

PHOTOLUMINESCENCE STUDY OF DEFECTS  
IN MERCURY CADMIUM TELLURIDE

BY

ROBERT FURSTENBERG

M.S., University of Illinois at Urbana-Champaign, 1999

DISSERTATION

Submitted in partial fulfillment of the requirements  
for the degree of Doctor of Philosophy in Physics  
in the Graduate College of the  
University of Illinois at Urbana-Champaign, 2006

Urbana, Illinois

# PHOTOLUMINESCENCE STUDY OF DEFECTS IN MERCURY CADMIUM TELLURIDE

Robert Furstenberg, Ph.D.

Department of Physics

University of Illinois at Urbana-Champaign, 2006

Yia-Chung Chang, Advisor

MBE growth and substrate related defects in mercury cadmium telluride ( $\text{Hg}_{1-x}\text{Cd}_x\text{Te}$ ) limit the performance of complex infrared devices (e.g. large focal plane arrays). A fundamental understanding of the underlying mechanism of defect formation and their characterization is needed. We have developed a novel experimental apparatus suitable for non-destructive optical characterization of these defects. It is based on Fourier Transform Infrared (FTIR) Spectroscopy. The apparatus is capable of measuring spectrally resolved photoluminescence, transmittance and photo-transmittance with high (diffraction-limited) spatial resolution in the infrared portion of the spectrum. In order to get quantitatively accurate FTIR spectra, we have also developed a new error-free algorithm for phase correction of FTIR interferograms using digital all-pass filters. With this apparatus, we have studied microscopic and macroscopic defects by analyzing spatial photoluminescence images (for macroscopic defects) and the temperature dependence of photoluminescence spectra (for microscopic defects - impurities). Defect levels were identified and their spatial distribution analyzed. Also, the effect of substrate surface preparation on the defects in the epilayer was studied. It was shown that photoluminescence study can be an effective tool in the optimization of MBE growth of  $\text{Hg}_{1-x}\text{Cd}_x\text{Te}$  epilayers.

*To my Grandmother Katarina*

# Acknowledgements

I would like to express my gratitude to my advisor, Prof. Yia-Chung Chang for his support, help and guidance during my studies. He is a great Professor and it was an honor for me to be one of his students.

Also, I would like to thank Prof. Chang for suggesting this research topic and introducing me to Dr. Jeffrey O. White who was also on board the MURI project and whose help and suggestions I appreciate a lot. His guidance throughout this project was invaluable.

I am very grateful to Dr. John H. Dinan (Army Research Laboratory, Fort Belvoir, VA) and Drs. John E. Jensen and Gregory L. Olson (HRL Laboratories, Malibu, CA) for providing the samples for the project.

I would also like to thank Prof. Stephen G. Bishop for his helpful comments and suggestions.

Finally, I would like to acknowledge the financial support for this work by the Army Research Office (grant No. DAAD 1901-1-0591), and by the Department of Physics (several teaching assistantships and a summer fellowship).

# Contents

<b>1</b>	<b>Introduction</b>	<b>1</b>
1.1	Motivation . . . . .	1
1.2	Thesis Overview . . . . .	3
<b>2</b>	<b>Overview of Basic Electronic and Optical Properties of <math>\text{Hg}_{1-x}\text{Cd}_x\text{Te}</math></b>	<b>5</b>
2.1	Electronic Structure . . . . .	5
2.2	Optical properties . . . . .	8
<b>3</b>	<b>Basic Principles of Fourier Transform Infrared Spectrometry</b>	<b>13</b>
3.1	The interferometer . . . . .	13
3.2	Calculating Spectra . . . . .	15
3.3	Loss of spectral resolution . . . . .	15
3.4	Phase errors . . . . .	18
3.5	Interferometers versus grating spectrometers . . . . .	19
<b>4</b>	<b>Phase Correction of Interferograms Using Digital All-pass Filters</b>	<b>22</b>
4.1	Introduction . . . . .	22
4.2	Theory . . . . .	27

4.3	Examples . . . . .	34
<b>5</b>	<b>Experimental Setup for the Acquisition of Near- and Mid-infrared Photoluminescence</b>	<b>40</b>
5.1	Mid-infrared setup . . . . .	40
5.1.1	Phase correction of interferograms in photo-transmittance experiments . . . . .	49
5.2	Near-infrared setup . . . . .	51
<b>6</b>	<b>Photoluminescence Imaging Study of <math>\text{Hg}_{1-x}\text{Cd}_x\text{Te}</math></b>	<b>53</b>
6.1	Introduction . . . . .	53
6.2	Spatially Resolved Photoluminescence of Bulk CdTe and CdZnTe	54
6.3	Room Temperature Photoluminescence . . . . .	55
6.4	High spatial resolution photoluminescence imaging of CdTe at 300K	60
6.5	Medium resolution photoluminescence imaging of CdTe and $\text{Cd}_{0.96}\text{Zn}_{0.04}\text{Te}$ at 77K . . . . .	63
6.6	Analysis of photoluminescence spectra in CdTe . . . . .	69
6.7	Photoluminescence imaging of $\text{Hg}_{1-x}\text{Cd}_x\text{Te}$ . . . . .	80
<b>7</b>	<b>Low Temperature Photoluminescence Study of <math>\text{Hg}_{1-x}\text{Cd}_x\text{Te}</math></b>	<b>84</b>
7.1	Influence of doping and alloy composition . . . . .	84
7.2	Influence of annealing . . . . .	88
7.3	Influence of substrate quality . . . . .	90
<b>8</b>	<b>The Effect of Multilayers on Luminescence Spectra</b>	<b>94</b>
8.1	Introduction . . . . .	94
8.2	Theory . . . . .	95
8.3	Discussion and Analysis . . . . .	101

<b>9 Summary</b>	<b>105</b>
<b>References</b>	<b>107</b>
<b>Author's Biography</b>	<b>112</b>

# Chapter 1

## Introduction

### 1.1 Motivation

This project was carried out as part of a collaborative effort by several research groups from the University of Illinois at Urbana-Champaign, University of Illinois at Chicago and University of Michigan. The wide array of research subprojects centered on fundamental issues concerning infrared detector materials and devices. As part of this Multi University Research Initiative (MURI) our goal was to develop an experimental apparatus suitable for non-destructive optical characterization of infrared detector materials and devices primarily by studying photoluminescence.

The materials we studied were  $\text{Hg}_{1-x}\text{Cd}_x\text{Te}$  epilayers (with the Cd content ranging from  $x = 0.28$  to  $x = 1$ ) and substrates used for their growth, primarily bulk CdTe,  $\text{Cd}_{0.96}\text{Zn}_{0.04}\text{Te}$  and CdTe epilayers grown on silicon substrates.

A substantial body of research has been accumulated since  $\text{Hg}_{1-x}\text{Cd}_x\text{Te}$  was first discovered as a material well suited for high quality infrared detectors. Most of this research dealt with the properties of bulk  $\text{Hg}_{1-x}\text{Cd}_x\text{Te}$  used in

photoconductive detectors. In recent years, new and highly complex infrared devices (e.g. two-color and multi-color focal plane arrays or FPAs) grown by MBE (and to some extent MOCVD) are being fabricated. Due to the ever-increasing demand for high quality infrared devices, the MBE growth process needs to be further optimized, especially when growing large devices on silicon substrates that result in substantial lattice mismatch.

The fabrication of these devices involves the deposition of several  $\text{Hg}_{1-x}\text{Cd}_x\text{Te}$  multilayers of different alloy content, doping type (p or n), doping concentration as well as etching of mesas for the delineation of individual detectors (diodes). In order to monitor the quality of the devices before subsequent fabrication steps are performed, it is highly desirable to have a non-destructive tool to detect bad growth runs. Also, for a systematic study of growth related defects and growth process optimization, a non-destructive, optical tool is indispensable. Photoluminescence has been used extensively in materials that emit photoluminescence in the visible and near-IR portion of the electromagnetic spectrum (e.g. III-Vs). For these classes of materials commercial systems are available. For infrared materials commercial tools are not available. This is mainly due to the fact that the measurement of infrared photoluminescence is much harder due to the lack of good detectors and because the techniques used for measuring visible/near-IR photoluminescence are inadequate in the infrared. To remedy this, we designed and built a novel experimental apparatus that is capable of measuring spectrally-resolved photoluminescence, transmittance and photo-transmittance with high spatial resolution at room- and liquid nitrogen temperatures. The apparatus is based on a Fourier Transform Infrared Spectrometer and has a custom made microscopic attachment for confocal, diffraction-limited resolution.

The system was used in the study of defects (both micro- and macroscopic)

in  $\text{Hg}_{1-x}\text{Cd}_x\text{Te}$  that limit its performance in infrared devices. For microscopic defects (impurities) the temperature dependence of PL spectra was measured and analyzed. For macroscopic defects, PL images were acquired and the spatial structure and distribution of such defects was analyzed. Also,  $\text{Cd}_{0.96}\text{Zn}_{0.04}\text{Te}$  substrates used in the MBE growth of  $\text{Hg}_{1-x}\text{Cd}_x\text{Te}$  epilayers were studied by using a similar methodology. Finally, we studied the correlation between substrates and the epilayers grown on top of them.

The system we built has also been successfully used by several other research groups at the University of Illinois (Professors P. Braun, J. Lewis, S.G. Bishop and S.L. Chuang).

## 1.2 Thesis Overview

The thesis is organized in 9 chapters.

- Chapter 2 gives an overview of the electronic structure and basic optical properties of  $\text{Hg}_{1-x}\text{Cd}_x\text{Te}$ .
- Chapter 3 gives a brief overview of the principles of FTIR spectrometry.
- In Chapter 4, a novel algorithm for phase correction of FTIR interferograms based on digital all-pass filters is given. It allows for improvement of the quantitative accuracy of FTIR spectra.
- Chapter 5 describes the experimental setup used in this work.
- Chapter 6 contains the result of the study of macroscopic defects in  $\text{Hg}_{1-x}\text{Cd}_x\text{Te}$  epilayers,  $\text{CdTe}/\text{Si}$  and bulk  $\text{Cd}_{0.96}\text{Zn}_{0.04}\text{Te}$  and  $\text{CdTe}$ . It also gives an analysis of defect level transitions in  $\text{CdTe}$ .

- In Chapter 7 the photoluminescence study of microscopic defects in  $\text{Hg}_{1-x}\text{Cd}_x\text{Te}$  is given.
- Chapter 8 gives the analysis of the distortion of PL spectra as a result of the propagation of PL photons through multilayered structures.
- Finally, in Chapter 9 we summarize the work and present the conclusions.

# Chapter 2

# Overview of Basic Electronic and Optical Properties of $\text{Hg}_{1-x}\text{Cd}_x\text{Te}$

## 2.1 Electronic Structure

$\text{Hg}_{1-x}\text{Cd}_x\text{Te}$  is a ternary alloy crystallizing in the zinc-blende structure over the entire composition range. At  $x = 1$  (i.e. CdTe) it is a direct-gap semiconductor with a bandgap of  $E_g \approx 1.6\text{eV}$ . Figure 2.1 shows the calculated electronic structure of CdTe, using the pseudo-potential method (Chadi et al., 1972). As the mercury content in  $\text{Hg}_{1-x}\text{Cd}_x\text{Te}$  is increased, its bandgap is decreased, until it completely closes at  $x \approx 0.15$  and the alloy becomes semi-metallic.

The band structure of  $\text{Hg}_{1-x}\text{Cd}_x\text{Te}$  near the  $\Gamma$  point of the Brillouin zone is shown in Fig. 2.2. The variation of bandgap as function of alloy composition is shown was given in Fig. 2.3 (Hansen et al., 1982). Hansen *et al.* also give an empirical expression valid for 4.2K to 300K and over the full alloy composition

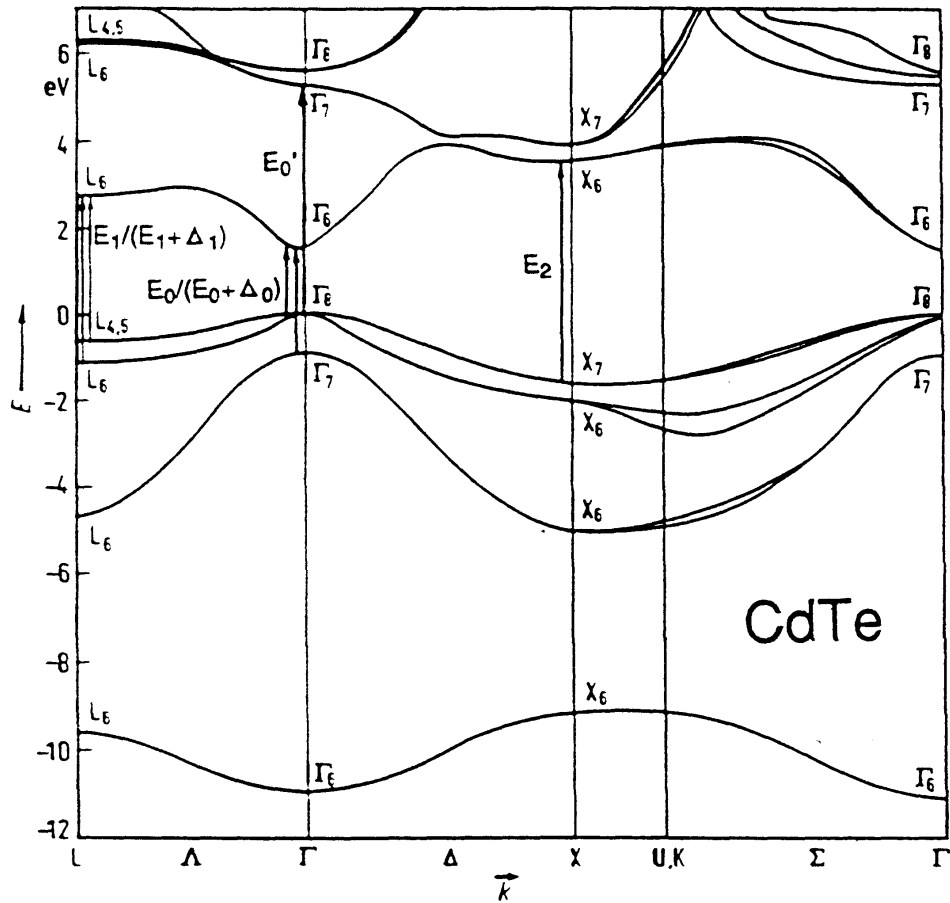


Figure 2.1: The electronic structure of CdTe (Chadi et al., 1972).

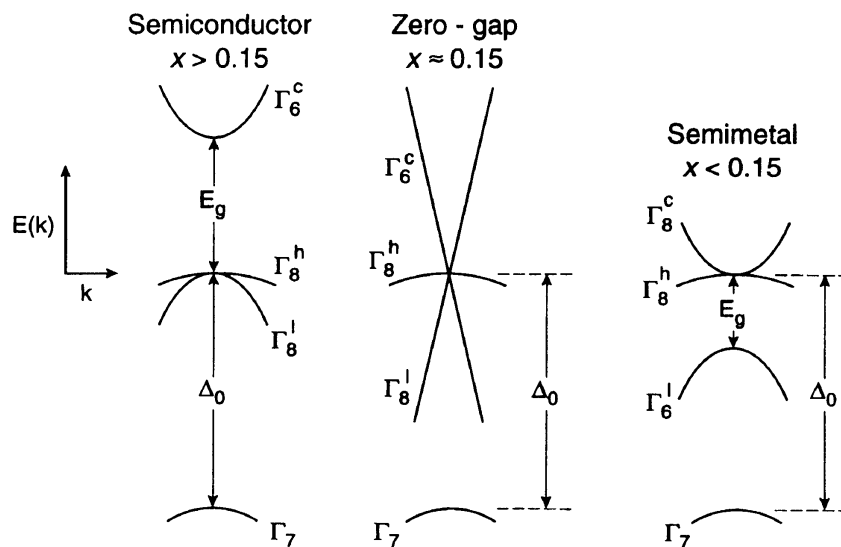


Figure 2.2: The bandgap of  $\text{Hg}_{1-x}\text{Cd}_x\text{Te}$  in the vicinity of the Brillouin zone center. (Capper, 1997).

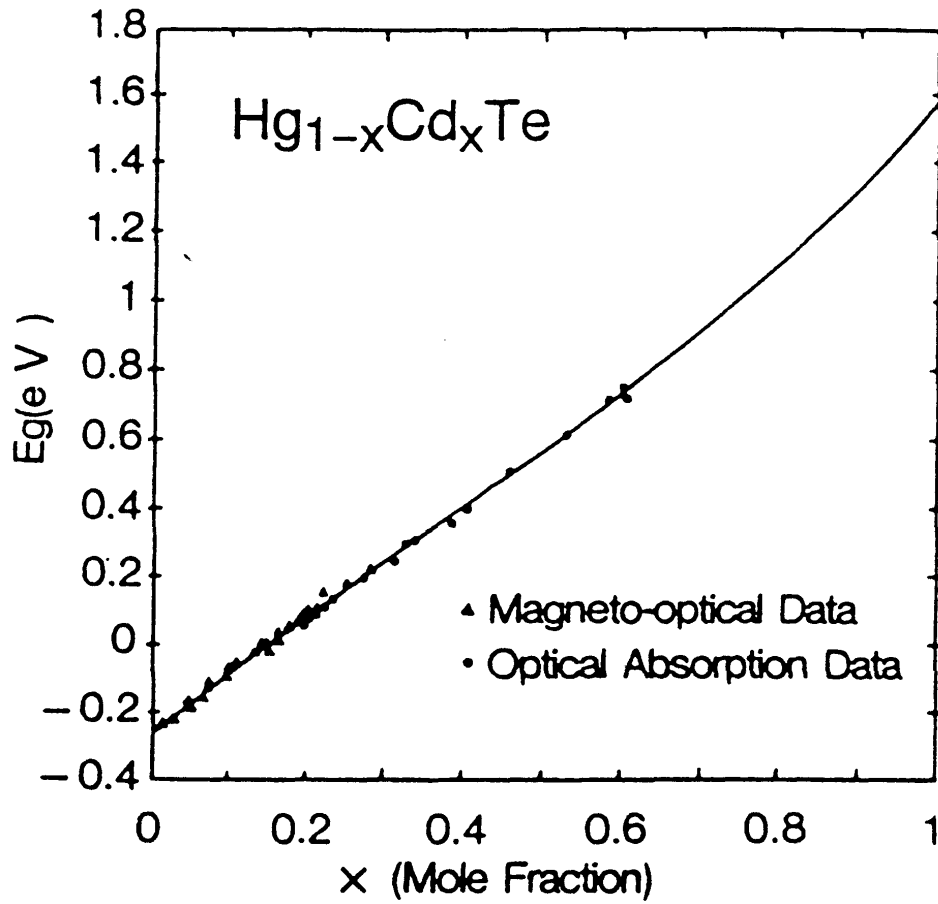


Figure 2.3: The bandgap of  $\text{Hg}_{1-x}\text{Cd}_x\text{Te}$  as a function of alloy composition at 80K (Hansen et al., 1982).

range with an error estimate of 0.013eV:

$$E_g(T, x) = -0.302 + 1.93x + 0.000535T(1 - 2x) - 0.810x^2 + 0.832x^3. \quad (2.1)$$

## 2.2 Optical properties

Of all the optical properties of  $\text{Hg}_{1-x}\text{Cd}_x\text{Te}$ , absorption is the most widely studied. The region around the fundamental absorption edge is especially important as it is used to determine the bandgap and has been studied in detail (Finkman and Schacham, 1984, Chu et al., 1991, Li et al., 1996, Nathan, 1998). Figure 2.4 shows the absorption coefficient of  $\text{Hg}_{1-x}\text{Cd}_x\text{Te}$  at 300K, as measured by Chu *et al.* (Chu et al., 1991). Above the bandgap, the absorption coefficient is determined by the electronic transitions from valence to conduction band states. For energies near  $E_g$ , for most semiconductors, parabolic bands are usually assumed and the absorption coefficient is given by

$$\alpha(\hbar\omega) \propto \sqrt{\hbar\omega - E_g} \quad (2.2)$$

In  $\text{Hg}_{1-x}\text{Cd}_x\text{Te}$ , however, a strong non-parabolicity of bands was observed (Krishnamurty et al., 1996), and (2.2) is often modified in order to achieve better agreement with experimental measurements:

$$\alpha(\hbar\omega) \propto \frac{\sqrt{(\hbar\omega - E_g + c)^2 - c^2(\hbar\omega - E_g + c)}}{\hbar\omega} \quad (2.3)$$

where  $c$  is the parameter defining the curvature of the band structure.

At energies below the bandgap,  $\text{Hg}_{1-x}\text{Cd}_x\text{Te}$  is characterized by a very pronounced Urbach tail (Urbach, 1953), attributed to structural and alloy disorder. The absorption coefficient in this region is described as

$$\alpha(\hbar\omega) \propto \exp\left(\frac{\hbar\omega - E_g}{W(T)}\right) \quad (2.4)$$

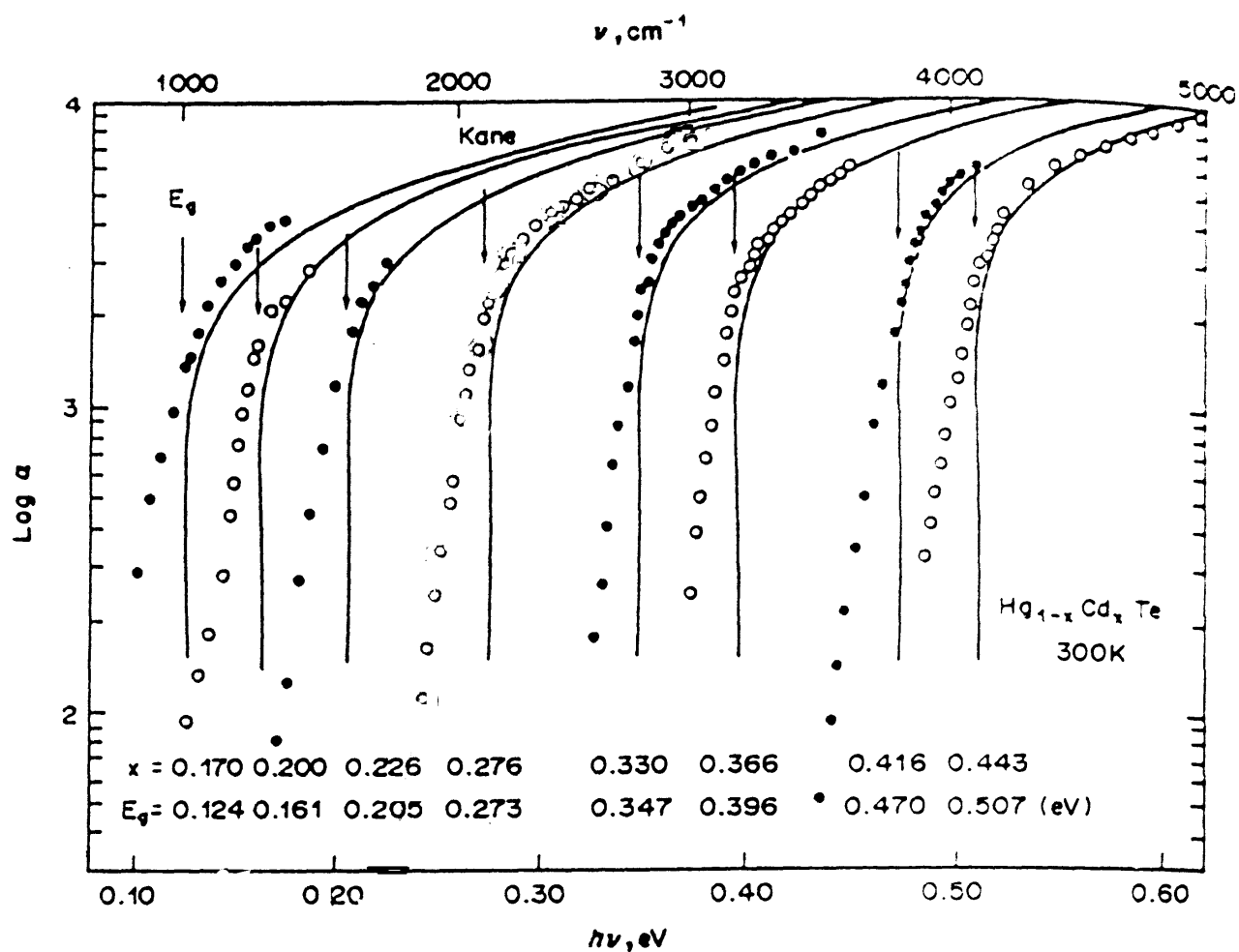


Figure 2.4: Optical absorption spectra of  $\text{Hg}_{1-x}\text{Cd}_x\text{Te}$  measured at 300K (Chu et al., 1991).

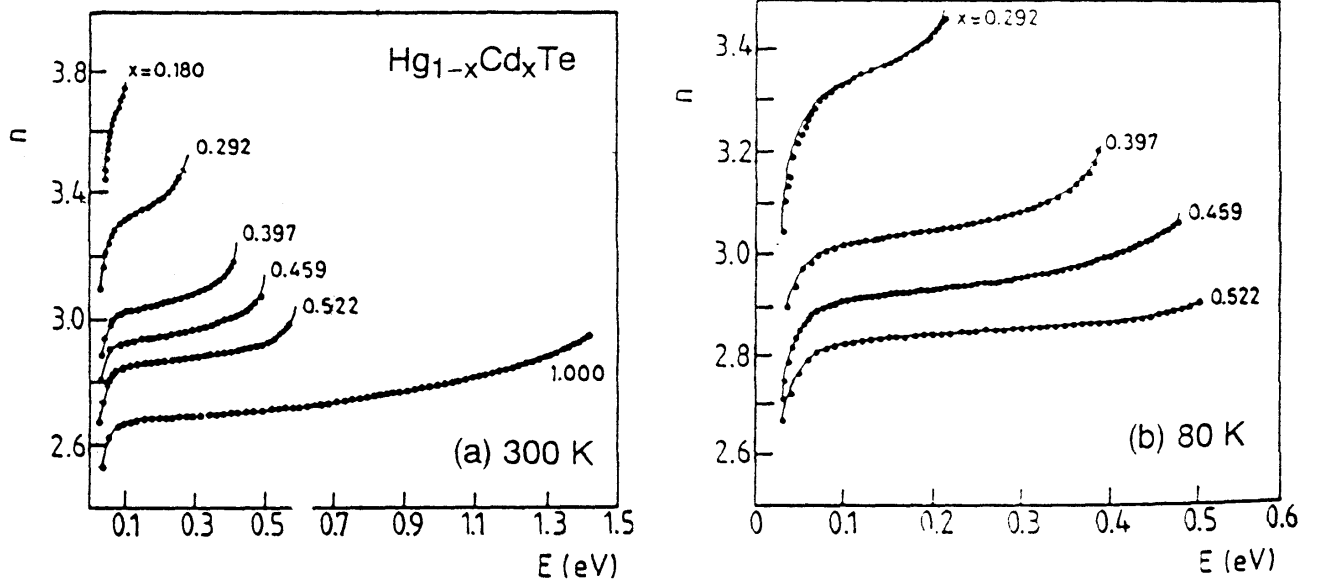


Figure 2.5: Index of refraction for  $\text{Hg}_{1-x}\text{Cd}_x\text{Te}$  at 300K (a) and 80K (b) (Kucera, 1987).

where  $W(T)$  is the Urbach tail energy which, in the adiabatic approximation, can be approximated as

$$W(T) = A + B \coth \frac{\hbar\omega_{LO}}{2k_B T} \quad (2.5)$$

where  $A$  is the term describing structural and alloy disorders, while the term  $B$  describes the temperature dependent electron-phonon interaction (Greeff and Glyde, 1995).

The  $\text{Hg}_{1-x}\text{Cd}_x\text{Te}$  bandgap can be defined as the crossover point between the two regimes (Moazzami et al., 2003, Chang et al., 2004, Ariel et al., 1997). Due to the large Urbach tail, this is not very reliable. Later in this work we give an alternative method based on photo-transmittance measurements.

The most often cited values for the index of refraction of  $\text{Hg}_{1-x}\text{Cd}_x\text{Te}$  were given by Kucera (Kucera, 1987), as shown in Fig. 2.5. However, these values only cover the region of transparency. Recently, spectroscopic ellipsometry mea-

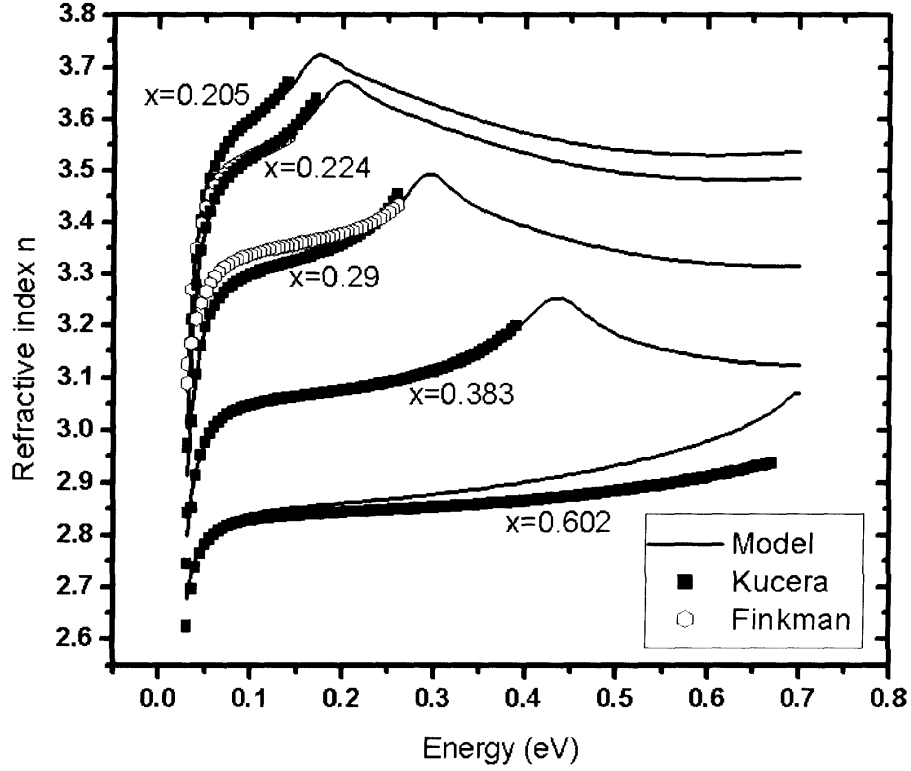


Figure 2.6: Index of refraction for  $\text{Hg}_{1-x}\text{Cd}_x\text{Te}$  at 300K measured by Infrared Spectroscopic Ellipsometry (Daraselia et al., 2005).

measurements were used to determine the dielectric function (and thus  $n(E)$ ) for energies  $E > E_g$  (Daraselia et al., 2005). Results are shown in Fig. 2.6. At even higher energies (1.8eV-5.5eV), the dielectric function of  $\text{Hg}_{1-x}\text{Cd}_x\text{Te}$  was measured earlier by Vina *et al.* (Vina et al., 1984) and is shown in Fig. 2.7.

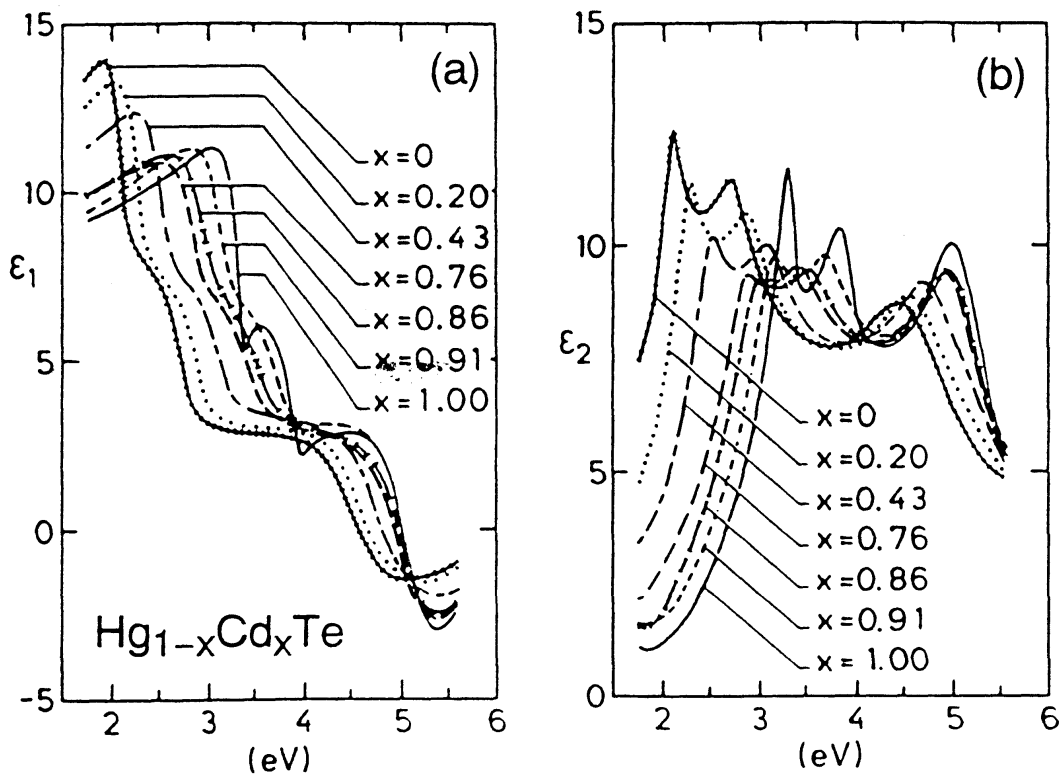


Figure 2.7: The dielectric function  $\epsilon(\omega) = \epsilon_1(\omega) + i\epsilon_2(\omega)$  of  $\text{Hg}_{1-x}\text{Cd}_x\text{Te}$  measured by Spectroscopic Ellipsometry at 300K. (Vina et al., 1984).

## Chapter 3

# Basic Principles of Fourier Transform Infrared Spectrometry

### 3.1 The interferometer

The main component of every Fourier transform infrared (FTIR) spectrometer is the interferometer. There are several different design implementations but all of them are conceptually similar to the Michelson interferometer. It essentially plays the role of a dispersive element (like a diffraction grating in a grating spectrometer) capable of separating a polychromatic source into its spectral components.

A collimated monochromatic beam is split by an ideal beamsplitter into two beams, as shown in Fig. 3.1. One beam is incident on a fixed mirror (F) while the other beam is incident on a moving mirror (M). Both beams reflect and reach the beamsplitter and split once again, travelling towards the source or the

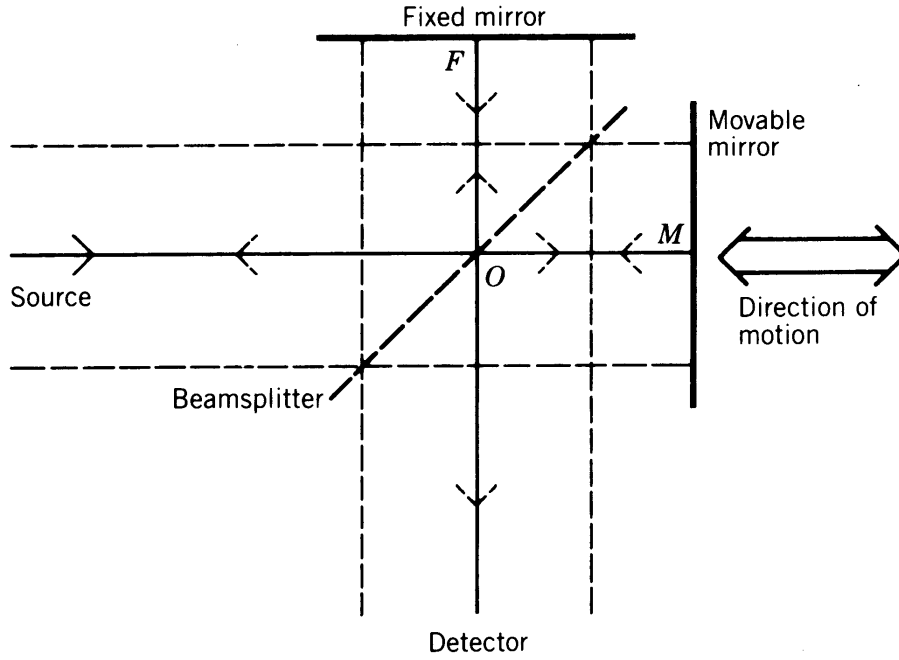


Figure 3.1: Schematic representation of a Michelson interferometer

detector. We are only interested in the beam traveling towards the detector. It represents a superposition of two beams, having a path difference of

$$\delta = 2(\overline{OM} - \overline{OF}) \quad (3.1)$$

The measured intensity of the beam at the detector is then:

$$I'(\delta) = \frac{1}{2}I_0(\lambda) \left( 1 + \cos \frac{2\pi\delta}{\lambda} \right) \quad (3.2)$$

Because the DC component is independent of the path difference  $\delta$ , it is neglected. Also, in FTIR spectrometry it is customary to use wavenumbers instead of wavelengths ( $\nu = \frac{1}{\lambda}$ ). With these modifications, we get

$$I(\delta) = \frac{1}{2}I_0(\nu) \cos 2\pi\nu\delta \quad (3.3)$$

Expression (3.3) assumes ideal beamsplitters (50-50 splitting ratio). In practice,  $I(\delta)$  is reduced due to the usage of a non-ideal beamsplitter, through the factor

$H(\nu)$ . Also, the detector signal is passed through preamplifiers and electronic filters which introduces a wavenumber dependent phase delay. Writing  $B(\nu) = H(\nu)I_0(\nu)/2$ , we get the following expression for the so called "interferogram" of a polychromatic source:

$$I(\delta) = \int_{-\infty}^{+\infty} d\nu B(\nu) \cos(2\pi\nu\delta + \theta_\nu) \quad (3.4)$$

## 3.2 Calculating Spectra

For a given interferogram, the spectrum of the source  $B(\nu)$  is obtained by Fourier transforming Eq. (3.4)

$$B(\nu) = \left| \int_{-\infty}^{+\infty} d\delta I(\delta) \exp^{-2\pi\nu\delta i} \right| \quad (3.5)$$

It is evident from equations (3.4) and (3.5) that in order to get the spectrum of a source without loss of information, the interferogram needs to be known in the interval  $-\infty < \delta < \infty$ . This is clearly impossible, as the moving mirror in the interferometer travels a finite distance  $-\delta_{max} < \delta < \delta_{max}$ .

## 3.3 Loss of spectral resolution

In principle, a finite interferogram can be treated as an infinite one, multiplied by a function

$$I'(\delta) = I_\infty(\delta)D(\delta) \quad (3.6)$$

where

$$D(\delta) \begin{cases} > 0 & \text{for } |\delta| \leq \delta_{max} \\ = 0 & \text{for } |\delta| > \delta_{max} \end{cases} \quad (3.7)$$

The spectrum is now given as a convolution:

$$\begin{aligned} B'(\nu) &= I_\infty(\nu) * D(\nu) \\ &= \int_{-\infty}^{\infty} d\nu' B(\nu') D(\nu' - \nu) \end{aligned} \quad (3.8)$$

The meaning of (3.8) is best illustrated by examining the calculated spectrum of a monochromatic source. It has a spectrum given by the Dirac delta function:

$$B(\nu) = B_0 \delta_{Dirac}(\nu - \nu_0) \quad (3.9)$$

If we insert (3.9) in (3.8), we get

$$\begin{aligned} B'(\nu) &= \int_{-\infty}^{\infty} d\nu' B_0 \delta_{Dirac}(\nu' - \nu_0) D(\nu' - \nu) \\ &= B_0 D(\nu - \nu_0) \end{aligned} \quad (3.10)$$

So instead of a delta function, the calculated spectrum is the Fourier transform of the truncating function  $D(\delta)$ . It now has a finite width and spectral artifacts.

Figure 3.2 shows several different truncating functions and their Fourier transforms. The most basic truncating function is the boxcar function. This corresponds to the case when the collected interferogram is Fourier transformed without any modifications, as we can see in Fig. 3.2a. In addition to a strong peak, we get a series of sidelobes. This means that the spectrum of a monochromatic source will exhibit spectral features at several frequencies around the main one. This is clearly undesirable. To remedy this, we choose different  $D(\delta)$  functions in order to reduce the sidelobes. Since the sidelobes are referred to as "feet", or "podos" in greek, the function  $D(\delta)$  is often called an apodization function. Various apodization functions are characterized by the amount of sidelobe suppression and the full-width at half maximum of the main peak. High sidelobe suppression comes at the expense of increasing the peak width.

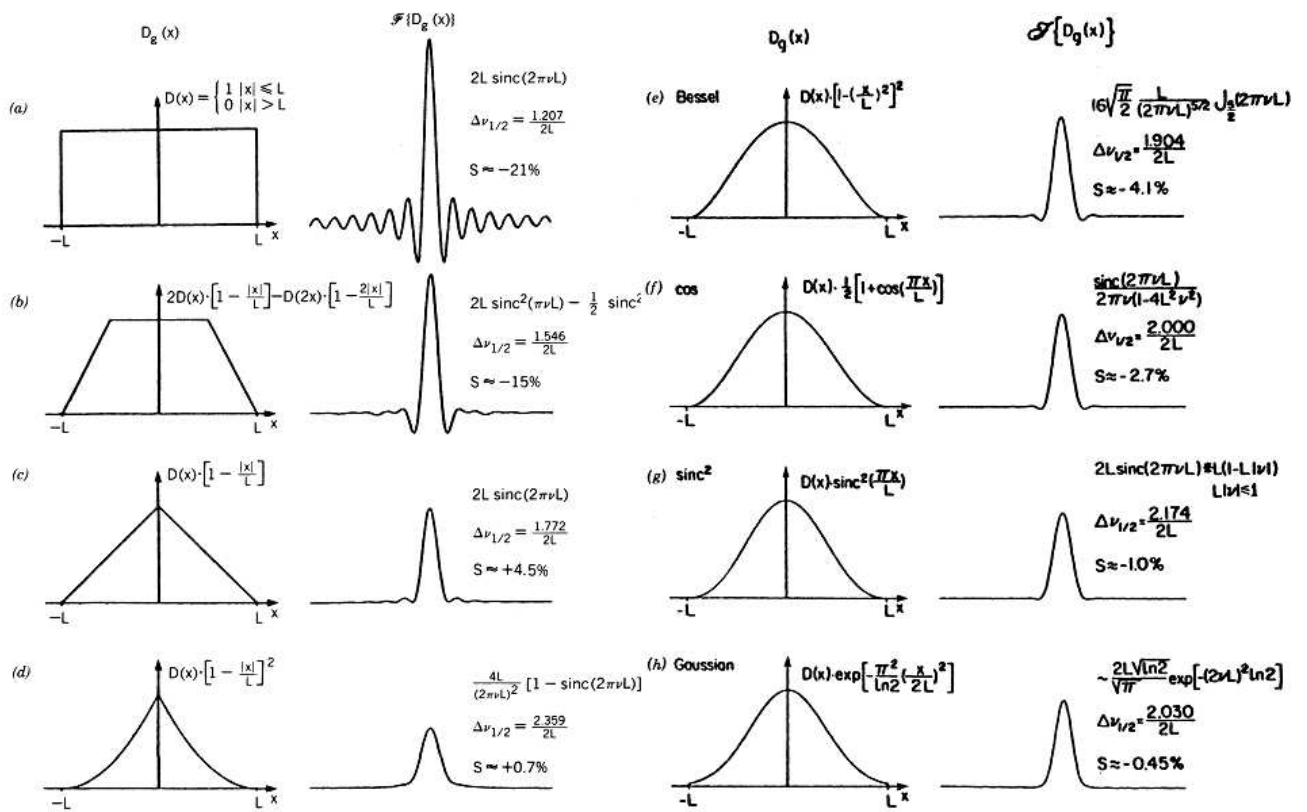


Figure 3.2: Commonly used apodization functions and their Fourier transforms.

## 3.4 Phase errors

In practice, equation (3.5) can be a source of errors. The noise component of real spectra will show up as purely positive contributions due to taking the magnitude function of the complex Fourier transform that results from asymmetric interferograms.

To remedy this, a procedure called phase correction is performed on the interferogram to render it symmetric (all cosine components line up at the  $\delta = 0$  point).

The most often used method is the one proposed by Mertz. It involves calculating the phase angle from the Fourier transform of the interferogram and then rotating this complex transform into the real axis by the amount of the phase angle. For an infinite interferogram, this would be an exact, error-free procedure. In case of finite interferograms, however, the Mertz method is a source of photometric errors. What follows is a brief explanation on why the Mertz method is inaccurate:

If a spectral component of the interferogram is not centered around the  $\delta = 0$  point, i.e. it contains a phase offset:

$$I(\delta) = B(\nu) \cos(2\pi\nu\delta + \theta_\nu) \quad (3.11)$$

then the apodization function will asymmetrically truncate the interferogram - since the  $\delta = 0$  point is arbitrary, it is obvious that having a phase offset in the interferogram is equivalent to having a symmetric ( $\delta_\nu = 0$ ) interferogram apodized by a function that is asymmetric (shifted) around the  $\delta = 0$  point. This means that the Fourier transform  $D(\nu)$  of the apodization function is not constant and symmetric any more and is changing shape with the change in phase. This in turn will produce a photometric error when such an interfer-

ogram is Fourier transformed. Since the Mertz method uses these inaccurate components of the fast Fourier transform (FFT) to obtain the true spectrum (by rotating them by the phase angle) it is evident that the final spectrum will also be inaccurate. It is important to emphasize that the main error of the Mertz method lies in fact that it relies on approximate FFT components, and not just because the phase angle (obtained from these components) is inaccurate. The solution to this problem is to remove most (if not all) of the phase error before the FFT is performed but without affecting the spectral content of the interferogram. In chapter 4 we will show that this can be done by applying an all-pass digital filter to the interferogram that removes most of its phase error (and thus eliminates the asymmetric apodization) before the true spectrum is calculated.

## **3.5 Interferometers versus grating spectrometers**

As we have seen in this chapter so far, the calculation of spectra in FTIR spectrometry involves substantial amount of calculation. Naturally, the usefulness of the method is in question, especially when one considers that grating spectrometers are much easier to use and obtaining spectra is easy and involves no calculations.

The most important reason why an FTIR spectrometer was used in this thesis is because of the high SNR of FTIR spectrometers over grating spectrometers.

There are two main reasons for the increased SNR:

## Throughput or Jacquinot's advantage

Throughput is defined as the solid angle from which the signal is collected multiplied by the collection area. It basically measures the total amount of radiation that can be collected from the sample while achieving a given spectral resolution. For example, in grating spectrometers, the input slit is quite small (fraction of a millimeter) and resulting in most of the radiation being discarded, in order to maintain high spectral resolution. The throughput of a Fourier spectrometer is given by

$$\theta_I(\nu) = 2\pi A^I \frac{\Delta\nu}{\nu_{max}} \quad (3.12)$$

where  $A^I$  is the area of the interferometer mirrors being illuminated,  $\Delta\nu$  is the spectral resolution and  $\nu_{max}$  is the maximum wavenumber in the spectrum. The throughput of a grating spectrometer is given by

$$\theta_G(\nu) = \frac{hA^G \Delta\nu}{fa\nu^2} \quad (3.13)$$

where  $A^G$  is the area of the grating being illuminated,  $f$  is the focal length of the collimating mirror,  $h$  is the slit height and  $a$  is the grating constant. Jacquinot's advantage is therefore given by the ratio:

$$A_J = \frac{\theta_I(\nu)}{\theta_G(\nu)} = \frac{2\pi hA^I fa\nu^2}{A^G h\nu_{max}} \quad (3.14)$$

Typically, in the mid-IR portion of the spectrum, Jacquinot's advantage is on the order of 100.

## Multiplexing or Fellgett's Advantage

In a grating spectrometer, at any given time during the acquisition of the spectrum, only a small portion of the input signal ( $\Delta\lambda$ , or  $\Delta\nu$ ) is being collected. The rest of the signal is discarded. In contrast, FTIR spectrometers record all

the signal all of the time. This yields a significant advantage. The Fellgett's advantage is:

$$A_F = \sqrt{\frac{\nu_{max} - \nu_{min}}{\Delta\nu}} = \sqrt{M} \quad (3.15)$$

where  $M$  is the total number of resolution elements.  $A_F$  usually ranges from 10 to 100.

Combining the values of the Jacquinot's and Fellgett's advantage we get an overall increase of SNR on the order of 1000.

This is significant when weak spectra, such as infrared photoluminescence are to be measured, especially when rapid acquisition of spectra is needed as is the case in photoluminescence imaging.

## Chapter 4

# Phase Correction of Interferograms Using Digital All-pass Filters

### 4.1 Introduction

Phase correction is one of the most important steps in the process of calculating spectra from recorded FTIR interferograms. The preferred method for most commercial instruments is the one proposed by Mertz (Mertz, 1965). Its mathematical equivalent, the Forman method (Forman et al., 1966) is used less frequently. Although quite accurate, it has been shown that the Mertz algorithm introduces photometric errors (Chase, 1982). The main reason for this error lies in the fact that the length of the interferogram is finite. This finite interferogram can be thought of as an infinite interferogram which is truncated by an apodizing function that is symmetric around the zero path difference point. However, due to the frequency-dependent phase of the interferogram, only one particu-

lar frequency (wavenumber) will experience symmetric apodization, all other frequencies will be asymmetrically apodized. This asymmetric apodization is the primary reason why the Mertz method is only approximate (Mertz, 1965). Apart from photometric errors, the Mertz method is found inadequate in instances when the interferogram is too noisy (Griffiths and de Haseth, 1986). In this case, phase correction is often not done at all, and the amplitude spectrum is used in lieu of the real (i.e. phase-corrected or true) spectrum, leaving the spectrum distorted. Stored phase curves are sometimes used with varying success.

In this chapter, an algorithm using digital all-pass filters is described and compared to the Mertz method. Its main advantage is the ability to achieve an arbitrarily high photometric accuracy and its applicability to noisy interferograms. Another advantage is that the output of the method is not a spectrum but rather an interferogram, which makes this (phase-corrected) interferogram available for further processing. One of the limitations of the method is slower computation speed (compared to the Mertz method) resulting from filter design. However, depending on the algorithm, the time required to design an all-pass filter with a personal computer is on the order of 100ms or less. For high precision applications, for example, the measurement of the dielectric function using FTIR based infrared spectroscopic ellipsometry, the virtual elimination of phase errors in the spectra, is well worth the extra processing time.

On the other hand, if stored filter coefficients are used, this method becomes even faster than the Mertz method. For noisier spectra this approach is more than adequate. In this case, phase correction can even be implemented on a hardware level as part of digital signal processing (DSP) circuits.

For certain applications, where a large number of spectra is acquired using

focal plane arrays, having a fast phase correction method is of paramount importance, especially if a rapid succession of FPA images is taken, as is the case in hyper-spectral target tracking and detection. We believe all-pass filters with pre-programmed (stored) filter coefficients are an excellent choice for phase correction of such spectra. They are extremely fast, and can be implemented as part of the DSP circuit used for the acquisition and analysis of spectra. Phase correction can be done in a streaming fashion, and since the output is a nearly phase corrected interferogram, only the real part (cosine) of the FFT needs to be calculated. This would further increase the speed of the system by an additional factor of 2.

What follows is a brief overview of digital filters. More details can be found elsewhere (Johnson, 1989a).

Digital filters are uniquely described by their transfer function  $H(z)$ . An infinite impulse-response (IIR) digital filter has a transfer function expressed as a rational function:

$$H(z) = \frac{b_0 + b_1z^{-1} + b_2z^{-2} + \dots + b_Mz^{-M}}{a_0 + a_1z^{-1} + a_2z^{-2} + \dots + a_Nz^{-N}} \quad (4.1)$$

The above transfer function can be shown to be related to a linear difference equation. From

$$H(z) = \frac{Y(z)}{X(z)} = \frac{\sum_{m=0}^M b_m z^{-m}}{\sum_{k=0}^N a_k z^{-k}} \quad (4.2)$$

we get

$$\sum_{k=0}^N a_k z^{-k} Y(z) = \sum_{m=0}^M b_m z^{-m} X(z) \quad (4.3)$$

A  $z$ -transform is defined as

$$Z\{x(n)\} = \sum_{n=0}^{\infty} x(n) z^{-n} \quad (4.4)$$

where  $x(n)$  is a casual sequence.  $z$ -transforms are the digital equivalent of the Laplace transforms.

Applying the inverse  $z$ -transform to Eq. (4.3), and using the shift property of  $z$ -transforms (Johnson, 1989b)

$$Z^{-1}\{z^{-m} X(z)\} = x(n - m) \quad (4.5)$$

we get

$$\sum_{k=0}^N a_k y_{n-k} = \sum_{m=0}^M b_m x_{n-m} \quad (4.6)$$

or

$$y_n = \frac{1}{a_0} \left( \sum_{m=0}^M b_m x_{n-m} - \sum_{k=1}^N a_k y_{n-k} \right) \quad (4.7)$$

where  $\{x_1, x_2, \dots, x_n, \dots\}$  is the input sequence and  $\{y_1, y_2, \dots, y_n, \dots\}$  is the filtered output. Equation 4.7 clearly shows how digital filtering amounts to only a few arithmetic operations on the input sequence, making it fast to execute. Moreover, a digital filter can have a hardware implementation in DSP circuits.

All-pass filters are a special class of digital filters (Johnson, 1989c) whose transfer function can be represented as:

$$H(z) = \frac{a_N + a_{N-1}z^{-1} + a_{N-2}z^{-2} + \dots + z^{-N}}{1 + a_1z^{-1} + a_2z^{-2} + \dots + a_Nz^{-N}} = \frac{z^{-N}Q(z^{-1})}{Q(z)} \quad (4.8)$$

where

$$Q(z) = 1 + a_1 z^{-1} + a_2 z^{-2} + \dots + a_N z^{-N}$$

and  $a_1, a_2, \dots, a_N$  are real coefficients.

It can be easily shown that

$$|H(\exp(i\omega))| = 1$$

which means that all frequencies are passed without attenuation or amplification. These filters are often used in signal and speech processing to modify the phase of signals without changing their amplitude. The phase response of an all-pass filter is given by:

$$\theta(\omega) = -N\omega - 2\arg Q(e^{i\omega}) \quad (4.9)$$

An important consideration when designing IIR filters is the issue of stability. An IIR filter is stable (i.e., produces a bounded output for a bounded input) if and only if all the poles of the transfer function lie within a unit circle in the complex plane (Johnson, 1989d).

To make the all-pass filtering method and the Mertz procedure easier to compare, the Mertz procedure can be thought of in terms of a filtering process in which the interferogram is convolved with a function that is the Fourier transform of the complex exponential of the phase curve. The transfer function of this filter would have a form similar to Eq. 1 but without the polynomial in the denominator, thus making it a finite impulse response (FIR) filter. The number of terms (polynomial coefficients) is large and is on the order of the length of the interferogram. This high filter order is the main disadvantage of FIR filters as compared to IIR filters, which can have a much smaller order

for the same filtering effect. IIR filters are much easier to implement in DSP circuits.

## 4.2 Theory

An analog interferogram  $I(\delta)$  is uniquely (albeit with a finite spectral resolution and provided that the Nyquist's sampling theorem is satisfied) represented by a digital sequence:

$$\mathbf{I} = \{I(1), I(2), \dots, I(n), \dots, I(N)\} \quad (4.10)$$

where:

$$I(n) = \int_0^\pi B(\omega) \cos((n - N_{ZPD})\omega + \theta_I(\omega)) d\omega \quad n = 1, 2, \dots, N \quad (4.11)$$

Where  $B(\omega)$  is the true (real, phase corrected) spectrum,  $\theta_I(\omega)$  is the phase for a given frequency  $\omega$ ,  $N_{ZPD}$  is the sampling point at which all components of the interferogram would constructively interfere if was zero. Usually,  $N_{ZPD}$  is chosen as the interferogram point with the maximum value.

Equation 4.11 is written with digital filtering in mind so instead of wavenumbers, normalized frequencies were used. These frequencies take value from 0 to  $\pi \frac{\text{rad}}{\text{s}}$ , where  $\pi \frac{\text{rad}}{\text{s}}$  corresponds to the Nyquist frequency. Normalized frequencies are related to wavenumbers by:

$$\omega = 2\pi\Delta\delta\nu \quad \text{or} \quad \omega = \pi \frac{\nu}{\nu_{max}} \quad (4.12)$$

where  $\Delta\delta[\text{cm}]$  is the mirror movement (retardation) between two sampling points,  $\nu[\text{cm}^{-1}]$  is the wavenumber and  $\nu_{max}$  is the Nyquist frequency in wavenumbers.

The usual procedure for performing a Fourier transform of interferograms involves their shifting so that the point with the maximum value ( $n = N_{ZPD}$ ) is placed in the first position before applying the FFT algorithm. This yields a phase curve with both positive and negative values. However, stable all-pass filters can have only negative phase so the above procedure is modified by placing the point  $n = N_{ZPD} + N_{SHIFT}$  in the first position. This introduces an additional phase shift  $+N_{SHIFT}\omega$ :

$$\theta_I^{N_{ZPD}+N_{SHIFT}} = N_{SHIFT}\omega + \theta_I^{N_{ZPD}}(\omega) \quad (4.13)$$

where the superscript in  $\theta_I^{N_{ZPD}}(\omega)$  refers to the point around which the phase curve is calculated. ( $\theta_I^{N_{ZPD}}(\omega)$  will be abbreviated as  $\theta_I(\omega)$ ). If  $N_{SHIFT}$  is sufficiently large,  $\theta_I^{N_{ZPD}+N_{SHIFT}} > 0$  for all  $\omega$ .

If an all-pass filter has a phase response (up to an integer multiple of  $2\pi$ ) that is the exact opposite of the phase curve array in a given interferogram:

$$\theta_F(\omega) = -N_{SHIFT}\omega - \theta_I(\omega) \quad (4.14)$$

within an angular precision  $\Delta\theta(\omega)$  for frequencies  $\omega \in (\omega_1, \omega_2)$  for which the detector is responsive and/or there are spectral features, then it will be said that the interferogram  $\mathbf{I}_F$ , which is the result of applying the filter  $F$  to the interferogram  $\mathbf{I}$  (using Eq. 4.7) is phase corrected. Note that the phase curve  $\theta_I(\omega)$  of the interferogram  $\mathbf{I}$  still needs to be calculated around  $N_{ZPD}$ . If a shift is performed now on  $\mathbf{I}_F$  so that the point  $n = N_{ZPD} + N_{SHIFT}$  is the first position and subsequently a fast Fourier transform is performed, the real part of the resulting transform will be the true spectrum  $B(\omega)$ , while the imaginary part will only contain noise. It is important to point out that in the Mertz method the true spectrum is calculated using the Fourier transform components

of the uncorrected interferogram while in the all-pass filtering method the interferogram is phase corrected prior to FFT which greatly reduces the effects of asymmetric apodization on the photometric accuracy.

A residual phase error  $\Delta\theta(\omega)$  introduces a photometric error:

$$\frac{\Delta B(\omega)}{B(\omega)} \approx 1 - \cos(\Delta\theta(\omega)) \quad (4.15)$$

For example, for  $\Delta\theta = 5^\circ$ ,  $\frac{\Delta B}{B} = 0.38\%$  and for  $\Delta\theta = 2^\circ$  is only 0.06%.

Phase correction amounts to finding a suitable  $N_{SHIFT}$  and a set of coefficients  $\mathbf{a}_F = \{1, a_1, \dots, a_{NF}\}$  in Eq. 4.8 so that Eq. 4.14 is satisfied. This is done by minimizing an error function with respect to  $\mathbf{a}_F$ . In case the phase of the interferogram  $\theta_I(\omega)$  is known, the error function is given by:

$$E(a_1, a_2, \dots, a_{NF}) = \max_{\omega_1 \leq \omega \leq \omega_2} (\theta_F(a_1, a_2, \dots, a_{NF}) + N_{SHIFT} + \theta_I(\omega)) \quad (4.16)$$

When the interferogram is noisy, phase correction can be done indirectly by minimizing the imaginary part of the Fourier transform:

$$E(a_1, a_2, \dots, a_{NF}) = \sum_{i=1}^{N_{FFT}} w(i) \left( \text{Im} \mathbf{I}_F^{(a_1, a_2, \dots, a_{NF})}(i) \right) \quad (4.17)$$

where  $\mathbf{I}_F^{(a_1, a_2, \dots, a_{NF})}(i)$  is the interferogram after being filtered with an all-pass filter with coefficients  $\mathbf{a}_F$ ,  $w(i)$  is a weight function where  $w(i) = 0$  for parts of the spectrum where only noise is present and  $w(i) = 1$  where spectral information is expected. Note that only a small part (32 to 256 points) of the filtered interferogram (shifted around the point  $n = N_{ZPD} + N_{SHIFT}$ ) needs to be Fourier transformed because the phase is a slowly changing function. When the imaginary part is minimized, the resulting real part can be either all positive or all negative. If it happens to be all negative, the whole spectrum should

simply be multiplied by  $-1$ . To get a very rough estimate of the level of phase correction achieved, the following expression can be used to obtain the average phase error:

$$\langle \Delta\theta(\omega) \rangle \leq \frac{\sum w(i) |\arctan(\text{Im}\mathbf{I}_F(i)/\text{Re}\mathbf{I}_F(i))|}{\sum w(i)} \quad (4.18)$$

Several efficient methods for all-pass filter design have been reported in the literature (Jing, 1987, Deczky, 1974). Most of them are based on linearizing the nonlinear error function. To do this, however, a detailed knowledge of the partial derivatives of the error function with respect to the optimizing variables is needed. This is not practical, especially for Eq. (4.17). Some methods also require a good initial guess to guarantee stability and an optimal solution. Later in the chapter, a particularly simple algorithm is presented suitable for minimizing both Eq. (4.16) and Eq. (4.17). It does not require an initial guess for the filter coefficients, nor does it use the derivatives of the error function. As a result, the method is somewhat slower although execution speed is still reasonable (on the order of 100ms).

In general, Eq. (4.16) and Eq. (4.17) can be successfully minimized depending on the prescribed angular precision  $\Delta\theta$  and filter order  $N_F$ . The filter order can be thought of as the number of free parameters in a fitting procedure - the higher the filter order and the smoother the phase curve the lower  $\Delta\theta$  can be. Also, the smaller the frequency range  $(\omega_1, \omega_2)$  the easier it is to design a filter. Stable all-pass filters have two natural limits:  $\theta(0) = 0$  and  $\theta(\pi) = -N_F\pi$ . All-pass filters tend to be stiffer around these points so as  $\omega \rightarrow 0$  or  $\omega \rightarrow \pi$  it will be harder to find a filter that satisfies Eq. (4.14). It is recommended that interferograms with high wavenumbers be sampled with the smallest possible  $\Delta\delta$  (Eq. (4.12)) so that the highest frequency is well below the Nyquist limit.

In this work, interferograms covering the spectral region from  $\nu = 4000\text{cm}^{-1}$  to  $\nu = 800\text{cm}^{-1}$  (sampled with  $\nu_{max} = 15802\text{cm}^{-1}$ ) were successfully treated. If a wider spectral range is to be covered (which is unlikely since most detectors do not cover a much wider range), it might take longer to find a suitable filter and the filter order may need to be higher.

It is important to point out that the result of filtering is a phase corrected interferogram with a given angular precision  $\Delta\theta$ . This means that if further phase correction is desired, it can be done so with either another all-pass filter or the Mertz (or any other) method.

Phase errors in spectra have both electronic and optical origins. The electronic phase error results from the detector preamplifier and electronic (or digital) filtering of the signal prior to phase correction. The electronic contribution can be assumed constant for a given combination of detector/preamplifier, electronic filters and mirror velocity and ambient temperature. Not only is it constant, it is a slowly varying function of frequency so low order all-pass filters can be used to correct it.

Moreover, the transfer function of any electronic system can be expressed in the form given by Eq. (4.1), which makes a digital filter a natural choice for modeling the electronic contribution to the phase curve.

The optical contribution is a result of dispersion in the beamsplitter or if an optically dispersive material is inserted in one arm of the interferogram to intentionally chirp the interferogram. It can also be assumed constant for a given temperature, though it is not always very smooth (in case of intentional chirping), so a higher order filter might sometimes be required.

The temperature dependence of both the electronic and optical contributions to the phase error is not strong and small fluctuations will not significantly affect

the phase.

It is then possible to have a digital all-pass filter stored in the processing computer for every possible (but finite) combination of preamplifiers, filters, beamsplitters and mirror velocities. This way, a rough phase correction with these filters, followed by the Mertz method (which is now error free since the residual phase after the filtering is at most 5-10 degrees) will produce spectra that have virtually no photometric error.

A general phase correction algorithm based on digital all-pass filters is given below:

1. If possible, calculate  $\theta_I(\omega)$ . The best way to get the phase curve is to use the procedure given in the Mertz method (by using a small, say, 256 point symmetric interferogram around  $N_{ZPD}$ ). If the phase cannot be found reliably (e.g. emission experiments yielding noisy interferograms) then a different approach is needed as described later.

2. Choose the filter order  $N_F$  based on the degree of smoothness of the phase curve and the  $\Delta\theta$  desired. For a 3-10 degree error and a typical interferogram resulting from an absorption experiment on a rapid scan FTIR,  $N_F = 9$  will suffice.

3. Design an all-pass filter using any suitable filter design method to minimize Eq. (4.16) to satisfy Eq. (4.14), when  $\theta_I(\omega)$  is known, or, by minimizing Eq. (4.17) when it is unknown. This step also involves choosing an integer number  $N_{SHIFT}$ , as described earlier. It was observed that the execution speed of the filter design algorithm strongly depends on  $N_{SHIFT}$ , therefore it should be left to be determined by the algorithm.

4. Apply the filter to interferogram  $\mathbf{I}$  to obtain the phase corrected interferogram  $\mathbf{I}_F$ .

5. Before fast Fourier transforming  $\mathbf{I}_F$ , perform the usual shift, but this time the point  $n = N_{ZPD} + N_{SHIFT}$  is placed in the first place.

6. The real part of the FFT transform from step 5 is the phase corrected spectrum. No additional steps are required. If, for some reason, additional phase correction on  $\mathbf{I}_F$  is desired, set  $\mathbf{I} = \mathbf{I}_F$  and  $N_{ZPD} = N_{ZPD} + N_{SHIFT}$  (because the ZPD position for interferogram  $\mathbf{I}_F$  moved by  $N_{SHIFT}$  in the filtering process). Either use the Mertz method on the new  $\mathbf{I}$  to obtain the final spectrum, or go to step 1 to repeat the algorithm.

A method for designing all-pass filters suitable for minimizing both Eq. (4.16) and Eq. (4.17) is given below. It is not particularly efficient but it is very easy to implement and produces good results for low order filters ( $N_F < 16$ ). Filters with higher orders and frequencies closer to the Nyquist limit should be designed with other, more efficient methods (Jing, 1987, Deczky, 1974). The algorithm is based on randomly choosing filter coefficients  $\mathbf{a}_F$  that produce a stable filter and calculating the error function. The process is repeated until the prescribed angular precision is reached or a given number of trials have been performed. In order to generate a stable filter, instead of coefficients  $\mathbf{a}_F$  we randomly chose the poles of the filter  $\{z_1, z_2, \dots, z_{N_F}\}$  to make sure  $|z_i| < 1$  for all  $i$ . The algorithm involves the following steps:

1. Choose the filter order (usually  $N_F = 8$  to 16).

2. If  $N_F$  is even set  $N_{CC} = N_F/2$  and  $N_R = 0$ .

If  $N_F$  is odd set  $N_{CC} = (N_F - 1)/2$  and  $N_R = 1$ .  $N_R$  is the number of real poles of the filter while  $N_{CC}$  is the number of complex conjugate pairs.

3. Set a variable  $E^*$  to a large positive number.

4. Choose  $N_R$  random poles such that  $\text{Im}(z_i) = 0$  and  $\text{Re}(z_i) < 1$  and

$N_{CC}$  random poles such that  $|z_i| < 1$  . To avoid the possibility of accidentally choosing a pole with  $|z_i| \geq 1$  , instead of 1, set this limit to slightly lower number such as 0.999.

5. In terms of complex poles, the complex polynomial  $Q(z)$  from Eq. (4.8) can be calculated as:

$$Q(z) = \prod_{i=1}^{N_R} (z_i - z^{-1}) \prod_{j=1}^{N_{CC}} (z_j - z^{-1}) (z_j^\dagger - z^{-1}) \quad (4.19)$$

After expanding the product in Eq. (4.19) and comparing it to Eq. (4.8) the coefficients  $\mathbf{a}_F$  can be easily read off.

6. Calculate  $E$  according to Eq. (4.16) or Eq. (4.17) for the required phase response  $\theta_F(\omega)$  and frequency range. When calculating  $E$ , chose  $N_{SHIFT}$  that gives the minimum deviation. If  $E^* = E$ , set  $\mathbf{a}_F^* = \mathbf{a}_F$  , and  $N_{SHIFT}^* = N_{SHIFT}$

7. If the required precision is not achieved go to step 4.

8. The filter coefficients  $\mathbf{a}_F^*$  represent an all-pass filter that has the required phase response. After applying this filter, the centerburst of the interferogram will move to  $N_{ZPD}^* = N_{ZPD} + N_{SHIFT}$  .

For  $N_F = 9$  and  $\Delta\theta(\omega) = 5^\circ$  , filter coefficients can be obtained after  $\approx 1000$  trials. On an average personal computer this might take 100ms or less for minimizing Eq (4.16). A Java software package that implements the above algorithm was developed.

### 4.3 Examples

The measured spectrum of an infrared source ( $8\text{cm}^{-1}$  resolution,  $\nu = 4000\text{cm}^{-1}$  to  $\nu = 800\text{cm}^{-1}$  , sampled with  $\nu_{MAX} = 15802\text{cm}^{-1}$ ) was used to calculate

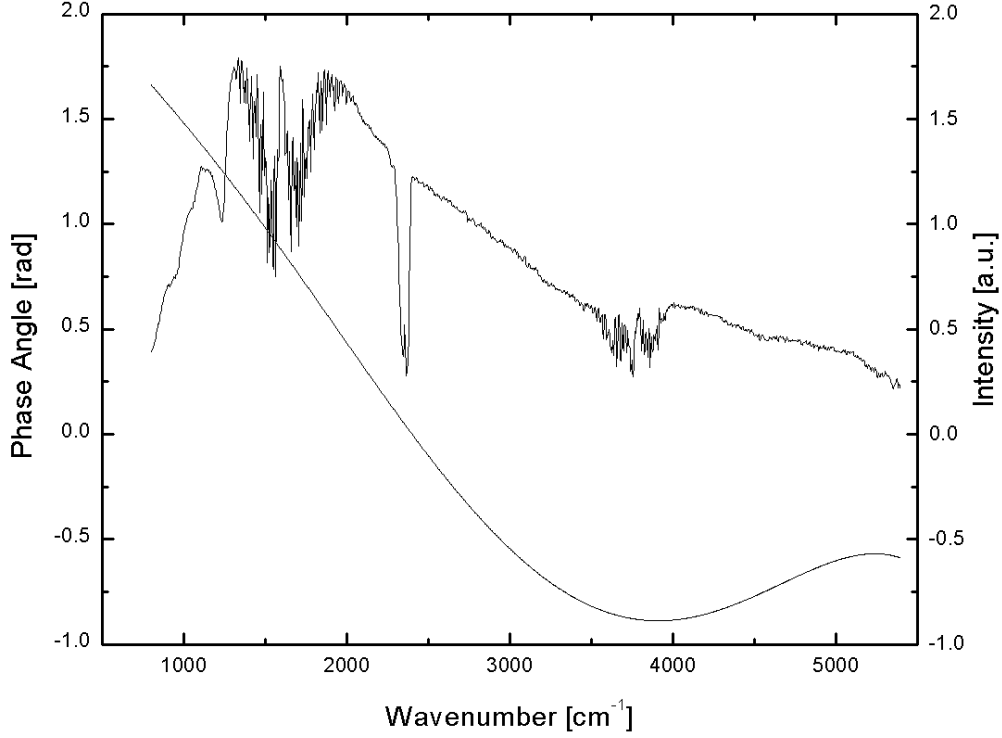


Figure 4.1: Spectrum and phase used to synthesize the interferogram.

two double sided synthetic interferograms with 8192 points using Eq. (4.11) with  $N_{ZPD} = 4097$ . The first interferogram had no phase shift introduced and its spectrum was used as a reference. The second one had a phase given by  $\theta(\omega) = 2.374 - 5.137\omega + 9.296\omega^2 - 41.499\omega^3 + 59.677\omega^4 - 25.305\omega^5$ . This phase curve was obtained by fitting the actual phase curve of the spectrum used in the synthesis of the interferograms. The spectrum and the phase curve are shown in Figure 4.1. All interferograms were apodized with the triangle function.

The phase-shifted interferogram was corrected by four methods:

1. Mertz method only (256 points for the phase curve determination).
2. All-pass filter ( $N_F = 9$ ,  $N_{SHIFT} = 10$ , filter coefficients:

$$a_0 = 1, a_1 = -1.582662, a_2 = 1.65706, a_3 = -1.039343, a_4 = 0.675962, \\ a_5 = -1.033974, a_6 = 0.882683, a_7 = -0.522626, a_8 = 0.04847554, a_9 =$$

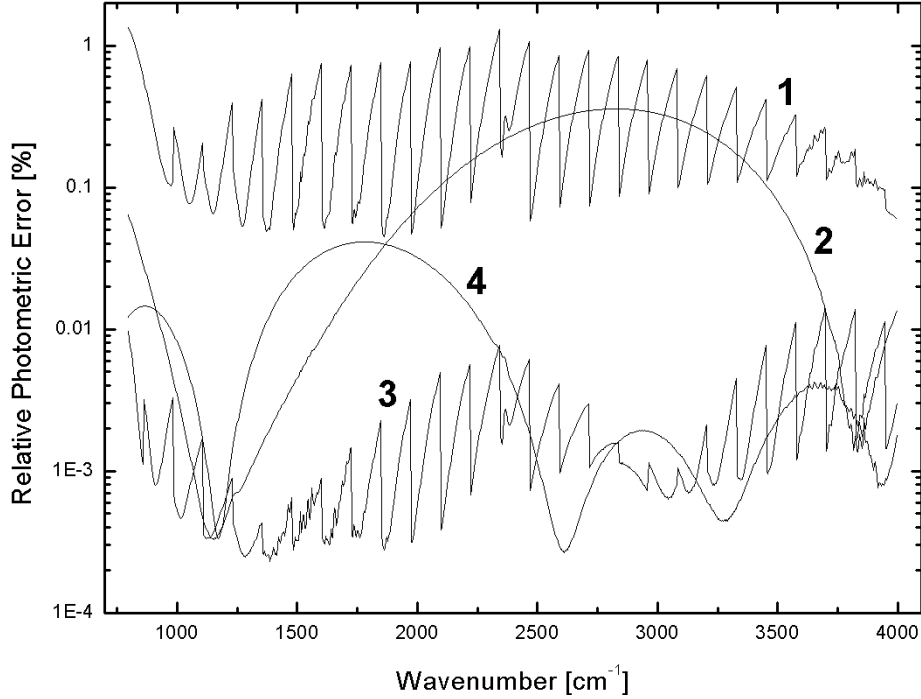


Figure 4.2: Error comparison of various phase correction methods.

$-0.001849615$ ) with  $\Delta\theta = 5^\circ$ .

3. All-pass filter from Method 2 followed by the Mertz method.

4. All-pass filter ( $N_F = 9$ ,  $N_{SHIFT} = 12$ , filter coefficients:

$a_0 = 1$ ,  $a_1 = -1.155238$ ,  $a_2 = 0.420712$ ,  $a_3 = 0.00561713$ ,  $a_4 = -0.0674369$ ,  
 $a_5 = -0.0935053$ ,  $a_6 = -0.0449673$ ,  $a_7 = -0.0137911$ ,  $a_8 = -0.00260652$ ,  
 $a_9 = -0.000238929$ ) with  $\Delta\theta = 1.3^\circ$ .

Fig. 4.2 shows the relative error for the above methods:

$$\Delta B/B[\%] = (\text{Re}(I_{corrected}) - \text{Re}(I_{ref})) / \text{Re}(I_{ref}) 100\%$$

Method 1 had an average photometric error of 0.3%. The oscillations of the error resulted from the interpolation of the phase curve. Near the beginning of the spectral region the photometric error appears to be diverging above 1%.

Method 2 had a bounded, slowly oscillating error of not more than 0.4%

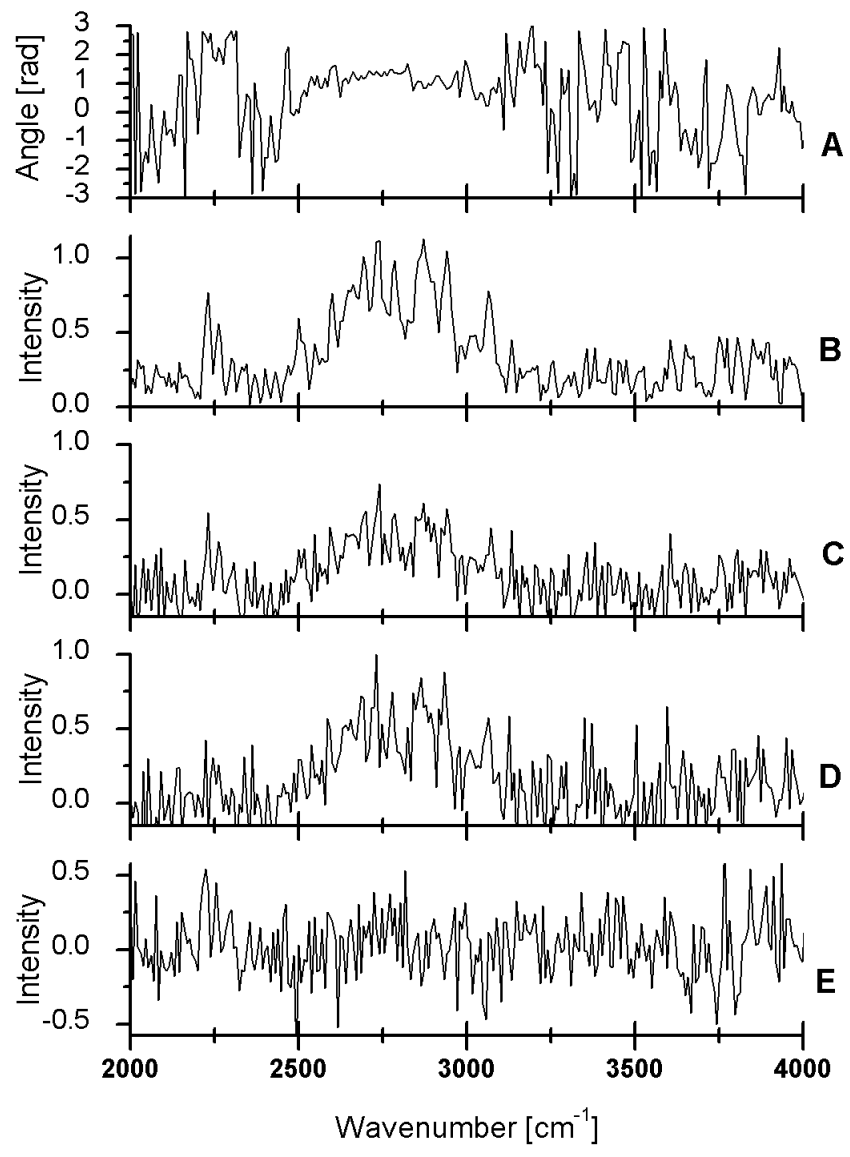


Figure 4.3: Phase correction of an interferogram with a noisy phase curve.

throughout the region, in line with the expected value according to Eq. (4.15).

Method 3 is virtually error-free throughout the spectral region (average error of 0.002%, maximum error of 0.014% at  $3820\text{cm}^{-1}$ ), and shows that perfect, error-free phase correction is possible by first applying a low-order all-pass filter that reduces the phase error below a certain level (5-10 degrees) and then followed by the Mertz method. To make method 3 as fast as the Mertz method alone, one can use previously calculated filter coefficients (for a given detector, preamplifier, electronic filter, beamsplitter and mirror velocity combination) and apply it before the Mertz method is used. By removing most of the phase error in the interferogram, the Mertz method becomes virtually error-free. This is especially useful for chirped interferograms which are prone to phase errors when only the Mertz method is used.

Method 4 is similar to method 2, with the exception that the angular precision of the filter is much higher, resulting in a small photometric error comparable to that of in method 3. The main disadvantage is much slower computation speed (2.2s in this example). Also, with such a high angular precision there is always the possibility that no suitable filter can be found. Method 4 should be avoided in practice.

Finally, an example of the method for unreliable phase curves is given. The interferogram is from a high spatial-resolution scanned photoluminescence (Furstenberg et al., 2004) experiment using the double-modulation technique. The sample was a film of on a substrate. It was excited with a focused 980nm laser through a reflecting objective and band- edge photoluminescence (PL) was recorded from a  $10\mu\text{m}$  spot size. Since the interferogram is too noisy to reliably determine the ZPD point, the ZPD point of the absorption interferogram that was collected in parallel with the PL spectrum was used instead. Figure 4.3A

shows the phase curve while Fig. 4.3B the amplitude spectrum of the band edge PL. Since the spectral information is contained in a narrow wavenumber range (3500 $\text{cm}^{-1}$  to 2300 $\text{cm}^{-1}$ ) only a third order filter was used to minimize the imaginary part of the interferogram with a total of 500 iterations. Figure 4.3C shows the result of the Mertz method, while Fig. 4.3D the real part of the filtered interferogram. Figure 4.3E shows the imaginary part of the filtered interferogram which only contains noise. It can be seen that the peak area for the magnitude spectrum (Fig. 4.3B) is higher than that for the all-pass filtering method demonstrating that noise, which always makes a positive contribution in magnitude spectra, raised the overall peak. On the other hand, the Mertz method (Fig. 4.3C) yielded a slightly smaller peak area because the phase curve was too noisy and deviated from the actual (smooth) phase curve and the resulting over-corrections and under-corrections of phase always yielded a smaller spectral intensity.

# Chapter 5

# Experimental Setup for the Acquisition of Near- and Mid-infrared Photoluminescence

This chapter gives a description of the experimental setups used to acquire infrared photoluminescence spectra. Two major setups were used, one for the mid-IR and one for the near-IR spectral range.

## 5.1 Mid-infrared setup

The apparatus is designed around a commercial ThermoNicolet Nexus 670 rapid scan FTIR spectrometer to which several optical and electronic components were added to achieve rapid acquisition of PL spectra with high spectral and spatial resolution. Figure 5.1 gives a schematic diagram of the major components of

the apparatus. Figure 5.2 shows a photograph.

The sample holder is mounted on a pair of perpendicular translation stages (Newport) motorized by linear actuators (Zaber LA-60).

Photoluminescence is excited and collected with an Ealing  $36 \times 0.5\text{NA}$  reflecting objective (O1). Reflecting objectives are free from chromatic aberrations, which is an important feature because of the wide range of wavelengths involved. The objective is mounted on a translation stage for alignment and fine focusing. An aperture (AP1) is placed 160mm from O1, at the intermediate image plane, to achieve confocal illumination and detection. Confocal detection is particularly important when PL is measured, because without it, carrier diffusion can degrade the effective resolution.

A visible light focusing tool (not shown in Fig. 5.1) can be temporarily inserted between O1 and AP1. It projects the intermediate image plane at AP1 onto the focal plane of a CCD camera, and also illuminates the sample.

The PL excitation source is a 1440nm laser diode ( $P_{max}=100\text{mW}$ ). It is introduced through a single mode optical fiber and is imaged by an achromatic lens L1 onto AP1 in such a way as to match the input NA of O1. Subsequently, the laser beam is refocused by O1 onto the sample to excite photoluminescence. Objective O1 collects the PL in back-reflection and sends it through the beamsplitter BS1. Mirror M1 serves to match the NA of the input paraboloid mirror M2 of the FTIR which was moved out from its original location inside the spectrometer.

Beamsplitter BS1 is a germanium plane-parallel window. It reflects approx. 25%-30% of the excitation laser, transmits 50%-60% of the infrared PL and filters out the reflected excitation laser.

After passing the FTIR interferometer the signal is taken from the focus of

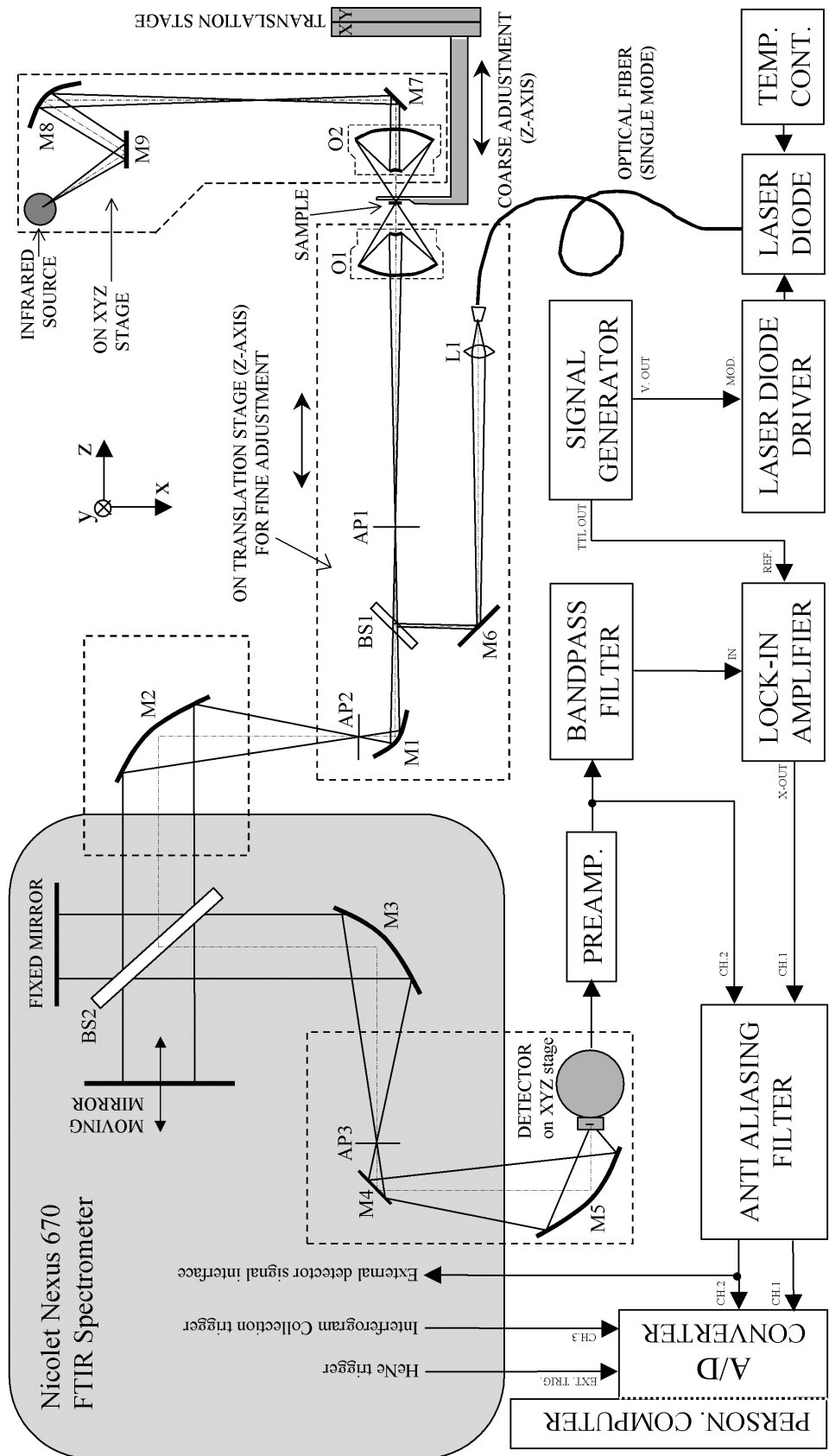


Figure 5.1: Schematic diagram of the experimental apparatus.

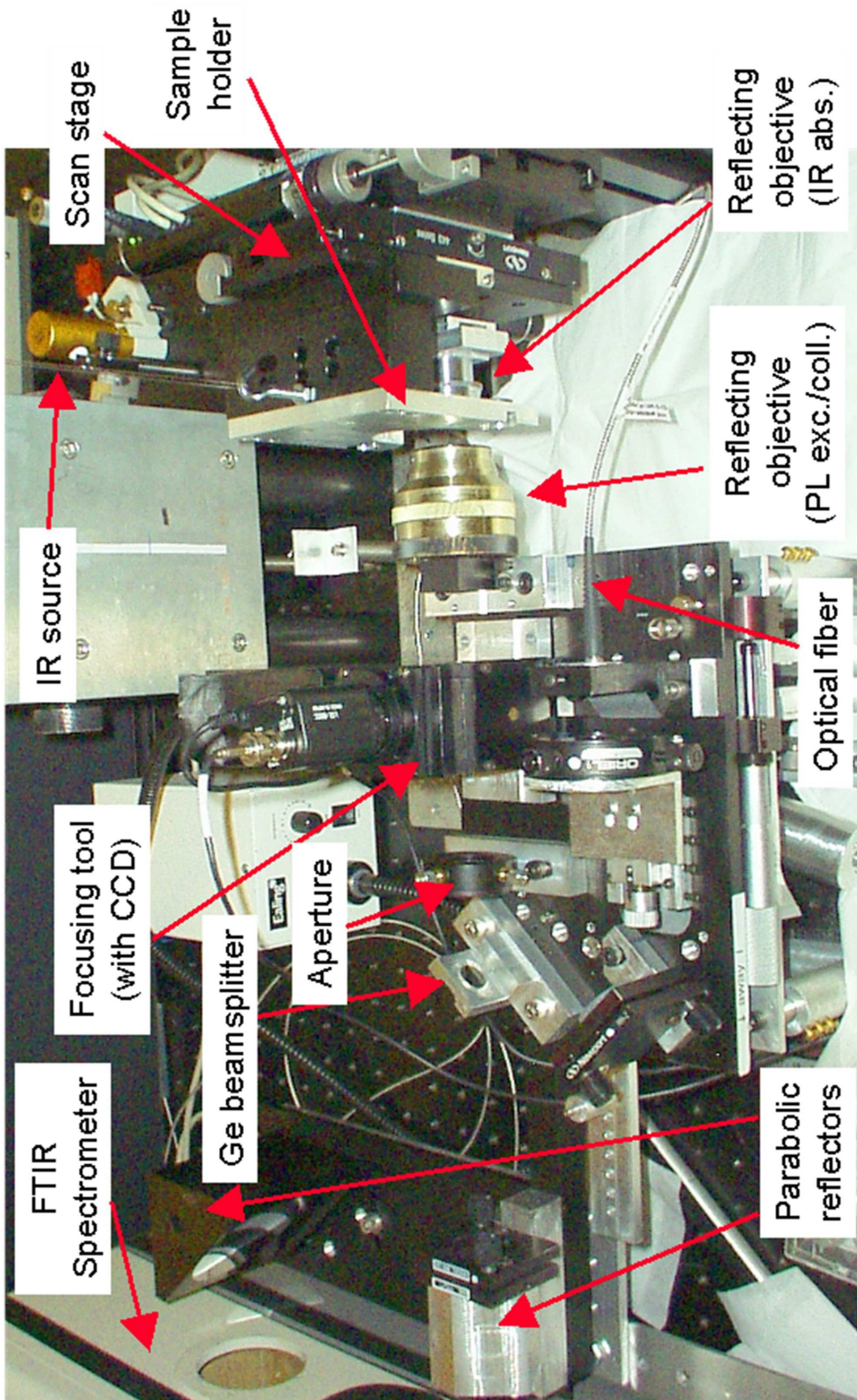


Figure 5.2: The experimental setup.

the sample compartment and refocused onto the detector by an ellipsoidal mirror M5. An aperture (AP3) is used (especially in transmittance measurements) to reduce the effects of the stray background blackbody radiation.

For room temperature measurements, there is the option of measuring transmittance spectra (along with PL) by coupling in broadband IR radiation through the backside of the sample with a reflecting objective O2.

For low temperature experiments, two options exist. For PL imaging, a liquid nitrogen cooled dewar (Kadel) can be attached to the translation stages. Without the imaging capability, PL can be measured from  $\approx 4\text{K}$  to  $300\text{K}$  using a liquid helium flow cryostat (APD Cryogenics). In the latter case, O1 is replaced with a ZnSe lens and O2 is omitted. This low-NA geometry is less sensitive to sample vibrations in the flow cryostat and has a longer working distance. In this configuration, it is also possible to measure transmittance and photo-transmittance, by coupling in the IR source radiation.

FTIR spectrometers are normally used for only measuring the absorbance and transmittance of materials and for this purpose detectors with active element areas of  $1 - 4\text{mm}^2$  are adequate. In order to measure PL with sufficient signal-to-noise ratio (SNR), we use a liquid nitrogen cooled HgCdTe detector (Infrared Associates) with a detector area size of  $100 \mu\text{m}$  and  $D^* = 5 \times 10^{10} \text{cmHz}^{1/2}\text{W}^{-1}$  at  $\lambda_{peak} = 12\mu\text{m}$  (useful range:  $2 - 13\mu\text{m}$ ). The noise equivalent power of a detector is given by

$$NEP = \frac{\sqrt{A}}{D^*} \quad (5.1)$$

where  $D^*$  depends on the temperature and detector material, but not geometry. Eq. 5.1 clearly demonstrates the need for small area detectors. However, switching to a small area detector makes the system much more sensitive to alignment

and aberrations. It was observed that optical alignment became critical as lot of the PL signal missed the detector element due to large aberrations of even slightly misaligned curved mirrors (paraboloidals and ellipsoidals). If not taken care of, this can cancel out any benefit of having a small area detector. To illustrate this, we have performed ray tracing for the last (most critical) ellipsoidal mirror M5 ( $F_1 = 203.2\text{mm}$ ,  $F_2 = 44.5\text{mm}$ ). An ideal point source placed exactly in the focal point of an ellipsoidal mirror will refocus to an infinitesimally small spot (neglecting wave optics) in its other focal point. By moving away from this ideal position ( either along or perpendicular to the optical axis) the imaged spot becomes finite. We calculated the minimum diameter of the circle containing 90% and 95% of the rays, as a function of the point source distance from the focal point. Results are shown in Fig. 5.3. It is clear that the mirror has to be positioned to within  $\approx 100 \mu\text{m}$  to avoid appreciable signal loss. The position of each mirror (from M1 through M4, except M3 which is part of the FTIR and is therefore fixed) was carefully aligned to minimize aberrations. This was done by placing a white light source from a multimode optical fiber at one of the mirror's focal points (e.g. at AP1 for M1), and a CCD camera (chip only, no lens) in its other focal point (e.g. at AP2 for M1). This way, the aberration spot can be visually minimized. In the last stage, the detector was placed on an XYZ translation stage to bring its active element in the focus of mirror M5.

PL and transmittance signals are superimposed on the stray 300K Planck's blackbody radiation. To some extent, this stray radiation can be eliminated using apertures, which we did for transmittance measurements. For a complete removal (needed in PL and photo-transmittance measurements) a different approach is necessary.

We use the double-modulation technique (Nafie and Diem, 1979). The pri-

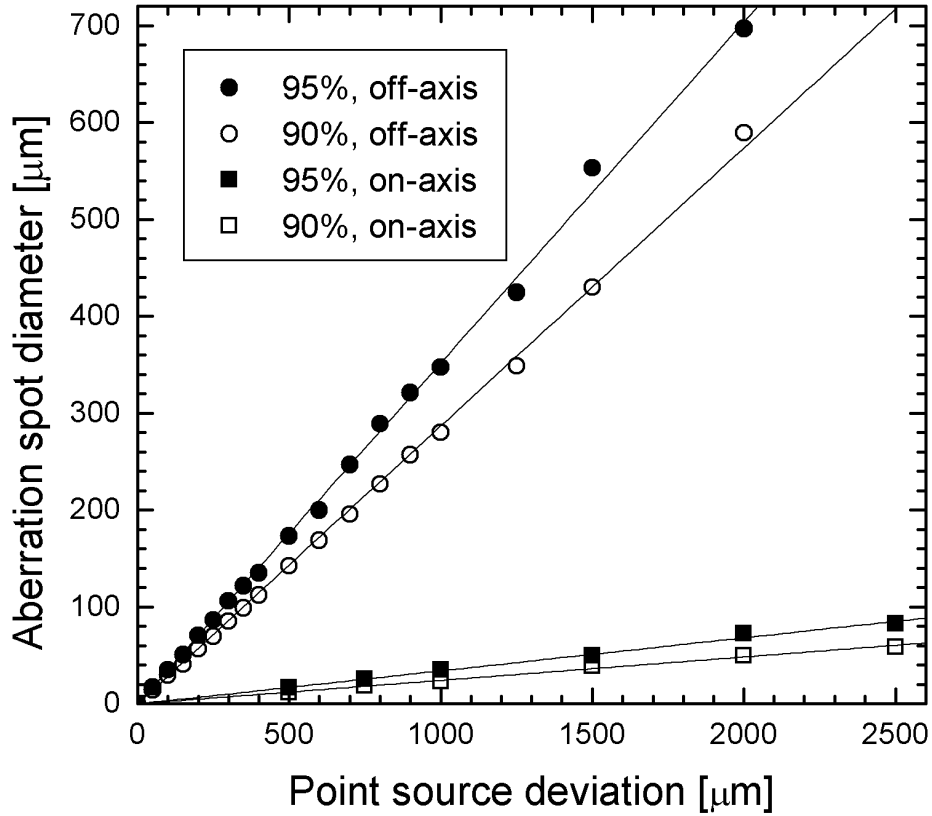


Figure 5.3: The diameters of circles containing 90% and 95% of the aberration spot as a function of a point source ( $NA_1 = 0.125$ ) deviation from the  $F_1$  focal point of a  $90^\circ$  ellipsoidal mirror ( $F_1 = 203.2\text{mm}$ ,  $F_2 = 44.5\text{mm}$ ).

mary modulation comes from the moving mirror of the FTIR spectrometer and is given by

$$f_{mod} = 2v_m\nu \quad (5.2)$$

where  $v_m$  is the mirror velocity (in cm/s) and  $\nu$  the wavenumber (in  $\text{cm}^{-1}$ ). For a mid-IR signal, this is typically in the 100Hz to 1kHz range. The secondary modulation results from the excitation laser which, in order to provide sufficient frequency separation, was modulated at 50-100kHz. The time constant of the lock-in amplifier was chosen such that

$$\tau_{LIA} < \frac{1}{f_{mod,max}} \quad (5.3)$$

The laser power modulation was performed by varying the laser diode current.

The signal (PL plus background) from the detector's wideband preamplifier passes a high-quality 6-pole bandpass active filter (Avens) that removes the low frequency component. The signal then goes into a digital lock-in amplifier (Stanford Research Systems, SR830). The output of the lock-in amplifier and the output of the preamplifier (containing either the transmittance signal or just stray background radiation - when the apertures A2 and A3 are removed) pass through an anti-aliasing low-pass active filter and into an analog to digital (A/D) converter (Data Translation, DT321). The A/D converter was triggered by a TTL signal provided by the FTIR that tracks the interference of an internal HeNe laser. This way, two interferograms were collected in parallel and stored on a hard drive by the control software. The importance of collecting both the PL and transmittance/background radiation signal lies in the fact that the PL interferograms are usually very noisy and do not have the clear zero-path-difference (ZPD) signal necessary for coherent addition subsequent interferograms. The background radiation signal is usually strong enough to yield

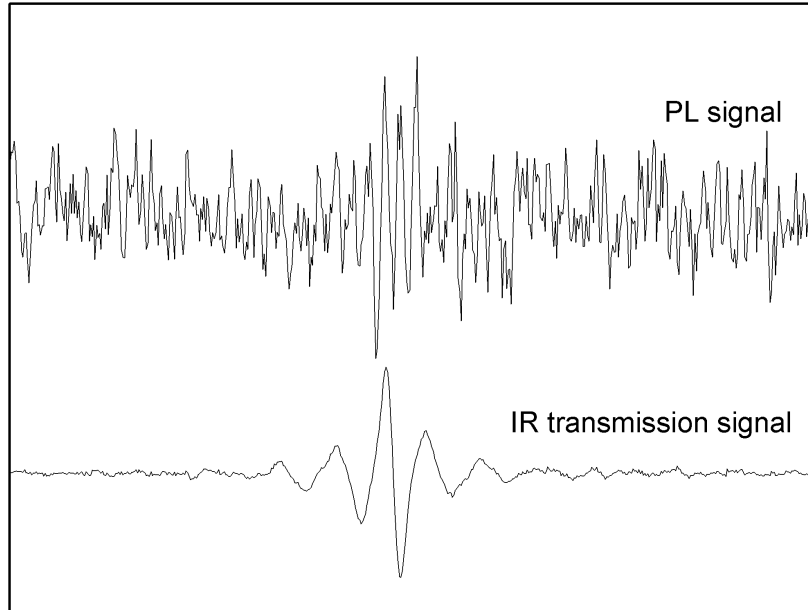


Figure 5.4: Signal quality comparison of photoluminescence and transmission interferograms in a typical room-temperature high-spatial resolution imaging experiment.

a clear ZPD. Figure 5.4 shows typical room-temperature PL and transmission interferograms in a high-spatial resolution PL imaging experiment. The ZPD point is associated with the maximum value of the interferograms. The sample was a MBE grown mid-IR  $\text{Hg}_{1-x}\text{Cd}_x\text{Te}$  ( $x=0.3$ ) epilayer on bulk  $\text{Cd}_{0.96}\text{Zn}_{0.04}\text{Te}$  from HRL Laboratories. Since the PL and background radiation interferograms are collected with the same interferometer, their ZPDs occur at the same time (or with the same time interval, since there might be a constant time lag due to their passage through different electronic circuits). Apart from sending it to the A/D converter, the background radiation signal is also passed back to the FTIR. The reason for this is because the Nicolet Nexus FTIR relies on a strong IR signal (always present in absorption measurements) to determine the ZPD. A weak PL signal is too noisy for this purpose.

Once the interferograms are collected, they are coherently added for every

point in the image, followed by apodization, phase correction (Griffiths and de Haseth, 1986, Furstenberg and White, 2005) and a fast Fourier transform (FFT) to get the spectra. These spectra can then be analyzed and parameters extracted to form various images.

The minimum acquisition time for one spectrum is limited by the mirror velocity and spectral resolution. For the slowest mirror velocity of  $v_{min} = 0.1581\text{cm/s}$  and resolution of  $\Delta\nu = 16\text{cm}^{-1}$ , the acquisition time is  $\approx 0.5\text{s}$  for one interferogram. For most mid-IR images in this work, 16 interferograms per image point were collected.

### **5.1.1 Phase correction of interferograms in photo-transmittance experiments**

In a photo-transmittance/photo-reflectance experiment one measures the change in transmittance/reflectance of the sample as a result of the presence of an electric field from a laser (Aspnes, 1980). The quantity  $\Delta T(\lambda)$  (or  $\Delta R(\lambda)$ ) is the direct output of a lock-in amplifier obtained by measuring the spectrally resolved (using a diffraction grating) transmittance/reflectance while the sample is illuminated with a modulated laser. As such, it can acquire both positive and negative values.

When an FTIR spectrometer is used to measure PT or PR, the output of the lock-in amplifier in the double-modulation configuration is not a constant, but a changing signal (both positive and negative values) whose temporal signature represents an interferogram. The spectrum is then obtained by FFT. The sign of  $\Delta T(\lambda)$  is contained not in the sign of the lock-in output, but rather in the phase of the FFT transform. The FFT phase curve in Fig. 5.5 shows several

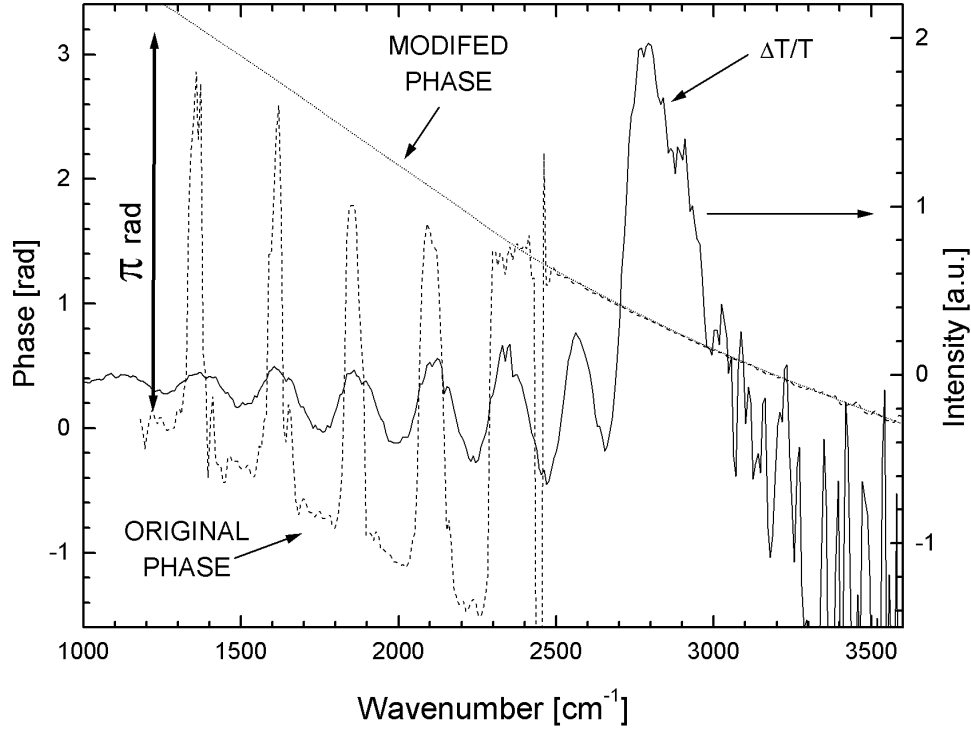


Figure 5.5: Interferogram phase curve and photo-transmittance spectrum of the  $\text{Hg}_{0.7}\text{Cd}_{0.3}\text{Te}$  sample.

jumps of  $\pi$  rad, which corresponds to sign change in the spectral domain. In this case a special phase correction procedure is needed lest the Fourier transformed  $\Delta T$  spectrum loses the information about the sign (i.e. becomes all positive).

There are several ways of doing this. Here we present two.

The first method uses all-pass digital filters (Furstenberg and White, 2005, Furstenberg and White, 2006). Since the phase spectrum is a slowly varying function of wavenumber, especially in the limited range of a PT spectrum, we design a low-order all-pass digital filter whose phase delay is the opposite of the interferogram's phase curve. This way, once applied, the phase curve of the interferogram is removed and the true spectrum is contained in the cosine (i.e. real) part of the FFT transform. In order to ignore the  $\pi$  rad phase jumps and

thus allowing the spectrum to have negative values, the  $\chi^2$  function used in the design of the all-pass filter is slightly modified,

$$\chi^2 = \sum_{\nu=\nu_{min}}^{\nu_{max}} [\min(|\theta_{filt.} + \theta_{interf.}|, |\theta_{filt.} + \theta_{interf.} + \pi|)]^2 \quad (5.4)$$

Another method suggested in (Furstenberg and White, 2005) is to choose a digital all-pass filter that minimizes the imaginary part of the Fourier transform in the spectral region of interest. This method is slightly slower, but can be applied without any modifications. This method was used in this work. Phototransmittance can be used to determine the bandgap of  $\text{Hg}_{1-x}\text{Cd}_x\text{Te}$  epilayers. Currently, the bandgap of  $\text{Hg}_{1-x}\text{Cd}_x\text{Te}$  is determined by analyzing the absorption curve around the bandgap (Moazzami et al., 2003, Chang et al., 2004, Ariel et al., 1997).

## 5.2 Near-infrared setup

To measure photoluminescence spectra of CdTe and similar materials with PL in the near-IR a different, more efficient setup is used. The same microscopic attachment used for mid-IR signals is used but instead of to the FTIR, the signal is sent into a grating spectrometer and imaged onto a cooled CCD camera (Princeton Research). The excitation laser is introduced via free space propagation through a small cube beamsplitter in the place of the aperture. The Ge beamsplitter is replaced by a mirror. The signal is focused on a multimode optical fiber that is in the same position as the excitation laser fiber for the mid-IR setup. The fiber is then connected to the spectrometer.

At an earlier stage of the project, near-IR spectra were also measured using a Witec Alpha 2000 microscope as shown in Figure 5.6. However, this setup

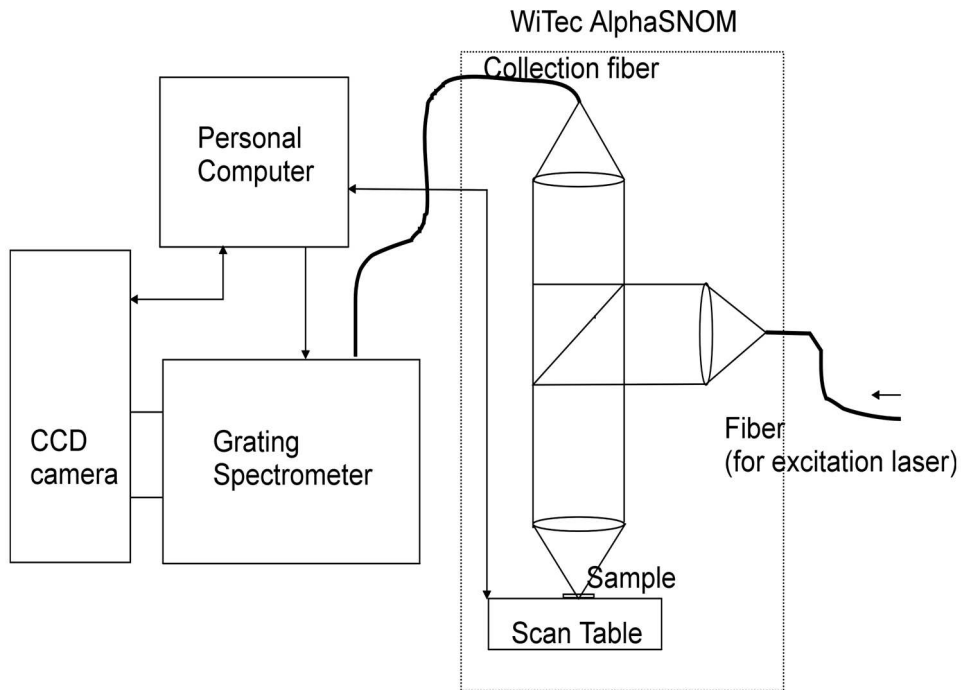


Figure 5.6: High resolution near-IR photoluminescence setup.

had limited scan range ( $100\mu\text{m}$ ) and was replaced in favor of the one described above.

# Chapter 6

## Photoluminescence

### Imaging Study of

### $\text{Hg}_{1-x}\text{Cd}_x\text{Te}$

#### 6.1 Introduction

Visible and near-IR photoluminescence (PL) in semiconductors and other materials has long been successfully used to identify and image defects as well as in assessing the overall sample quality. Photoluminescence spectroscopy or imaging is a non-destructive technique requiring little or no sample preparation. For materials with a PL signal in the visible and near-IR region of the spectrum, a large number of reports can be found in the literature (Sochinskii et al., 2004, Pernot et al., 2003, Ardila et al., 2002, Stavola, 1999, Arakawa et al., 1996, Petruzzello et al., 1995, Haugen et al., 1999, Vetter and Winnacker, 1991, Molva et al., 1990, Alt et al., 1989, Bishop et al., 1989, Kazmierski et al., 1985).

Commercial systems based on diffraction gratings are now widely available, facilitating the application of PL as a valuable characterization tool.

For infrared semiconductor materials the situation is quite different, and only a few reports exist on infrared PL as a materials characterization tool (Wolny et al., 1994, Schmidt et al., 1990, Fuchs et al., 1990, Chang et al., 2000). Consequently, photoluminescence characterization is by no means routinely used for narrow-gap materials as is by now the case for wide-gap materials. With the experimental setup described in the previous chapter, we were able to perform photoluminescence imaging for both wide and narrow-gap II-VI semiconductor materials.

## 6.2 Spatially Resolved Photoluminescence of Bulk CdTe and CdZnTe

Bulk  $\text{Cd}_{0.96}\text{Zn}_{0.04}\text{Te}$  is the best choice of substrate for MBE growth of  $\text{Hg}_{1-x}\text{Cd}_x\text{Te}$  epilayers. By adding small amounts of Zn in CdTe, perfect lattice matching can be achieved. However, large substrates are expensive and hard to fabricate. With the increased need for larger substrates for the growth of large focal plane arrays, alternative substrates are being studied. Silicon as one of the most ubiquitous substrates is a natural candidate. Focal plane arrays used silicon based readout circuits (ROIC) and the use of silicon substrates does not cause thermal cycling related breakdown of FPA pixel bonds with ROIC, as is often the case when bulk  $\text{Cd}_{0.96}\text{Zn}_{0.04}\text{Te}$  substrates are hybridized with silicon ROIC. The problem, however, in using silicon lies in a large, 19% lattice mismatch between  $\text{Hg}_{1-x}\text{Cd}_x\text{Te}$  and Si. To remedy this, buffer layers are grown to reduce and trap dislocations. As photoluminescence is sensitive to defects present in the mate-

rial, it can be a viable tool in the optimization process of these  $\text{Hg}_{1-x}\text{Cd}_x\text{Te}$  epilayers grown on silicon substrates.

### 6.3 Room Temperature Photoluminescence

First, we study the usefulness of using room temperature photoluminescence. Although all analysis of 300K PL peaks in this section were of CdTe and  $\text{Cd}_{0.96}\text{Zn}_{0.04}\text{Te}$ , it equally applies to  $\text{Hg}_{1-x}\text{Cd}_x\text{Te}$  with PL peaks in the mid-IR. The shape of the peaks is also quite similar, the only difference being their positions.

The main advantage of using high temperatures is primarily the lack of additional sample handling associated with applying thermal grease to attach the sample to the cold finger, and the possibility of doing these measurements in-situ in the MBE growth chamber, without the risk of sample contamination. The disadvantages are obvious, and stem from the lack of sharp spectral features due to the increased importance of phonon interactions at high temperatures. Also, the PL signal at 300K is much weaker than the corresponding signal at low temperatures. This decrease of PL strength is increasingly more pronounced with the narrowing of the bandgap.

Figure 6.1 shows a typical spectrum of  $\text{Cd}_{0.96}\text{Zn}_{0.04}\text{Te}$  at 300K. The band edge photoluminescence consists of a single, broad peak without any apparent features. The analysis of room temperature PL is therefore restricted, and involves measuring total PL peak intensity (integrated PL), and some other parameters related to the spectral position of the band edge photoluminescence. These are the PL peak, center of mass of the PL, PL FWHM and the so called  $\lambda_{1/2-MAX}$ . This last quantity is often used as an estimator of peak position

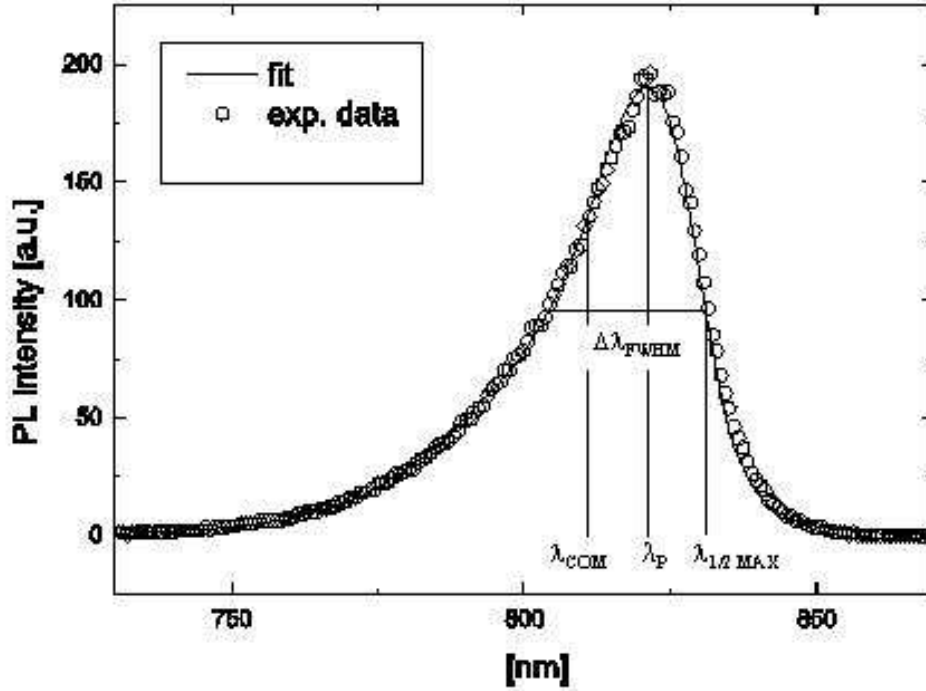


Figure 6.1: Typical room temperature spectrum of  $\text{Cd}_{0.96}\text{Zn}_{0.04}\text{Te}$  .

because it was found to be less dependent on the excitation laser intensity (Bassignana et al., 1989).

To give an example of imaging various band edge PL parameters, we obtained 300K PL spectra of a bulk  $10\text{mm} \times 10\text{mm}$  CdTe sample with a spatial resolution of  $50\mu\text{m}$ .

For each data point, spectra were analyzed and fitted and the four PL parameters discussed above were imaged. Peak fitting is needed for the determination of FWHM,  $\lambda_{1/2-MAX}$  and  $\lambda_{PEAK}$ .  $I_{PL}$  and  $\lambda_{COM}$  do not require fitting, as they are given by simple formulas

$$I_{PL} = \int_{\lambda_{MIN}}^{\lambda_{MAX}} d\lambda I(\lambda) \quad (6.1)$$

and

$$\lambda_{COM} = \frac{\int_{\lambda_{MIN}}^{\lambda_{MAX}} d\lambda \lambda I(\lambda)}{\int_{\lambda_{MIN}}^{\lambda_{MAX}} d\lambda I(\lambda)} \quad (6.2)$$

The wings of the room temperature PL spectra have a strong exponential behavior (with different slopes) with a transition region around the peak. In order to obtain a PL image, large number of spectra need to be processed in a reasonable amount of time. In order to achieve this, a linear fitting scheme is adopted in favor of physical models (Lee et al., 1994) that would require time-consuming non-linear fits. We use a multivariate cubic spline regression to model the PL peak as:

$$I_{PL}(\lambda) = \exp \left( c_0 + c_1 \lambda + c_2 \lambda^2 + c_3 \lambda^3 + \sum_{j=0}^{N_k-1} c_{j+4} ([\lambda - \lambda_j]_+)^3 \right) \quad (6.3)$$

where  $N_k$  is the number of knots (break points) of the spline,  $\{c_0, c_1, \dots, c_{n_k-1}\}$  are the fitting parameters, and  $[\lambda - \lambda_j]_+$  is defined as:

$$[\lambda - \lambda_j]_+ = \begin{cases} \lambda - \lambda_j & \text{for } \lambda \geq \lambda_j \\ 0 & \text{for } \lambda < \lambda_j \end{cases} \quad (6.4)$$

This notation of cubic splines is particularly conducive to statistical analysis, especially to the estimation of errors of the fitting parameters and various parameters of the PL peak. The number of knots and their position determine the quality of the fit. We used 6 knots (10 free parameters) for the  $\text{Cd}_{0.96}\text{Zn}_{0.04}\text{Te}$  peak and got a nearly perfect overlap with the experimental data as can be seen in Figure 6.1. The distribution of knots was not fully optimized. Knots were chosen to accumulate around the transition region of the peak where the most discrepancies between fit and experimental data were observed. Optimizing the

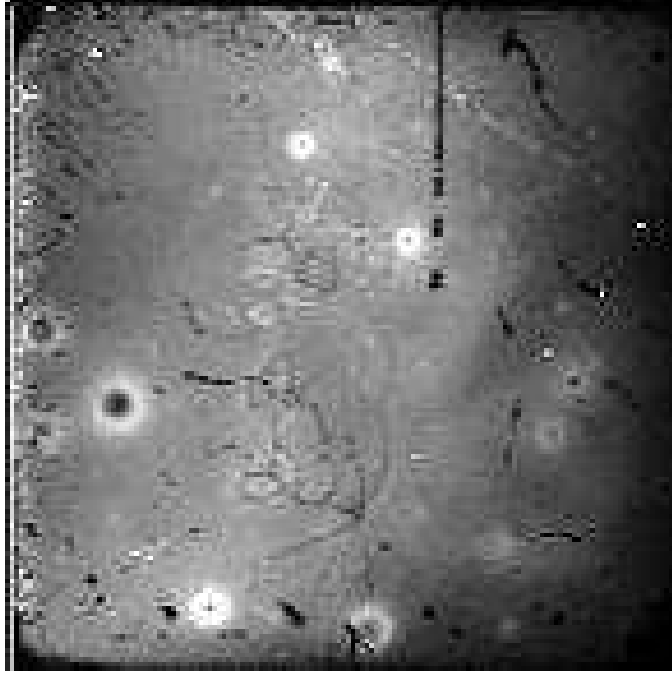


Figure 6.2: PL image of bulk CdTe. Imaged quantity is  $I_{PL}$ .

knot positions (through non-linear fitting) might improve the overall fit quality and even reduce the number of knots needed.

Figures 6.2 through 6.5 show the grayscale images representing the spatial variation of the various PL parameters.

Overall, the images are slightly different in each case. Figure 6.2 that represents the total PL intensity. It is evident that this quantity is most dependent on experimental conditions. Any changes in the excitation laser power as well as the changes in collection efficiency (mostly from slight tilt of the sample) are readily registered in the images. This is in sharp contrast with Figure 6.5 that shows the quantity  $\lambda_{1/2-MAX}$  which is mostly independent of both collection

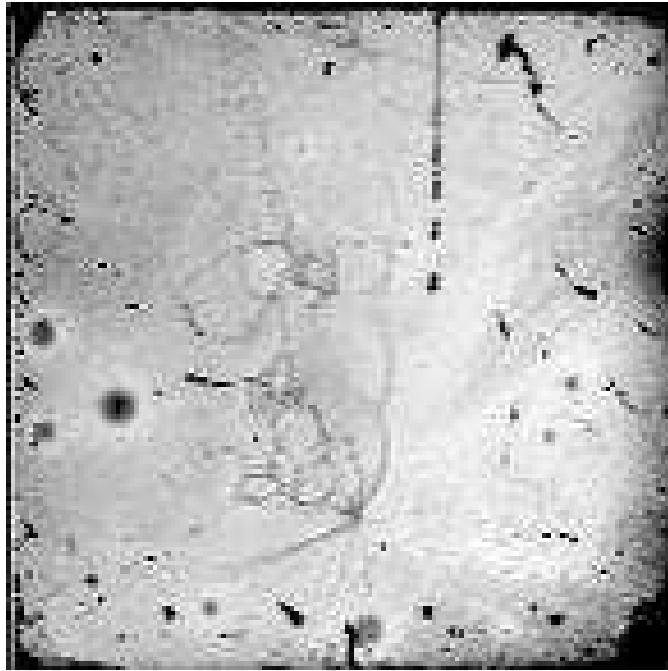


Figure 6.3: PL image of bulk CdTe. Imaged quantity is  $\lambda_{COM}$ .

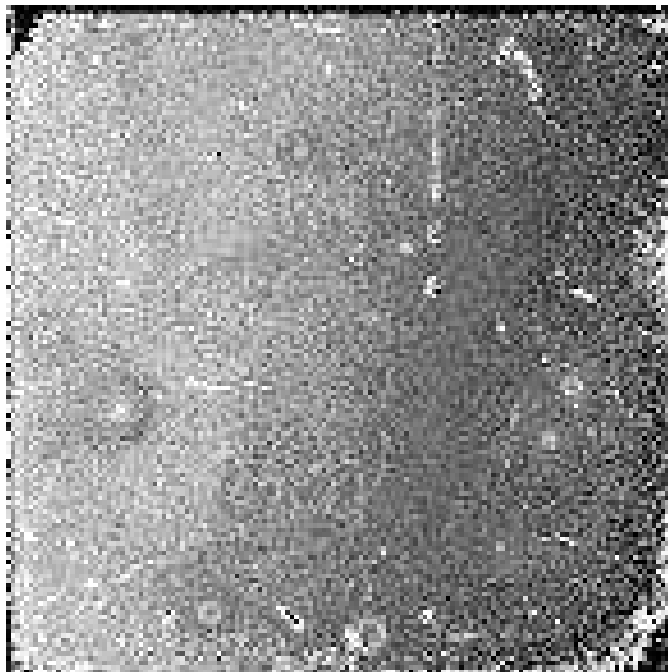


Figure 6.4: PL image of bulk CdTe. Imaged quantity is  $\Delta\lambda_{FWHM}$ .

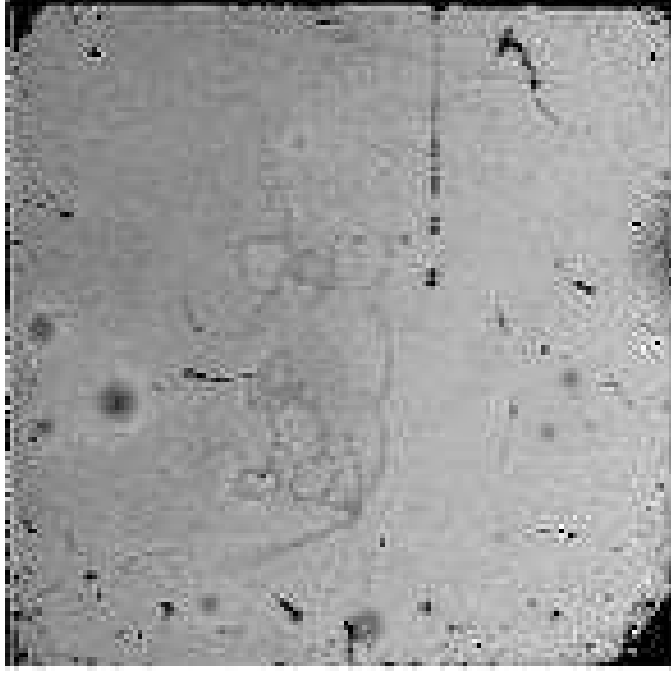


Figure 6.5: PL image of bulk CdTe. Imaged quantity is  $\lambda_{1/2-MAX}$ .

efficiency and excitation power density. This illustrates the need to collect full PL spectra for each data point and not just the total PL signal (as is usually done). Figure 6.3 shows the  $\lambda_{COM}$ . This quantity correlates well with  $\lambda_{1/2-MAX}$  in Fig. 6.5, and can be used as an alternative to  $\lambda_{1/2-MAX}$  since it does not require any special fitting procedures.

## 6.4 High spatial resolution photoluminescence imaging of CdTe at 300K

In order to characterize growth related defects in CdTe/Cd<sub>0.96</sub>Zn<sub>0.04</sub>Te we performed high-spatial resolution photoluminescence imaging at room temperature of two different substrates: one high quality Cd<sub>0.96</sub>Zn<sub>0.04</sub>Te bulk substrate and a MBE-grown CdTe epilayer on silicon wafer.

Figure 6.6 shows a 24 $\mu$ m by 24 $\mu$ m region of CdTe/Si at 300K imaged with

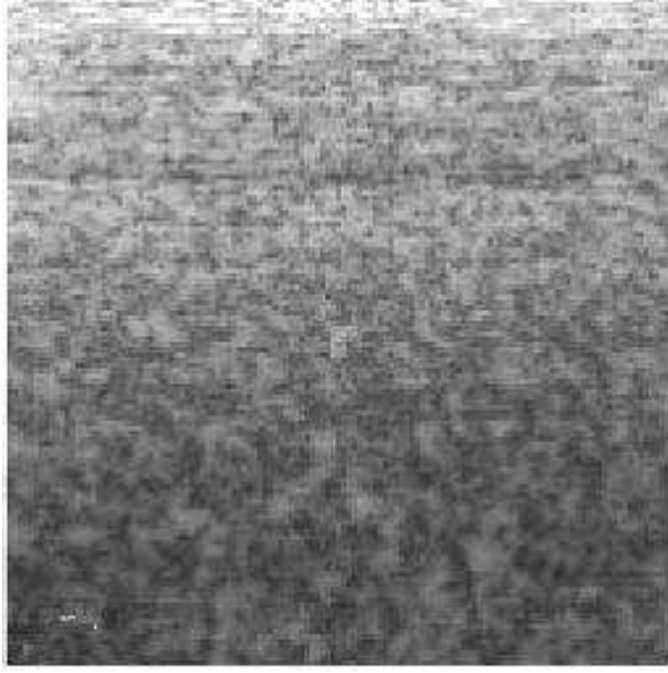


Figure 6.6: High resolution PL image of CdTe/Si.

a diffraction-limited resolution (500nm). The imaged PL peak parameter was  $\lambda_{1/2-MAX}$ . The image appears to be rough with islands of  $\approx 2\mu\text{m}$  in diameter. If we look at a cross section along a horizontal line in the middle of the image (Fig. 6.7), we can see the rapid changes of  $\lambda_{1/2-MAX}$ . Since the material is CdTe (no possibility of alloy composition fluctuations) we conclude that  $\lambda_{1/2-MAX}$  can be correlated with the local density of dislocations that develop as a result of large lattice mismatch between CdTe and the silicon substrate. In contrast, Figure 6.8 shows a high quality epi-ready bulk  $\text{Cd}_{0.96}\text{Zn}_{0.04}\text{Te}$  substrate. A  $24\mu\text{m}$  by  $24\mu\text{m}$  region, with diffraction limited resolution. Apart from the obvious etch pit in the center of the image,  $\lambda_{1/2-MAX}$  is relatively constant. A cross section running along the etch pit is shown in Figure 6.9 and is plotted with the same vertical scale to allow for direct comparison with Figure 6.7.

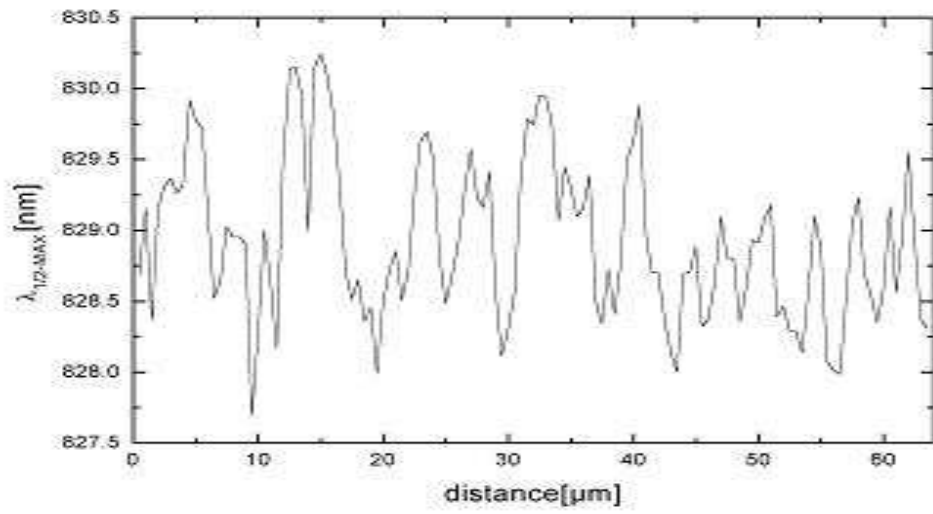


Figure 6.7: Cross section of the PL image.

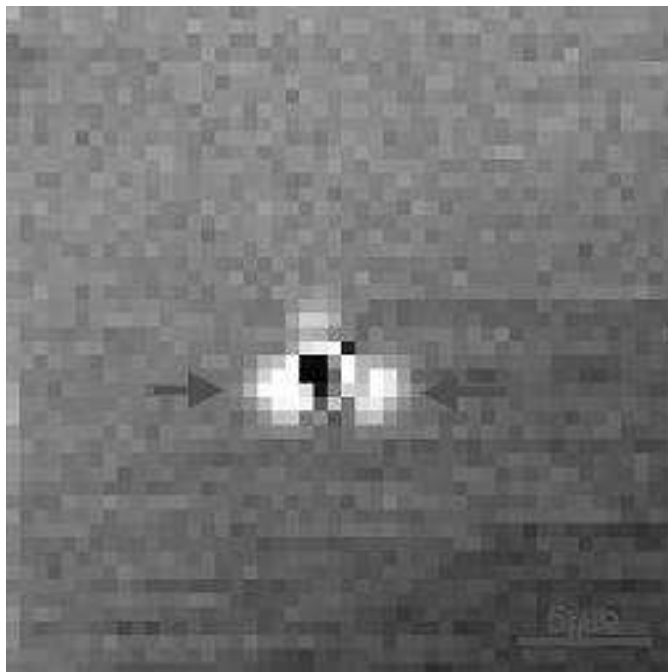


Figure 6.8: High resolution PL image of high quality  $\text{Cd}_{0.96}\text{Zn}_{0.04}\text{Te}$ .

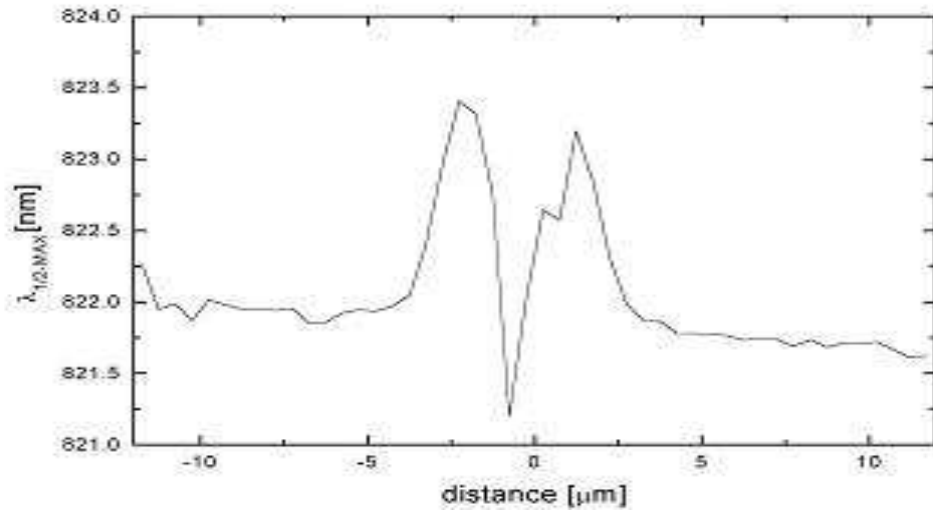


Figure 6.9: Cross section of the PL image.

## 6.5 Medium resolution photoluminescence imaging of CdTe and Cd<sub>0.96</sub>Zn<sub>0.04</sub>Te at 77K

In order to study large defects that extend several 10's or 100's of microns and to examine their distribution across a large wafer, the resolution of PL images needs to be adequately reduced or otherwise the images would take a prohibitively long time to acquire. A resolution of 10-50μm proved to be adequate for this task.

We used this technique to compare bulk CdTe and Cd<sub>0.96</sub>Zn<sub>0.04</sub>Te substrates with different quality levels of surface preparation. The preparation of good surfaces for MBE growth is very challenging and currently a considerable amount of effort is being made to produce high quality epi-ready Cd<sub>0.96</sub>Zn<sub>0.04</sub>Te substrates (Singh et al., 2005).

We will show that photoluminescence can be used to evaluate the surface quality and thus aid in the optimization of the chemo-mechanical polishing procedure.

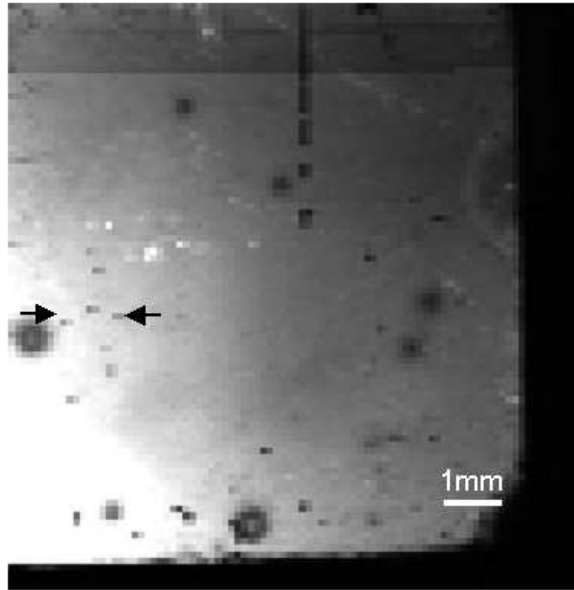


Figure 6.10: PL image of bulk CdTe with surface damage ( PL spectrum integrated from 760nm to 790nm).

Two samples of widely differing surface quality were scanned at liquid nitrogen temperatures. One was a CdTe sample with an inferior surface preparation and the other was the state-of-the-art  $\text{Cd}_{0.96}\text{Zn}_{0.04}\text{Te}$  substrate from Nikko Materials, Japan.

At 77K, the band edge PL has two distinct peaks. One is the band-to-band recombination ( $e - h$ ) and the other consist of one or more deep defect centers.

Figure 6.10 shows the spatial distribution of the ( $e - h$ ) peak of the low-quality sample (image obtained by integrating the spectrum from 760nm to 790nm). Figure 6.11 shows the spatial distribution of the deep defect band peak of the low-quality sample (image obtained by integrating the spectrum from 800nm to 920nm). Two representative spectra from the image are shown in figures 6.12 and 6.13. Figure 6.14 shows the spatial distribution of ( $e - h$ ) peak of the high-quality sample (image obtained by integrating the spectrum

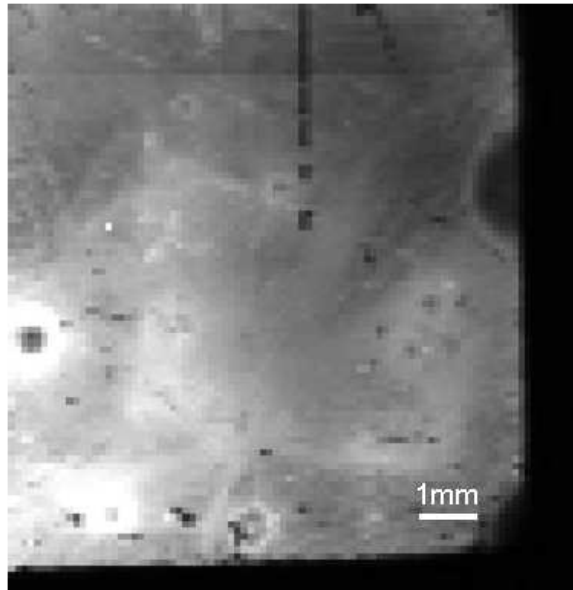


Figure 6.11: PL image of bulk CdTe with surface damage ( PL spectrum integrated from 800nm to 920nm).

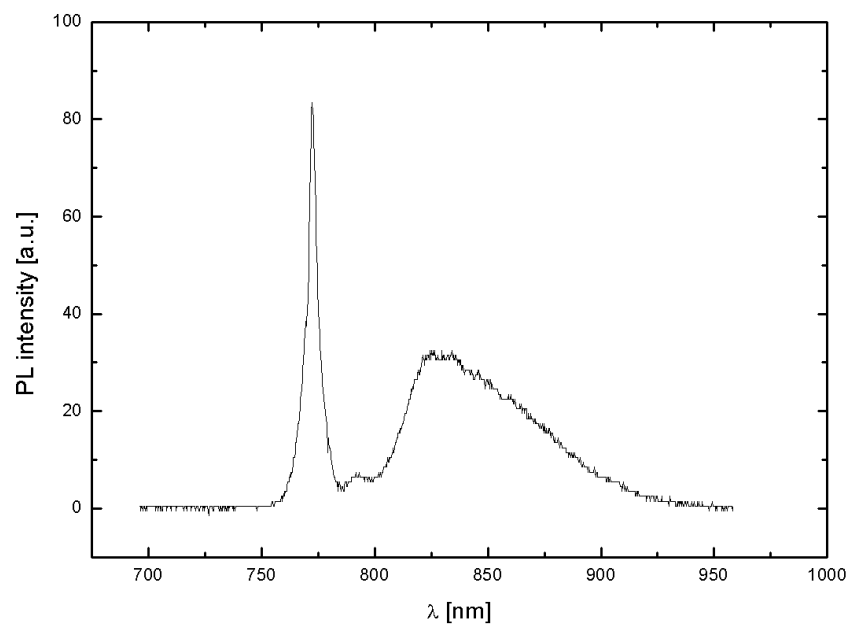


Figure 6.12: A representative spectrum from a high quality portion of the CdTe sample.

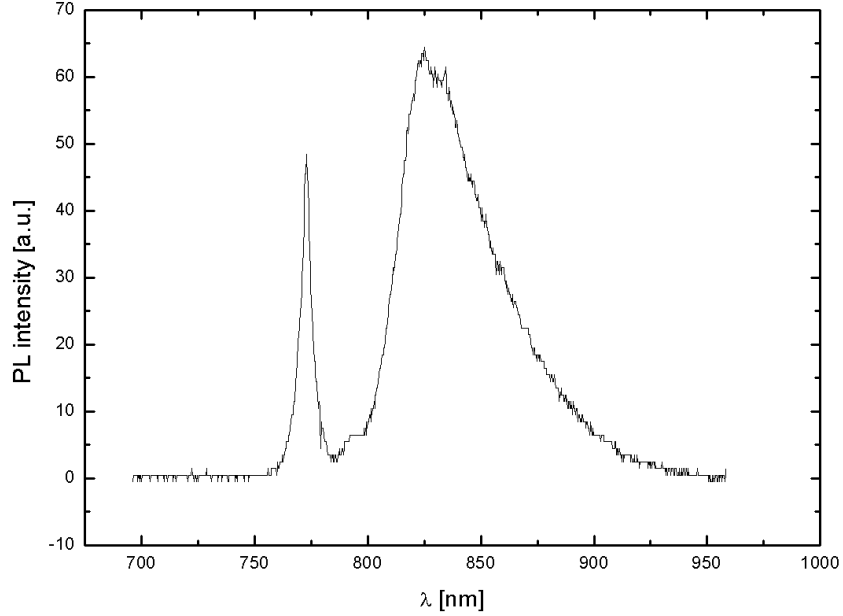


Figure 6.13: A representative spectrum from a low quality portion of the CdTe sample.

from 760nm to 790nm). Figure 6.15 shows the spatial distribution of the deep defect band peak of the high-quality sample (image obtained by integrating the spectrum from 800nm to 920nm). Two representative spectra from the image are shown in figures 6.16 and 6.17. It can be seen (both from the images and representative spectra) that the second sample is of much higher quality and the defect band peak is barely present. In sharp contrast to this, the low-quality sample has a defect band comparable in strength to the  $(e - h)$  peak. This strongly suggests that the deep center defect band is related to growth related native defects (such as cadmium vacancies and tellurium interstitials) and can be used to monitor the substrate surface quality.

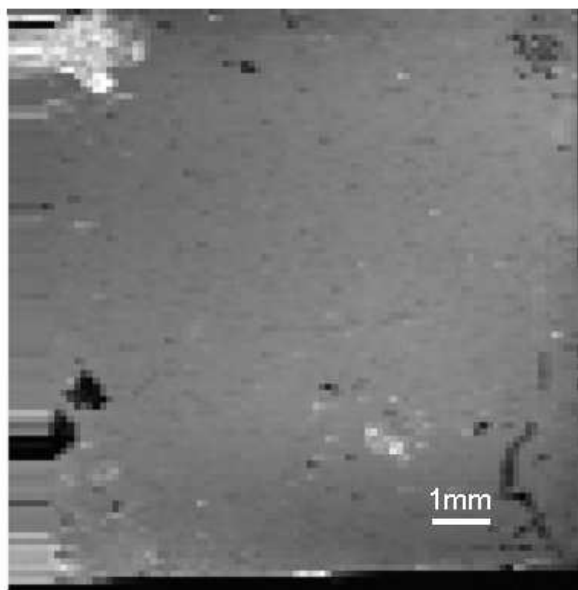


Figure 6.14: PL image of bulk Cd<sub>0.96</sub>Zn<sub>0.04</sub>Te with high surface quality ( PL spectrum integrated from 760nm to 790nm).

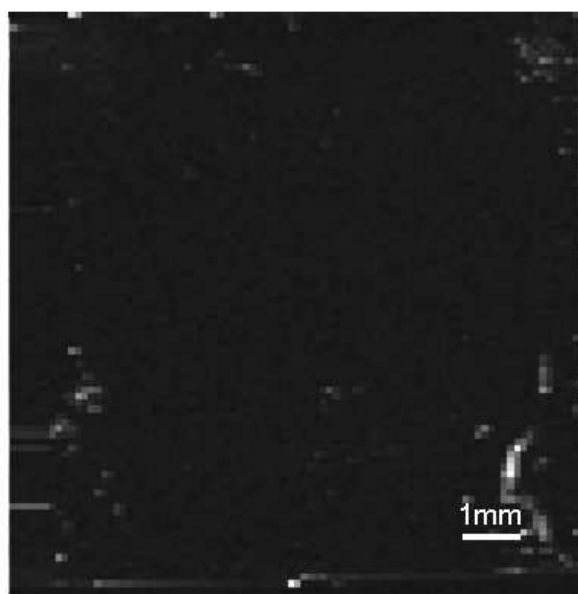


Figure 6.15: PL image of bulk Cd<sub>0.96</sub>Zn<sub>0.04</sub>Te with high surface quality ( PL spectrum integrated from 800nm to 920nm).

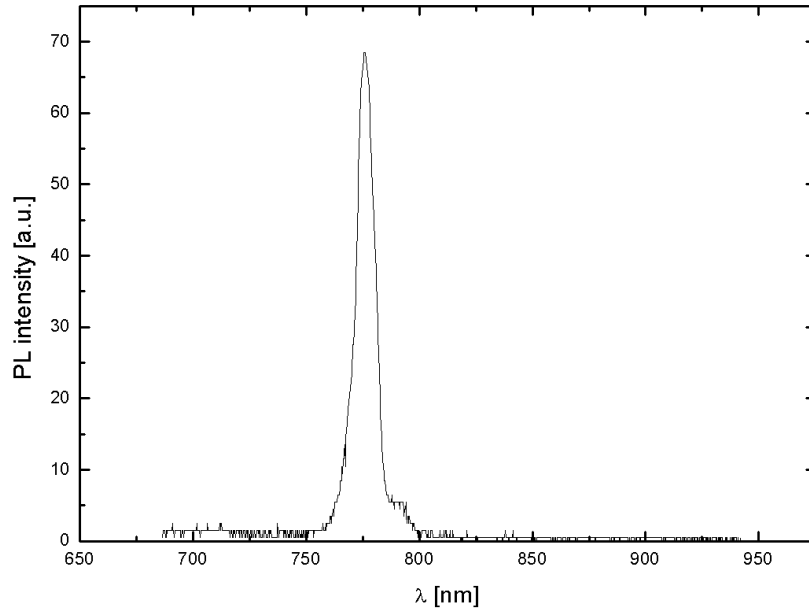


Figure 6.16: A representative spectrum from a high quality portion of the  $\text{Cd}_{0.96}\text{Zn}_{0.04}\text{Te}$  sample.

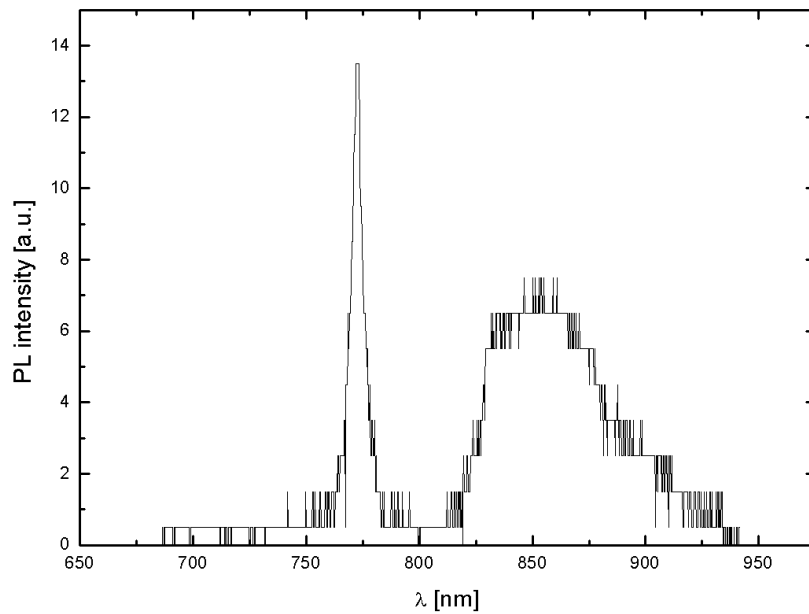


Figure 6.17: A representative spectrum from a low quality portion of the  $\text{Cd}_{0.96}\text{Zn}_{0.04}\text{Te}$  sample.

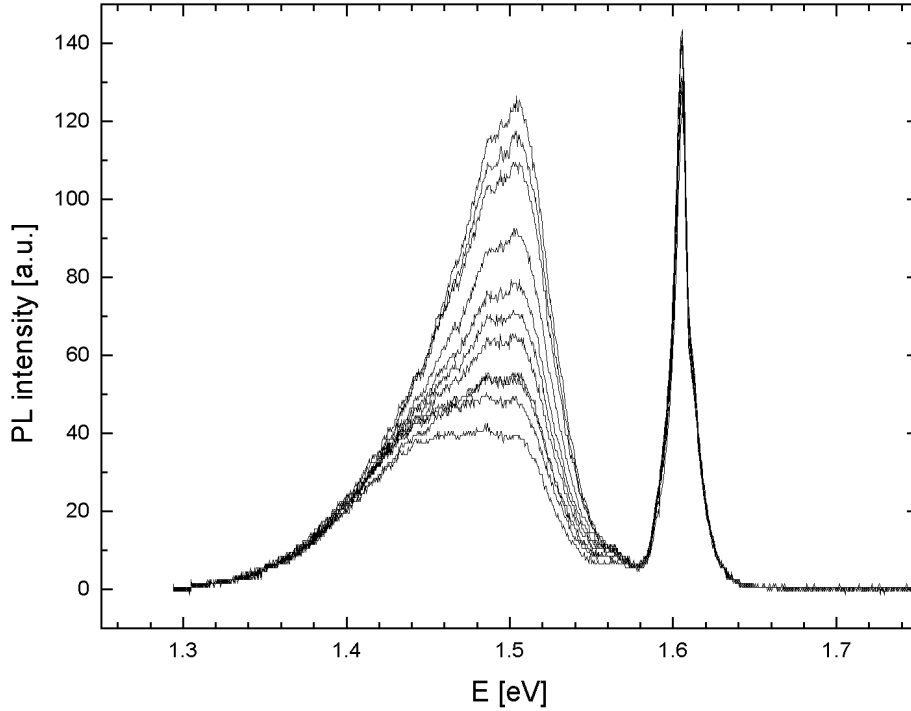


Figure 6.18: Spatial variation of the photoluminescence spectra of the CdTe sample.

## 6.6 Analysis of photoluminescence spectra in CdTe

The shape of the photoluminescence spectrum in figure 6.13 clearly indicates the presence of several defect level transitions. The strong peak at 1.6eV and a weaker shoulder at 1.57eV are obvious. The shape of the broad region 1.3eV-1.56eV suggests the presence of more than one transition. This becomes evident as we analyze the shape of the band as a function of position on the sample. In figure 6.18 a series of PL spectra shows this change. The spectra are from 12 points on a line indicated by arrows in figure 6.10. The change in shape can be attributed to the change in contribution (intensity) of the distinct defect levels.

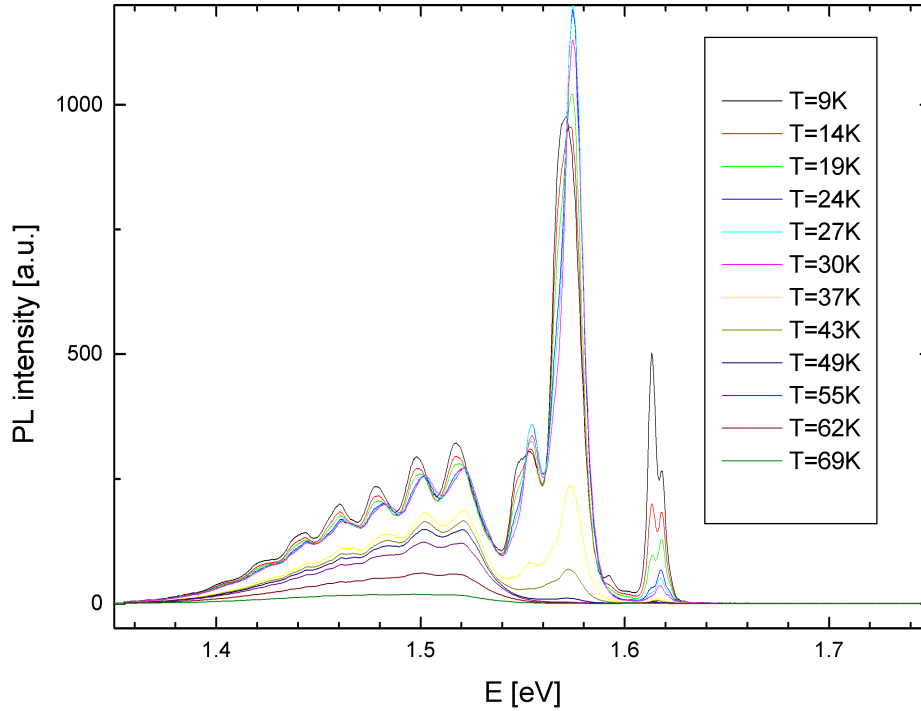


Figure 6.19: Temperature dependence of the photoluminescence spectra of CdTe.

Also, attempts to model the data with only one or two transitions yielded a poor fit. In what follows we will attempt to derive the transition energies for these levels.

In order to decide what the most appropriate model for a defect level transition is, we examine the temperature dependence of the PL spectrum from a large spot on the sample. With the current setup we can only perform imaging at 77K.

Figure 6.19 shows PL spectra for several temperatures. One can see that the defect band consists of several phonon replicas ( $\hbar\omega_{LO} = 21\text{meV}$ ). At low temperature, these replicas are resolved, but at higher temperatures (including 77K) they blend into one broad peak. At low temperatures, the line shape of a

defect level transition is given by the Poisson distribution:

$$I(\nu - \nu_0) = \sum_{n=0}^{\infty} \frac{S^n}{n!} \exp(-S) g(\nu - \nu_0 - \frac{\omega_{LO}}{2\pi} n) \quad (6.5)$$

where  $n$  is the number of phonons emitted at the specific transition,  $S$  is the Huang-Rhys factor and  $g$  is the line shape of the transition (usually represented by a Gaussian), where

$$g(\nu - \nu_0) = \frac{1}{\sqrt{2\pi}\gamma} \exp -\frac{\nu - \nu_0^2}{2\gamma} \quad (6.6)$$

At higher temperatures, the phonon replicas blend together to form broad peaks. Therefore, we will use the low temperature spectrum first to determine the number of defect levels and their transition energies.

The large peak near 1.61eV appears to be composed of two peaks and, adjacent to it a weaker peak. Because their energies are larger than the bandgap of CdTe  $E_g \approx 1.61\text{eV}$ , we associate those with either (e-h), (h-D) or (e-A) transitions. In CdTe, the lowest ionization energy for a donor is around 14meV (Francou et al., 1985), and 60meV for an acceptor (Molva et al., 1984). Given the relatively high ionization energy of acceptors, we conclude that apart from (e-h) transitions, possibly a (h-D) transition with a shallow donor is present. The energy difference between the two transitions is about 4meV.

Excitonic transitions that are usually prominent in high quality CdTe samples, are conspicuously absent in this sample, attesting to its poor quality. A very faint  $A^0X$  peak with the reported literature value of 1.589eV, is present at the lowest temperatures (fig. 6.19) but is very weak and will not be analyzed in this work.

The next peak at  $E=1.57\text{eV}$  was observed before (Giles-Taylor et al., 1985). Bryant, Totterdale and Hagston (Bryant et al., 1971) associated this peak with

the transition of an electron in the conduction band to the ground state of of neutral double acceptor center, probably cadmium vacancy ( $V_{Cd}$ ). The 1.57eV peak appears to have phonon replicas which were included in our model, in line with eq.(6.5).

The broad region from 1.3eV-1.55eV cannot be modeled assuming neither one nor two distinct transitions. We have found that acceptable agreement between experimental data and fit can be achieved assuming three defect transition. This is in line with Hofmann *et al.* (Hofmann et al., 1992). All three of these are expected to have pronounced phonon replicas so again, eq. (6.5) will be used.

Due to the great number of free parameters, a large number of iterations was performed ( $\approx 10^6$ ) to improve the quality of the fit, and arrive at a global optimum. The free parameters were chosen through a non-linear optimization method (random direction line search) while the contributions of individual peaks were determined through linear regression (after each non-linear iteration step, as part of the cost function evaluation).

An optimization procedure was performed for each temperature (and for all peaks present at that temperature).

Figure 6.20 show the results of the optimization for  $T=9.4K$ . The model was able to reproduce the experimental data for most of this spectrum. Similar results were obtained for other temperatures. The slight discrepancy around 1.54eV, can be attributed to the fact that a gaussian broadening mechanism was assumed for all peaks while the actual broadening differs from a gaussian. This produces errors around the side of the peaks. A better broadening mechanism, using Voigt profiles (convolution of a gaussian with a lorentzian), yielded slightly better results for certain peaks, but its evaluation is time consuming,

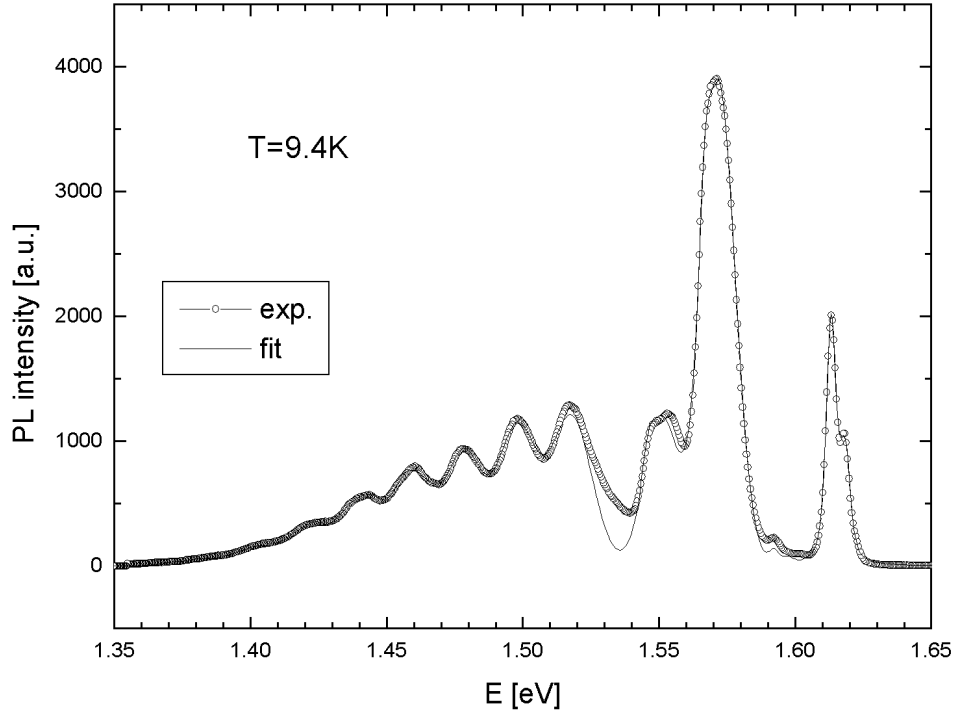


Figure 6.20: Optimization results for  $T=9.4\text{K}$ .

and more importantly, it introduces additional fitting parameters. The temperature dependence of the Huang-Rhys ( $S$ ) factor is given in figure 6.22, and is shown to be weak. The high numerical value of  $S$  for the last three peaks, indicates a significant amount of lattice distortion, hence these are complex defects. The first two peaks had no noticeable phonon replicas, meaning that no lattice distortion is present and these are simple defects. The third peak with  $S \approx 0.3$  has an intermediate behavior.

The temperature dependence of the peak intensities is given in figure 6.23. There is a sharp drop in peak intensities around 68K. Also, a less steeper decrease is observed at around 36K. We tentatively associate this with an increase in non-radiative recombination resulting from thermal activation of two unknown traps. Similar behavior was observed earlier (Krustok et al., 1996).

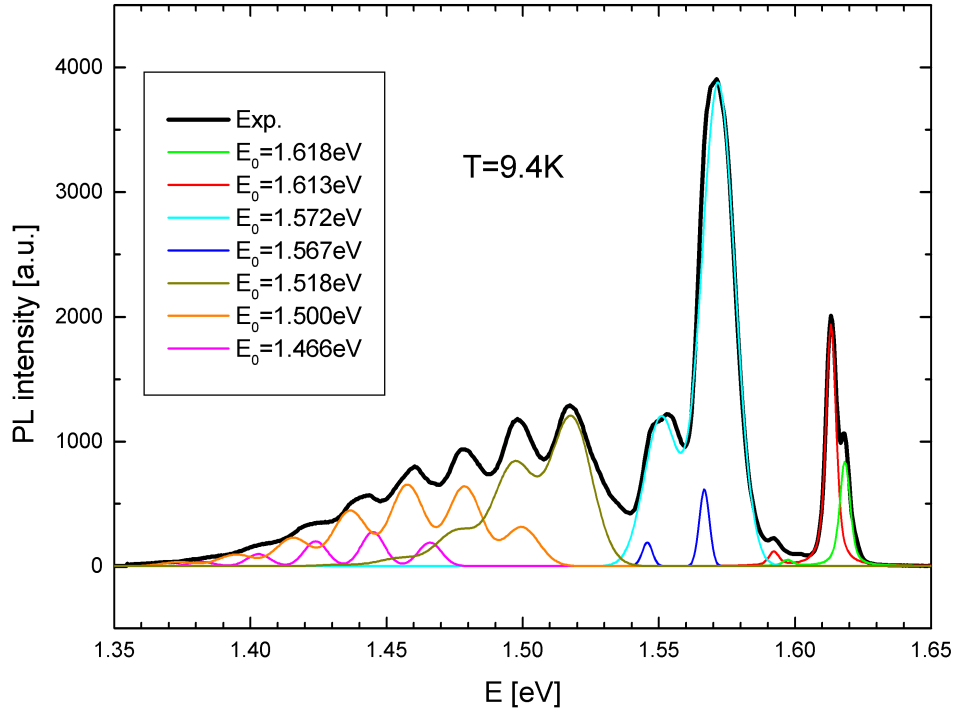


Figure 6.21: Peak composition at  $T=9.4\text{K}$ .

We also analyzed the spatial distribution of photoluminescence spectra in the CdTe sample. However, due to the limitations of the current experimental setup, spectra were only collected at 77K. At this temperature the phonon replicas blend together, and it becomes possible to fit the data with simple gaussians (for each transition). This also considerably increases the computation speed, which is an important consideration due to the massive amount of spectra in the image. Since imaging was being done, the laser beam was focused with a microscope objective, resulting in higher laser excitation power densities. This resulted in a sharp increase in the contribution of the (e-h) and (h-D) transition peaks. These two peaks appeared as doublets at lower temperatures but at 77K only a single peak is discernible so it was modeled with a single gaussian. Therefore, at 77K the optimization model consists of 5 gaussian-like transitions. Figure 6.24 shows

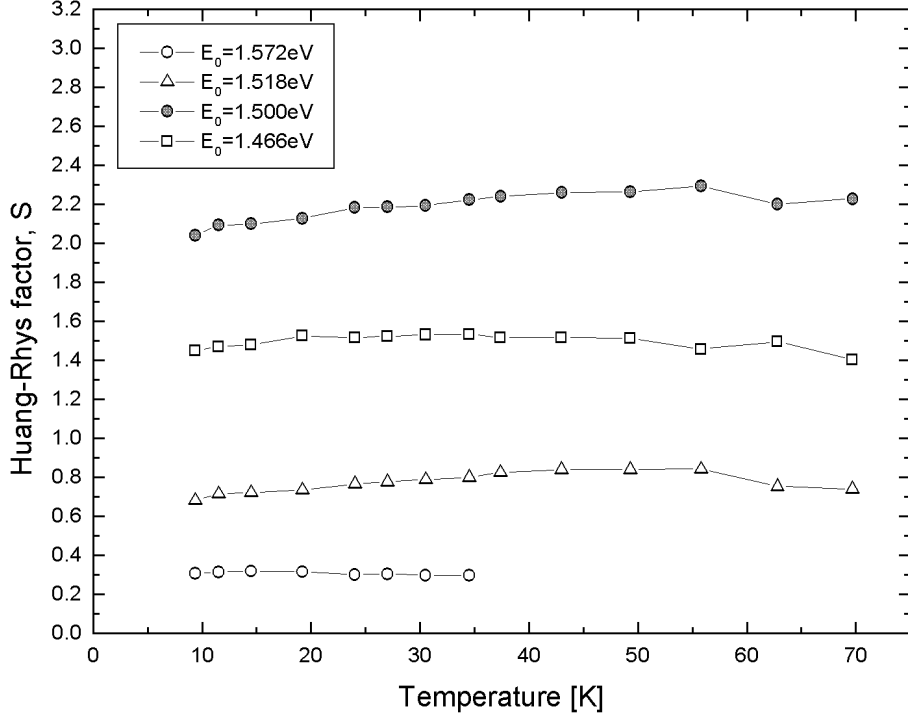


Figure 6.22: Temperature dependence of the Huang-Rhys factor ( $S$ ).

a representative spectrum along with the corresponding gaussian fit. Figures 6.25 through 6.29 show the spatial distribution of the relative contributions of the five peaks in the spectrum.

Interestingly, there is a relatively strong correlation (both positive and negative) between the images. To get the numerical strength of the correlation between various peaks, we calculated the correlation coefficients between two image matrices according to the following formula:

$$\text{cor}(X, Y) = \frac{\text{cov}(X, Y)}{\sigma_X \sigma_Y} = \frac{\langle (X - \mu_X)(Y - \mu_Y) \rangle}{\sigma_X \sigma_Y} \quad (6.7)$$

where  $X$  and  $Y$  are two vectors obtained by rearranging the  $N \times N$  image matrices into vectors of length  $N^2$ . The results are presented in table 6.30. It is clear that the peaks can be divided into two groups. The first group contains peaks at 1.60eV, 1.57eV and 1.46eV. While the second group contains peaks at

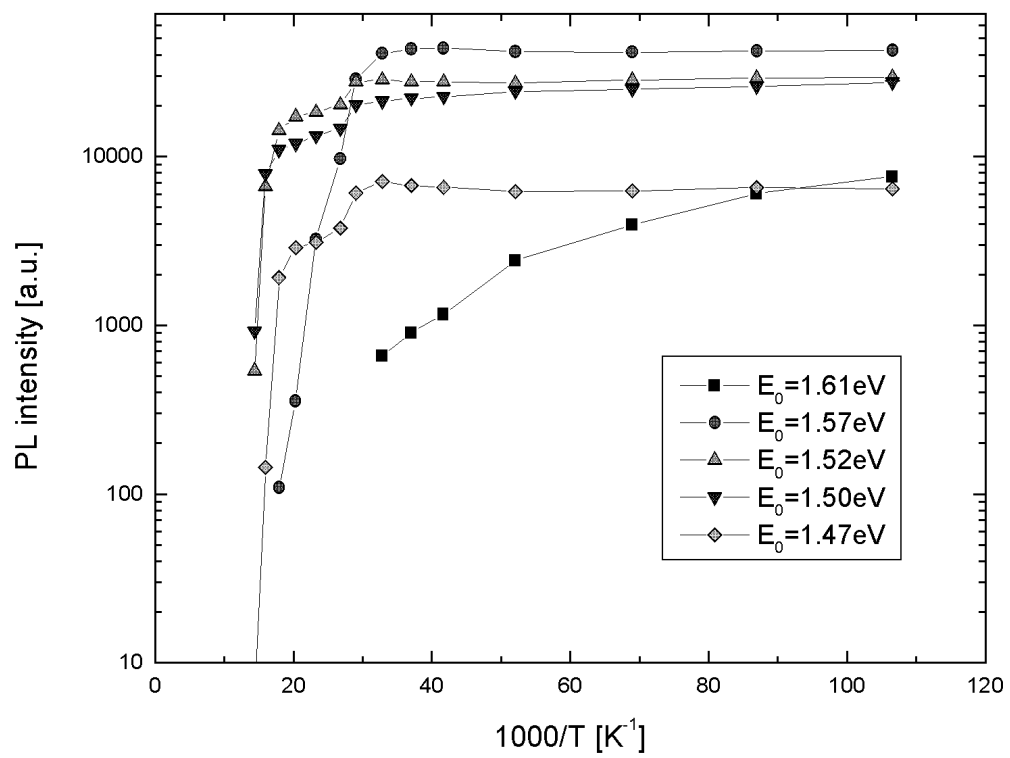


Figure 6.23: Temperature dependence of peak intensities.

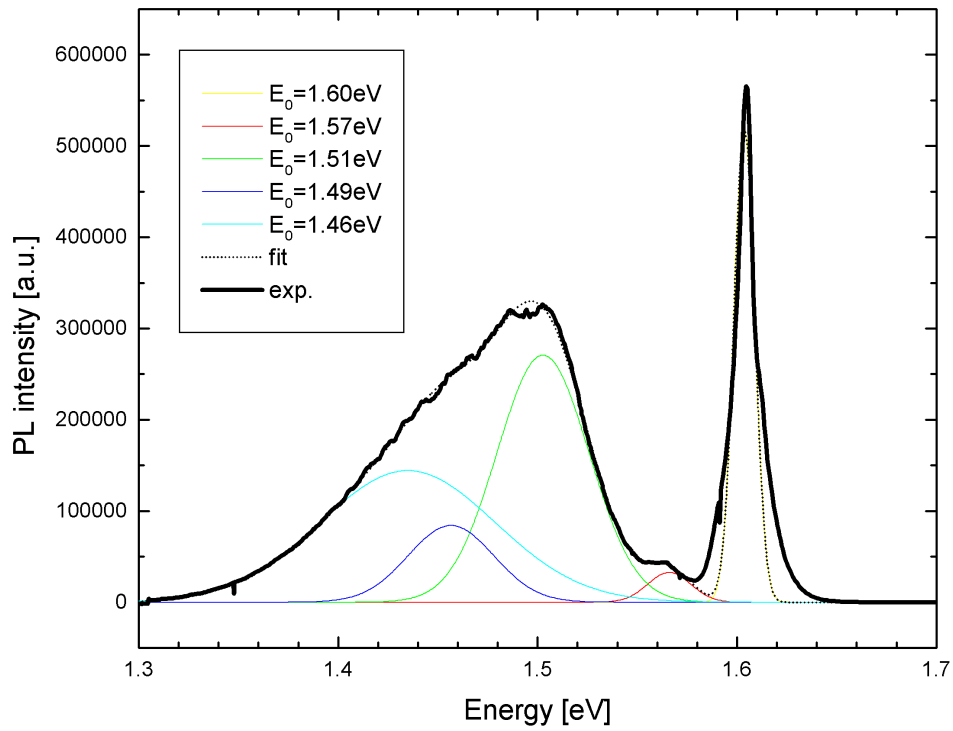


Figure 6.24: Gaussian fit of PL peaks at 77K.

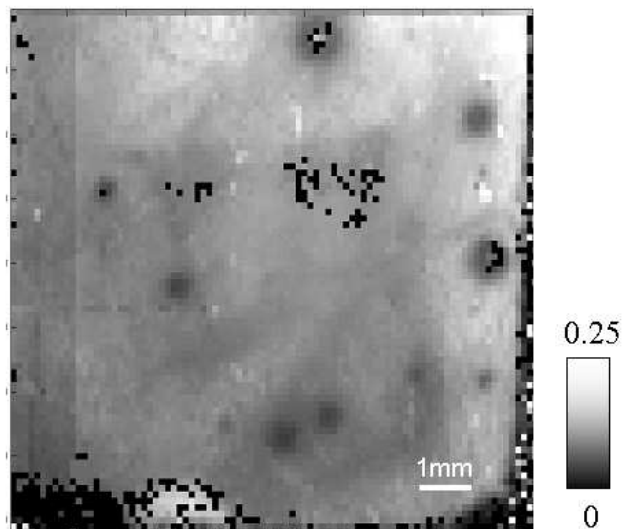


Figure 6.25: Relative contribution of the E=1.60eV transition.

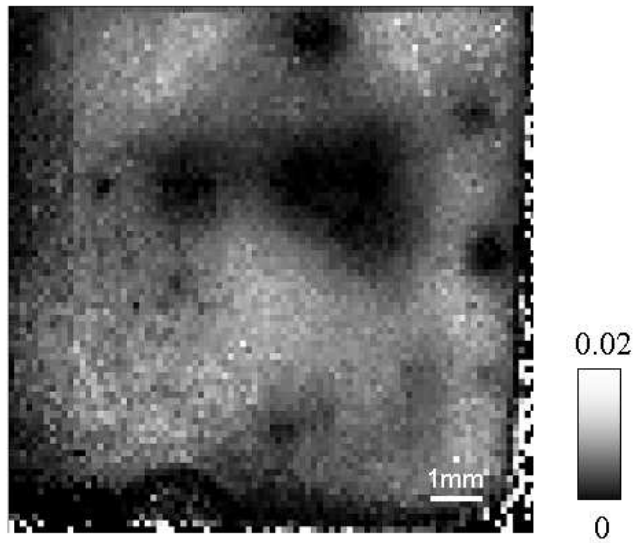


Figure 6.26: Relative contribution of the  $E=1.57\text{eV}$  transition.

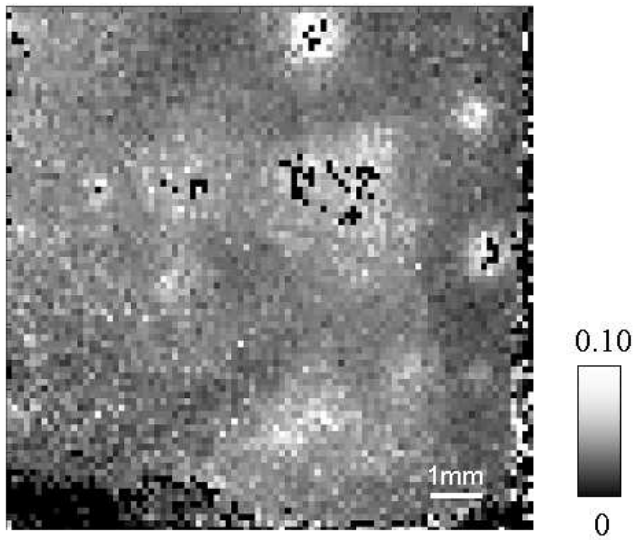


Figure 6.27: Relative contribution of the  $E=1.51\text{eV}$  transition.

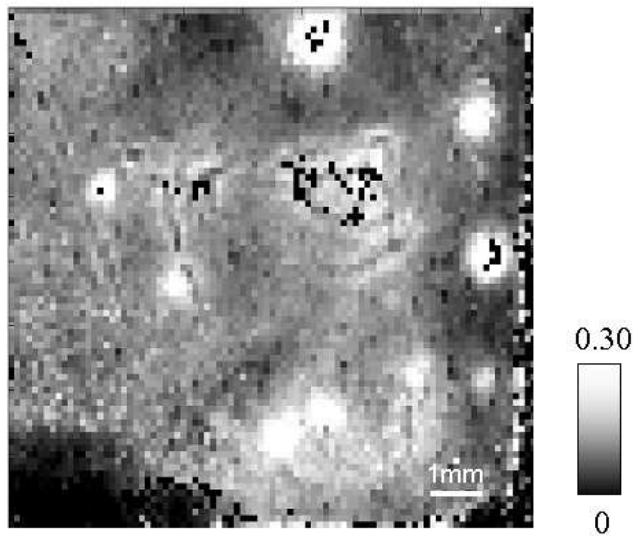


Figure 6.28: Relative contribution of the  $E=1.49\text{eV}$  transition.

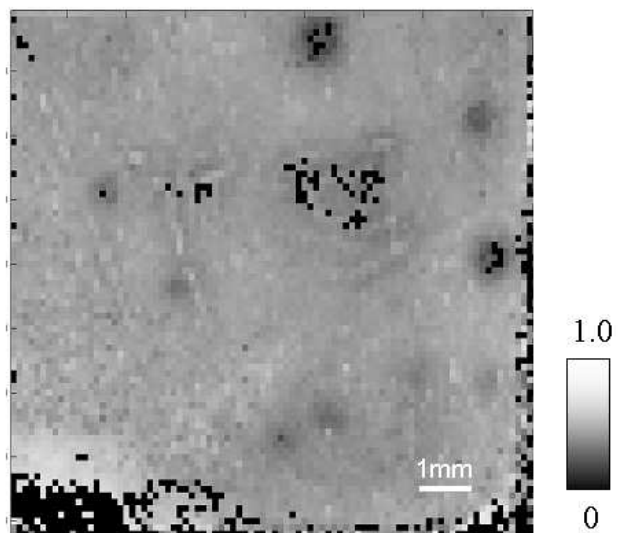


Figure 6.29: Relative contribution of the  $E=1.46\text{eV}$  transition.

cor	1.60eV	1.57eV	1.51eV	1.49eV	1.46eV
1.60eV	1.000	0.407	0.043	-0.108	0.477
1.57eV		1.000	-0.144	0.137	0.381
1.51eV			1.000	0.741	0.121
1.49eV				1.000	-0.077
1.46eV					1.000

Figure 6.30: Spatial correlation between defect level transitions.

1.51eV and 1.49eV. Peaks in one group anti-correlate with the peaks from the other group. A possible explanation for this is that one group is related to a common impurity or complex defect, while the other group is not. The increase in the presence of this impurity or defect will make transitions for this group more likely, thus increasing their contribution, at the expense of the transitions from the other group. CdTe samples with surface damage contain a high concentration of cadmium vacancies ( $V_{Cd}$ ). The large spatial inhomogeneity of the defect transitions strongly suggests that these are likely to be related to  $V_{Cd}$ , most likely due to a defect complex with a donor ( $D_{Cd} - V_{Cd}$ ).

## 6.7 Photoluminescence imaging of $\text{Hg}_{1-x}\text{Cd}_x\text{Te}$

Due to the high sensitivity of the experimental setup, photoluminescence imaging of mid-IR  $\text{Hg}_{1-x}\text{Cd}_x\text{Te}$  can be performed even at room temperature. However, imaging at lower temperatures (77K) is preferred because of higher signal-to-noise ratio (SNR) of spectra resulting from increased PL signals. Figure 6.31 shows the same region of an  $\text{Hg}_{1-x}\text{Cd}_x\text{Te}$  ( $x=0.3$ ) sample imaged at 77K and 300K. The increase in SNR helps distinguish between noise and actual features.

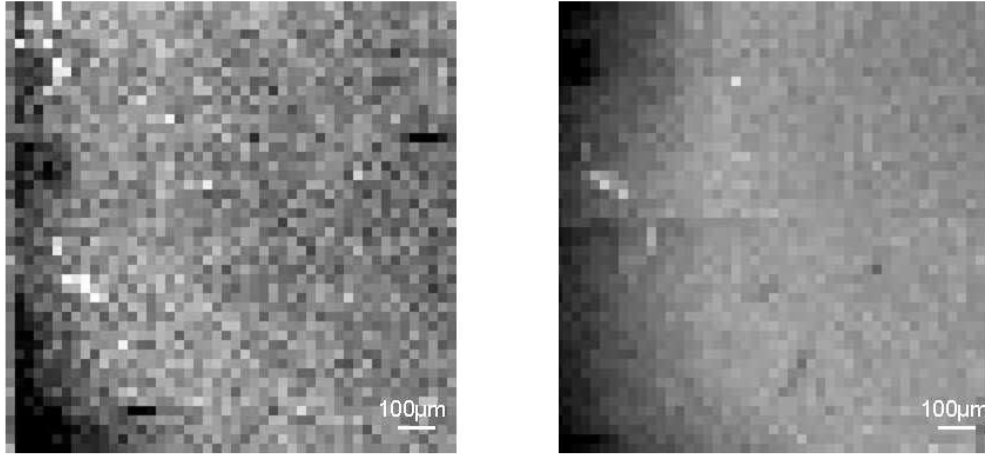


Figure 6.31: The influence of temperature on the signal-to-noise ratio of PL images. Identical  $1.2\text{mm} \times 1.2\text{mm}$  ( $48 \times 48$  pixels) regions of a  $\text{Hg}_{1-x}\text{Cd}_x\text{Te}$  ( $x=0.3$ ) sample were imaged at 300K (left) and 77K (right). At 300K the acquisition time was 19s/pixel (total scan time 12.5hr), while at 77K it was 8.4s/pixel (total scan time 5.5hr).

Figure 6.32 illustrates the effects of annealing on the FWHM of the PL peak. As expected, a decrease in the FWHM is observed for the annealed sample. The imaging of macroscopic defects is shown in Fig. 6.33. It illustrates the fact that photoluminescence is very sensitive to defects present at or near the surface of the material.

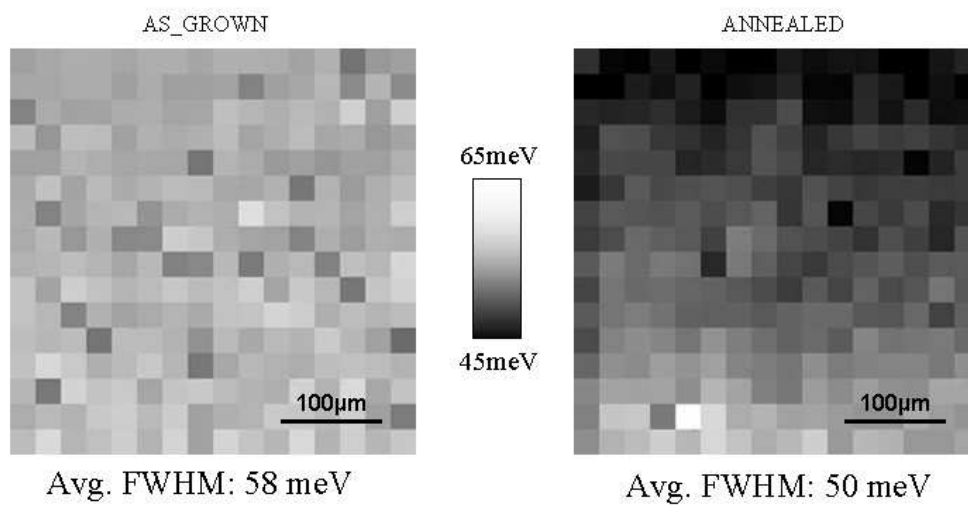


Figure 6.32: The influence of sample annealing on the band edge photoluminescence peak. Spatial distribution of the peak FWHM was imaged for a  $400 \times 400 \mu\text{m}^2$  region of a  $\text{Hg}_{1-x}\text{Cd}_x\text{Te}$  ( $x=0.3$ ) sample.

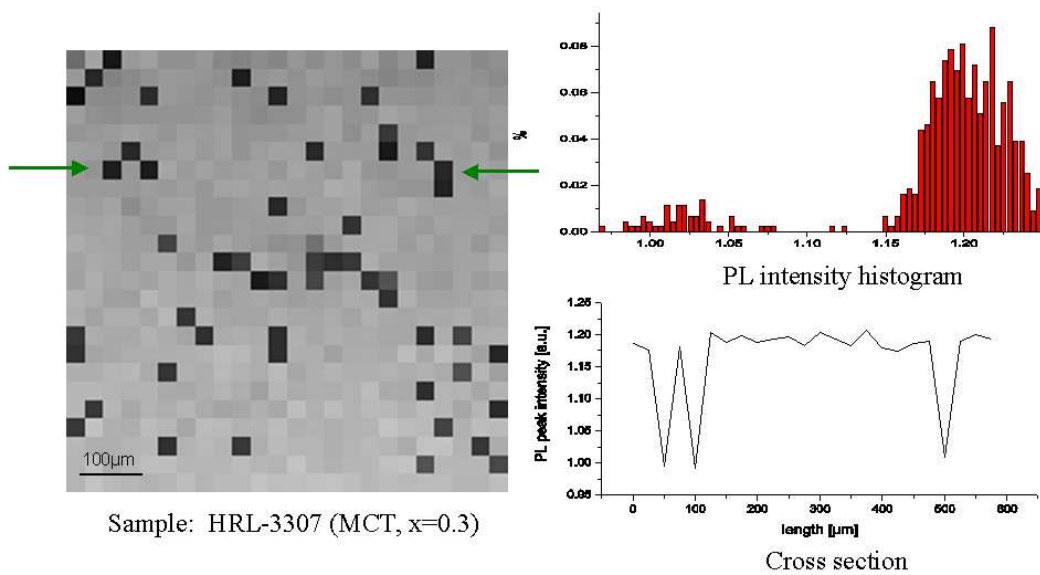


Figure 6.33: Photoluminescence imaging of macroscopic defects at or near the surface of an  $\text{Hg}_{1-x}\text{Cd}_x\text{Te}$  ( $x=0.3$ ) sample. At the site of defects, an  $\approx 20\%$  reduction in PL intensity is observed. Apart from the defected regions, the sample is fairly uniform, as is seen in the PL intensity histogram and the cross section (along the line indicated by arrows in the image).

# Chapter 7

## Low Temperature

## Photoluminescence Study

## of $\text{Hg}_{1-x}\text{Cd}_x\text{Te}$

### 7.1 Influence of doping and alloy composition

The temperature dependence of photoluminescence spectra of four  $\text{Hg}_{1-x}\text{Cd}_x\text{Te}$  epilayers was studied. The samples were  $\approx 5\mu\text{m}$  thick MBE grown epilayers on (211)B bulk  $\text{Cd}_{0.96}\text{Zn}_{0.04}\text{Te}$  substrates. The alloy composition ranged from  $x = 0.280$  to  $x = 0.574$ . The  $x = 1$  composition point (i.e. CdTe) was already studied in chapter 6. The  $x = 0.458$  and  $x = 0.574$  samples were highly doped with In ( $\sim 10^{18}\text{cm}^{-3}$ ). The rest of the samples were only lightly doped ( $\sim 10^{15}\text{cm}^{-3}$ ). All samples were *n*-type materials.

Figure 7.1 shows the PL spectra at  $\approx 10\text{K}$ . All spectra except the one with  $x = 0.458$  consist of a single broad peak of varying widths. The  $x = 0.458$  sample clearly contains two peaks, similar to CdTe spectra described in chapter

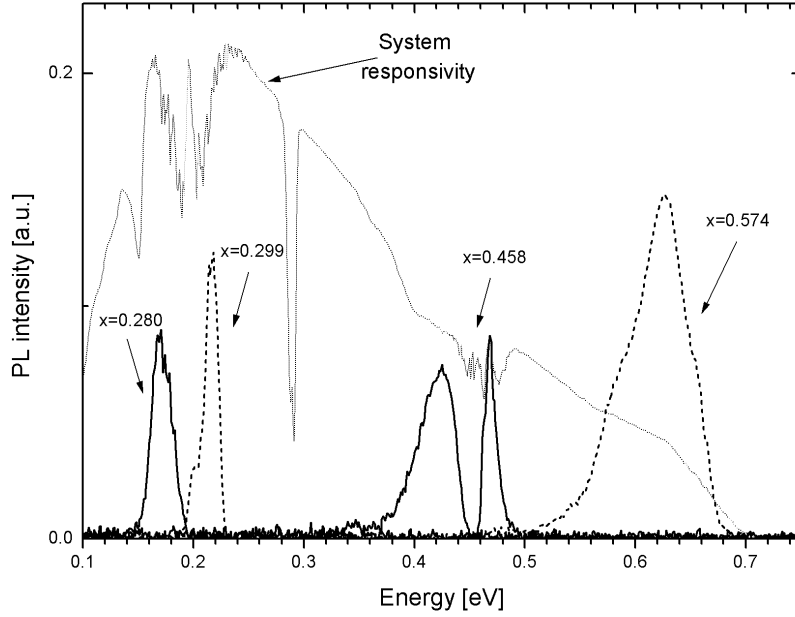


Figure 7.1: Photoluminescence spectra at 10K for four  $\text{Hg}_{1-x}\text{Cd}_x\text{Te}$  epilayers with varying alloy composition.

6. The relative smoothness and continuity of the FTIR system responsivity in the energy range of these peaks (see Figure 7.1) shows that the peak structure is not a result of spectral artifacts. Although spectral artifacts are present (as small undulations in the spectra, as discussed in detail in chapter 8), they cannot account for the two isolated peaks. Therefore, we conclude that the low energy peak in the  $x = 0.458$  spectrum is a defect level, possibly resulting from the high doping level of the samples. Since the  $x = 0.574$  has the similar doping concentration, it is likely that the wide peak is actually a superposition of two (or possibly more) peaks, one being related to high indium doping

Kraus *et al.* (Kraus et al., 1993) studied as-grown n-type  $\text{Hg}_{1-x}\text{Cd}_x\text{Te}$  ( $0.3 \leq x \leq 0.68$ ) samples, and observed spectra dominated by single emission lines with increasing linewidths for higher  $x$  values. They argued that alloy broadening might account for the observed increase in the linewidth at high

x-values. Schubert *et al.* (Schubert et al., 1984) developed a theory for alloy broadening in ternary alloys, and gave numerical data for  $\text{Al}_x\text{Ga}_{1-x}\text{As}$ . The linewidth broadening is given by

$$\sigma_E = \frac{dE_g}{dx} \sqrt{\frac{a_0^3 x(1-x)}{4V}} \quad (7.1)$$

where  $a_0$  is the lattice constant and  $V$  the effective volume of the sample in which the transition occurs. For  $\text{Al}_x\text{Ga}_{1-x}\text{As}$ , the maximum broadening (for  $e-A^0$  transitions) was  $\approx 20\text{meV}$ . For  $\text{Hg}_{1-x}\text{Cd}_x\text{Te}$ , due to low electron effective masses, the effective volumes tend to be larger than for  $\text{Al}_x\text{Ga}_{1-x}\text{As}$ . Therefore, the alloy broadening alone does not explain completely the increase in linewidth. It is likely that at higher x-values, defect level transitions are more readily observed. This is in line with theoretical calculations of some of the possible defect states in  $\text{Hg}_{1-x}\text{Cd}_x\text{Te}$ . For example, figure 7.2, shows the energy levels of some cation vacancies as well as cation-site substitutional impurity states (Kobayashi et al., 1982). According to the calculation, donor states are present inside the gap for  $x \gtrsim 0.5$ , while vacancy related acceptor states for  $x \gtrsim 0.7$ . However, due to the inherent inaccuracies of theoretical calculations these numerical values are just estimates, the general trend of not having gap states for low x-values being the most important conclusion in (Kobayashi et al., 1982). Defect complexes were not included in the above calculation.

In order to determine if the defect level for the  $x = 0.458$  sample is a shallow impurity or a complex defect, we measured PL spectra by excitation at two different laser powers. Table 7.1 gives the center-of-mass positions for the two peaks. A small change is observed in the first peak. This can be a sign of a complex defect, such as  $In_{Cd}-V_{Cd}$  observed in  $x = 1$  (CdTe) samples. Because of the decrease of peak center with increased laser power, we can exclude a donor-

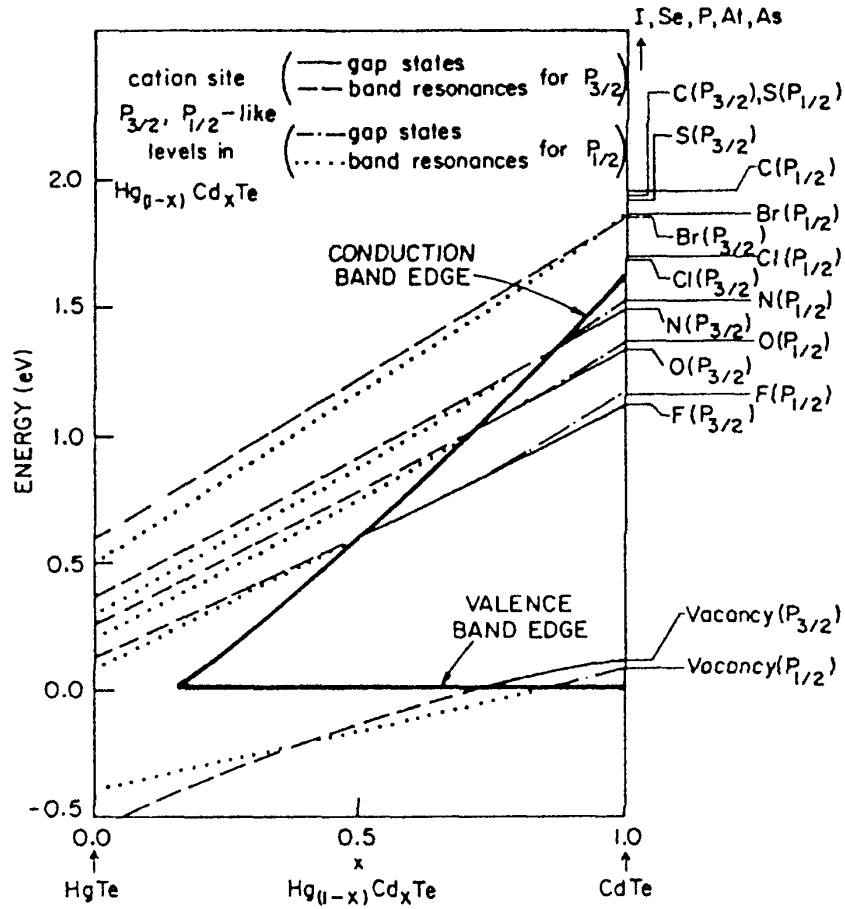


Figure 7.2: Calculated energy levels of cation vacancy and cation site substitutional impurities as a function of alloy composition in  $\text{Hg}_{1-x}\text{Cd}_x\text{Te}$  (Kobayashi et al., 1982).

Laser power [ $\text{kW}/\text{cm}^2$ ]	$E_{t,1}$ [eV]	$E_{t,2}$ [eV]
0.15	0.4183(5)	0.4706(5)
1.50	0.4146(5)	0.4703(5)

Table 7.1: Peak positions as a function of excitation laser power.

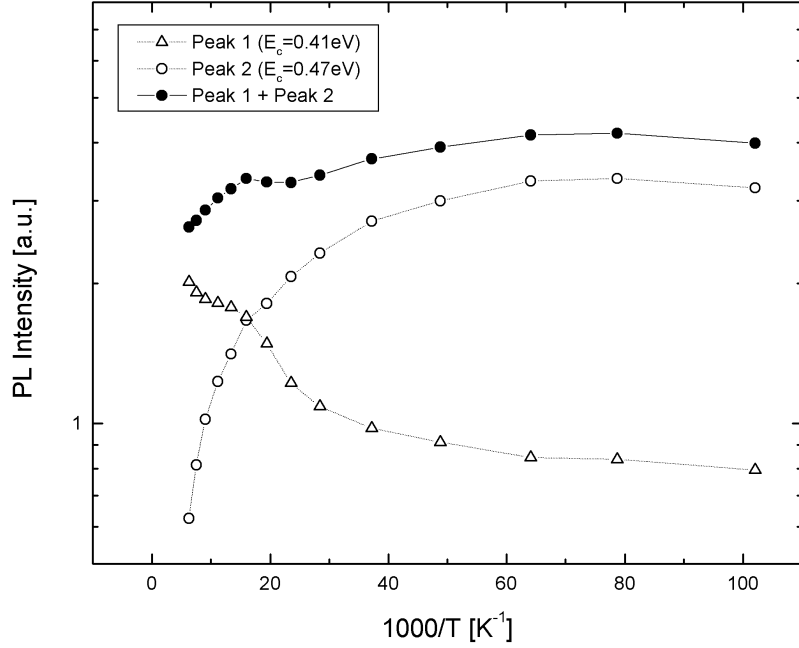


Figure 7.3: The intensity of the two peaks in the PL spectrum of the  $\text{Hg}_{1-x}\text{Cd}_x\text{Te}$  ( $x=0.458$ ) sample as a function of temperature.

acceptor pair (DAP) because they exhibit the opposite trend. Also, the width of the peak extends several phonon energies ( $E_{\text{phonon}} \approx 20\text{meV}$ ), characteristic of such complex defects. Nonetheless, this is inconclusive as it is also possible that two or more defect levels, broadened by alloy disorder are responsible for the wide peak. The temperature dependence of the two peaks is shown in Fig. 7.3. Although the strength of both peaks decreases with the increase in temperature, the proportion of radiative recombination into the first peak is increased. This behavior is similar to that of deep defect centers in CdTe (Chapter 6).

## 7.2 Influence of annealing

The temperature dependence of an as-grown and Hg-annealed mid-IR  $\text{Hg}_{1-x}\text{Cd}_x\text{Te}$  ( $x=0.3$ ) sample was measured. Figure 7.4 shows the PL spectra of the as-grown

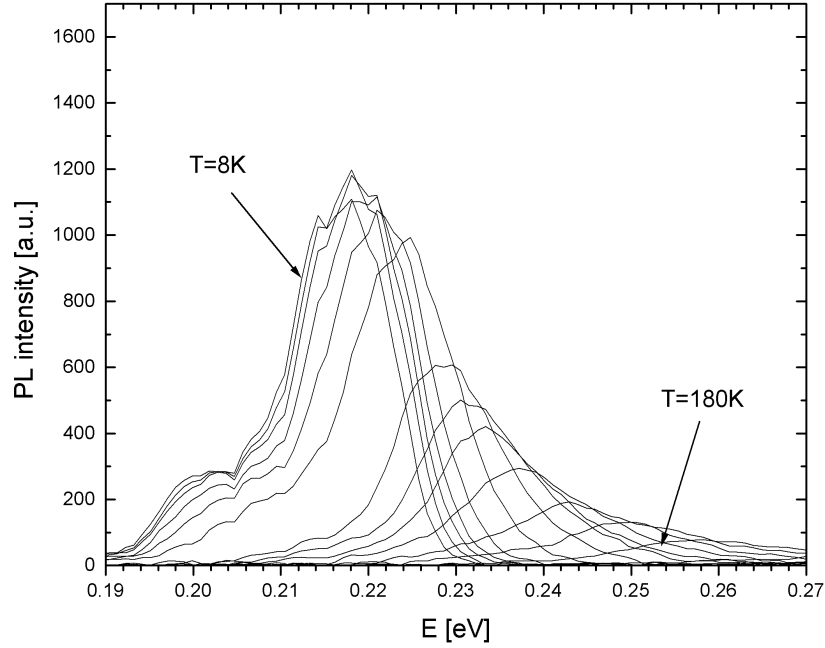


Figure 7.4: Photoluminescence spectra of as-grown  $\text{Hg}_{1-x}\text{Cd}_x\text{Te}$  ( $x = 0.3$ ) for a series of temperatures from  $T=8\text{K}$  to  $T=180\text{K}$ .

sample for a series of temperatures. Figure 7.5 shows the similar spectra for the annealed sample. The annealed sample had a narrower peak, which can be attributed to the decrease in the concentration of native defects in the annealing process. The PL spectra appear to contain two peaks, however, this can be misleading. The dip in the spectrum coincide with a water absorption band, and also the interference effects from the thin film are modulating the spectra below the bandgap. The necessary corrections would require accurate values of the index of refraction and absorption, which can be obtained using infrared spectroscopic ellipsometry. It is more likely that the spectrum is just a single emission line, due to (e-h) recombination with significant portion coming from recombination of carriers in the band tails, as most of the PL peak is located below the bandgap. This was suggested earlier in the literature

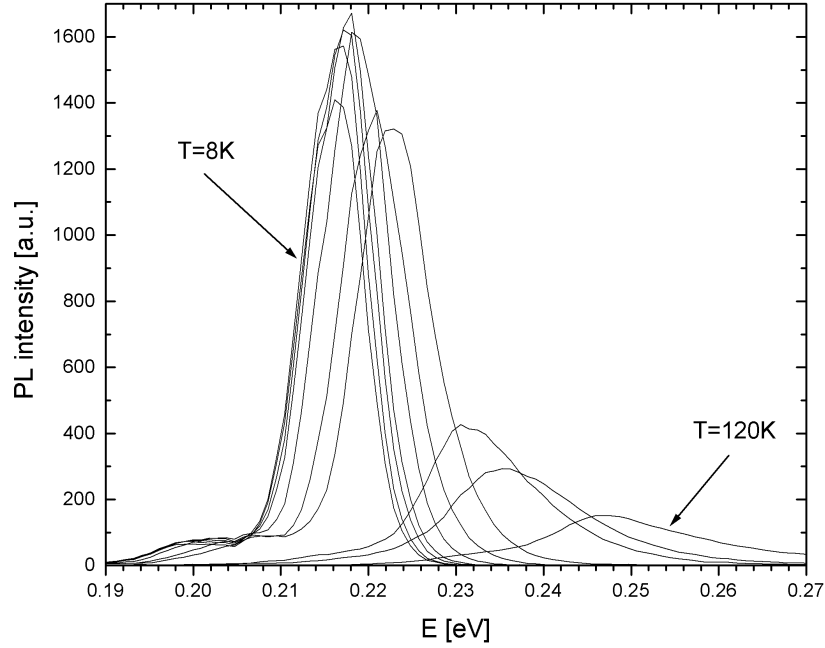


Figure 7.5: Photoluminescence spectra of Hg-annealed  $\text{Hg}_{1-x}\text{Cd}_x\text{Te}$  ( $x = 0.3$ ) for a series of temperatures from  $T=8\text{K}$  to  $T=180\text{K}$ .

(Kraus et al., 1993, Chang et al., 2000). There is some evidence, however, that Hg-related defect complexes (such as  $In_{Cd} - V_{Hg}$ ) can be associated with the increase in PL linewidth (Kurtz et al., 1993).

The temperature dependence of the PL peak intensity is given in Fig. 7.6. It appears that both samples have a similar temperature dependence. A single thermally activated non-radiative recombination center is responsible for rapid PL quenching at higher temperatures.

### 7.3 Influence of substrate quality

The preparation and overall quality of substrates have long been known to influence the quality of epilayers. In order to evaluate photoluminescence as a viable characterization tool for gauging substrate quality, we measured the

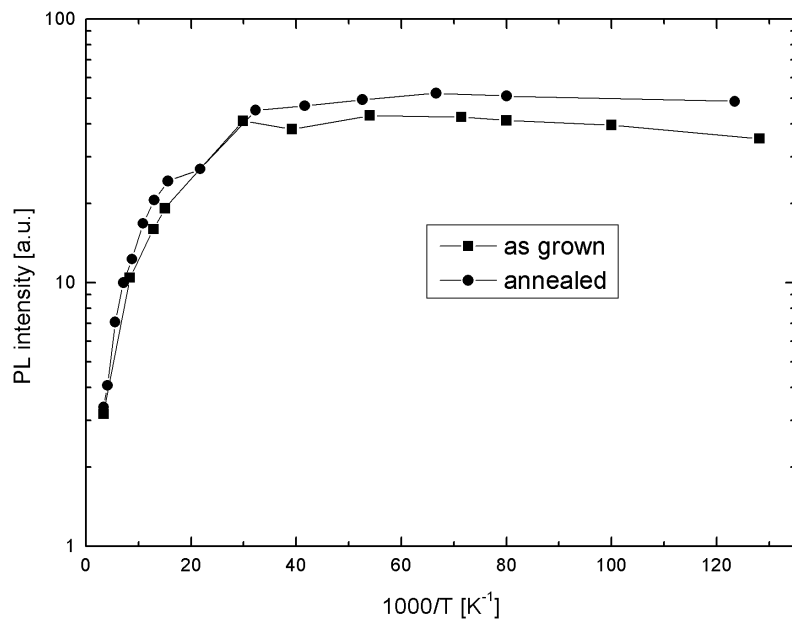


Figure 7.6: Temperature dependence of the photoluminescence intensity for  $\text{Hg}_{1-x}\text{Cd}_x\text{Te}$  ( $x=0.3$ ). Spectra for both as grown and annealed samples are given.

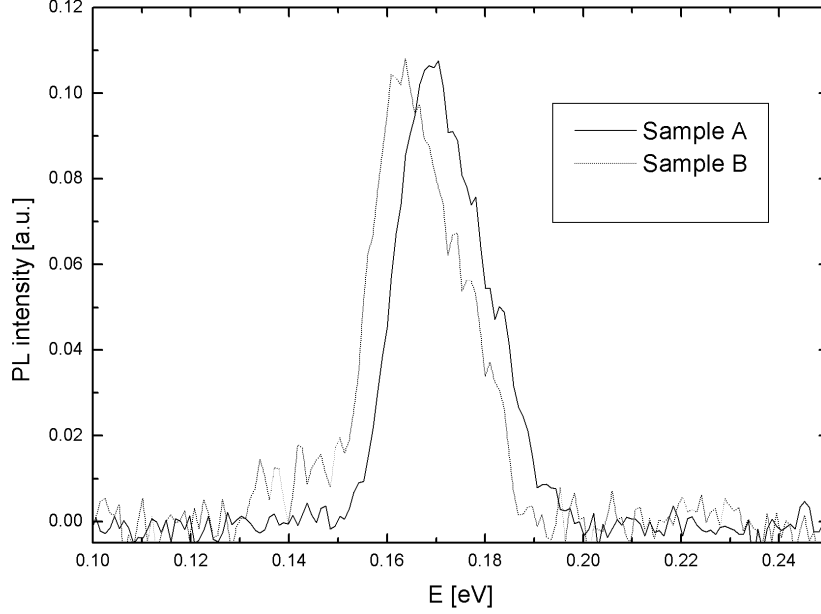


Figure 7.7: Photoluminescence spectra for two  $\text{Hg}_{1-x}\text{Cd}_x\text{Te}$  ( $x=0.280$ ) epilayers grown on  $\text{Cd}_{0.96}\text{Zn}_{0.04}\text{Te}$  substrates of differing quality. Sample B is grown on inferior substrate.

temperature dependence of photoluminescence for two similar samples grown on substrates of differing quality. Sample A is an  $\text{Hg}_{1-x}\text{Cd}_x\text{Te}$  ( $x = 0.280$ ) epilayer grown on state-of-the-art bulk  $\text{Cd}_{0.96}\text{Zn}_{0.04}\text{Te}$  substrates (by Nikko Materials, Japan). Sample B was grown under identical growth conditions and similar substrate as sample A, with the only exception that the substrate was repolished using an inferior polishing technique. Sample A had an etch pit density of  $EPD \approx 10^5 \text{cm}^{-2}$  while sample B had  $EPD \approx 10^6 - 10^7 \text{cm}^{-2}$ . Figure 7.7 shows the photoluminescence spectra for the two samples at  $T=11\text{K}$ . There is a spectral shift between the two spectra. It corresponds to a composition fluctuation of  $\Delta x = 0.003$ . This is in line with the  $\Delta x = 0.003$  run-to-run reproducibility of alloy composition achieved in MBE growth of  $\text{Hg}_{1-x}\text{Cd}_x\text{Te}$  epilayers of this type (Bajaj et al., 1996). Therefore, the observed shift is insignificant.

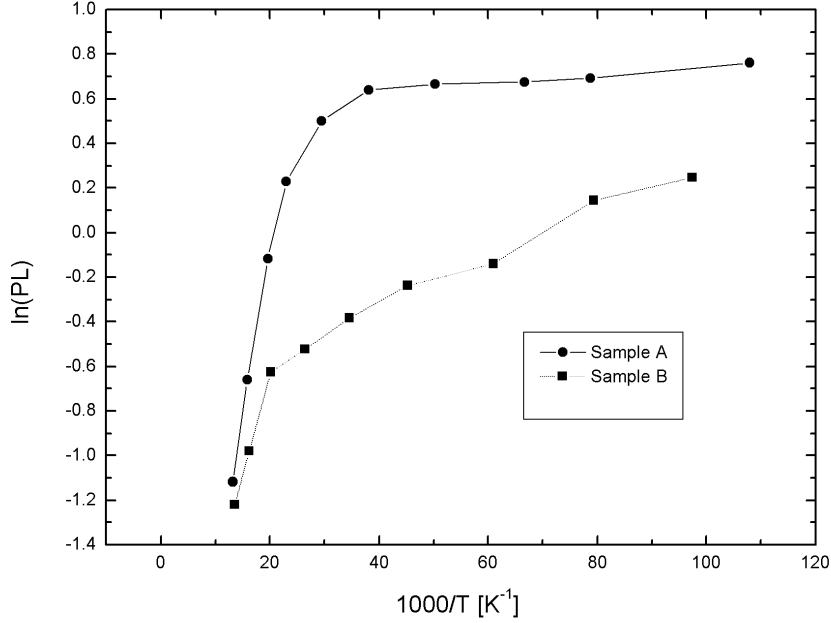


Figure 7.8: Temperature dependence of the photoluminescence intensity for two  $\text{Hg}_{1-x}\text{Cd}_x\text{Te}$  ( $x=0.280$ ) epilayers grown on  $\text{Cd}_{0.96}\text{Zn}_{0.04}\text{Te}$  substrates of differing quality. Sample B is grown on inferior substrate.

Next to the low energy side of the sample B PL peak, a small but noticeable peak can be observed. This might be attributed to a possible transition associated with the defects in the epilayer as a result of growing on low-quality substrates.

The temperature dependence of the PL peak intensity is given in Fig. 7.8. There is a large difference in PL intensity. Also, the samples seem to have different non-radiative recombination mechanisms. The high density of threading dislocations originating at the low-quality surface of the substrate act as an additional source of non-radiative traps, along with the ones due to native defects resulting in MBE growth of  $\text{Hg}_{1-x}\text{Cd}_x\text{Te}$ .

## Chapter 8

# The Effect of Multilayers on Luminescence Spectra

As we saw in the previous chapter, the PL spectra of  $\text{Hg}_{1-x}\text{Cd}_x\text{Te}$  appear to contain weak shoulders that might indicate multiple peaks in the band edge PL. In this chapter we show that this is a spectral artifact caused by the interference fringes in the  $\text{Hg}_{1-x}\text{Cd}_x\text{Te}$  film.

### 8.1 Introduction

In most experiments where luminescence (photo-, cathodo-, electro- etc.) of materials is measured, little or no consideration is given to the distortion of these spectra as a function of depth at which the luminescence is generated and its subsequent propagation through the sample. In some cases, the distortion is minimal and does not warrant special lineshape correction. However, for many types of samples and collection geometries the distortion of luminescence lineshape can be a significant source of systematic errors.

For example, in the near bandgap region of semiconductors the self-absorption of luminescence can change the shape of the spectra as a function of depth at which it was generated (Garbuzov, 1986). It can be shown that the luminescence decay curve is influenced through self-absorption related effects in direct band-gap materials. Ignoring this can lead to the underestimation of the luminescence lifetime (Bensaid 1989, Luke and Cheng, 1987, Hooft and van Opdorp, 1986, Boulou and Bois, 1977).

The sample geometry can also influence the shape of luminescence spectra (Shahzad and Cammack, 1990, Lester et al., 1988, Warwick, 1986, Yang et al., 1997).

Thin film interference effects should be taken into account if the spectral range of features is comparable or larger than the interference fringe spacings. Otherwise, the modulations of the luminescence spectra due to these fringes can be misinterpreted as actual defect level transitions.

In this chapter we give a detailed analysis of the propagation of luminescence through arbitrary multilayered structures using the Fresnel matrix method.

## 8.2 Theory

We treat the sample as a multilayer structure consisting of  $N$  infinite layers and  $N + 1$  interfaces (see Fig.8.1). Let the thickness of a given layer be  $d_j$  and the index of refraction  $\mathbf{n}_j = n_j - k_j i$ , where  $j = 1, 2, \dots, N$ .  $\mathbf{n}_0$  and  $\mathbf{n}_{N+1}$  are the indices of refraction of the region above and below the sample, respectively. In most cases the sample is in air so  $\mathbf{n}_0 = \mathbf{n}_{N+1} = 1$ . The electric fields of the approaching and reflected waves at the interface  $j$  will be denoted  $E_j^+$  and  $E_j^-$ , respectively. For non-normal incidence an additional index for the polarization

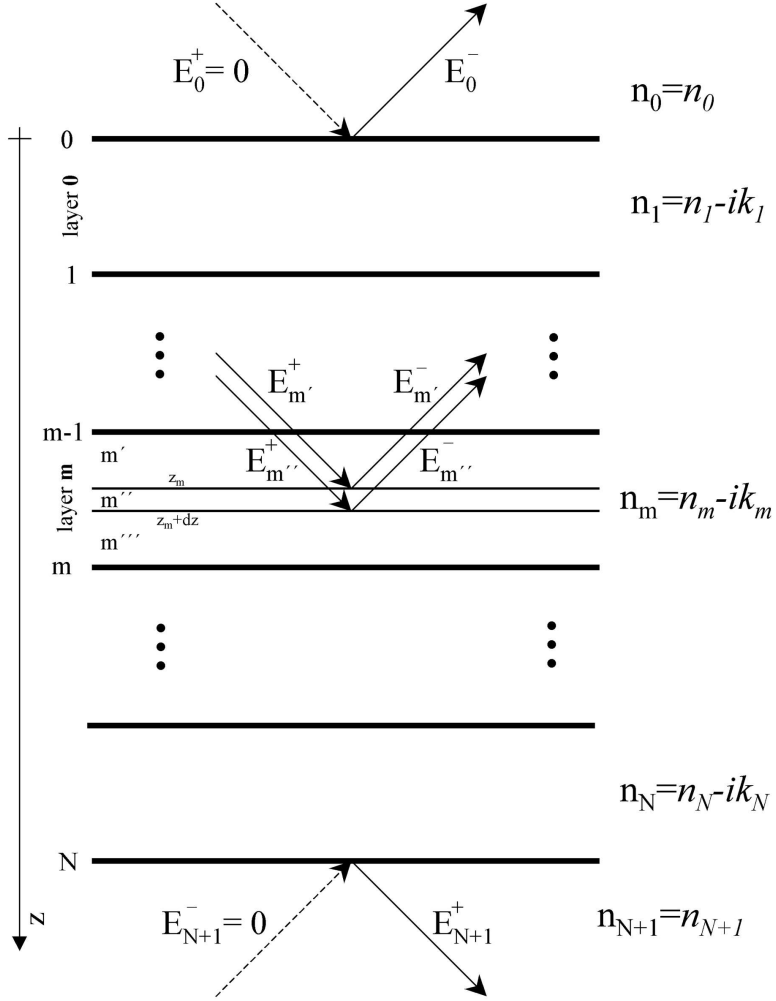


Figure 8.1: The multilayer structure used in the analysis.

( $p$  or  $s$ ) will be omitted, but is always implied. A coordinate system originating at the top of the sample, and with its  $z$ -axis pointing into the sample will be used.

It can be shown (Heavens, 1991) that the the electric fields at two consecutive interfaces are related by the following matrix equation:

$$\begin{aligned}
 \begin{pmatrix} E_{j-1}^+ \\ E_{j-1}^- \end{pmatrix} &= \frac{1}{t_j} \begin{pmatrix} e^{i\delta_{j-1}} & r_j e^{i\delta_{j-1}} \\ r_j e^{-i\delta_{j-1}} & e^{-i\delta_{j-1}} \end{pmatrix} \begin{pmatrix} E_j^+ \\ E_j^- \end{pmatrix} \\
 &= C_j \begin{pmatrix} E_j^+ \\ E_j^- \end{pmatrix}
 \end{aligned} \tag{8.1}$$

where:

$$r_j = \begin{cases} \frac{\mathbf{n}_{j-1} \cos \theta_j - \mathbf{n}_j \cos \theta_{j-1}}{\mathbf{n}_{j-1} \cos \theta_j + \mathbf{n}_j \cos \theta_{j-1}} & p \text{ polarization} \\ \frac{\mathbf{n}_{j-1} \cos \theta_j - \mathbf{n}_j \cos \theta_j}{\mathbf{n}_{j-1} \cos \theta_j + \mathbf{n}_j \cos \theta_j} & s \text{ polarization} \end{cases} \quad (8.2)$$

$$t_j = \begin{cases} \frac{2\mathbf{n}_{j-1} \cos \theta_{j-1}}{\mathbf{n}_{j-1} \cos \theta_j + \mathbf{n}_j \cos \theta_{j-1}} & p \text{ polarization} \\ \frac{2\mathbf{n}_{j-1} \cos \theta_{j-1}}{\mathbf{n}_{j-1} \cos \theta_{j-1} + \mathbf{n}_j \cos \theta_j} & s \text{ polarization} \end{cases} \quad (8.3)$$

$$\delta_j = \begin{cases} 0 & j = 0 \\ \frac{2\pi}{\lambda} \mathbf{n}_j d_j \cos \theta_j & j = 1, 2, \dots, N \end{cases} \quad (8.4)$$

$$\mathbf{n}_j \sin \theta_j = \mathbf{n}_{j-1} \sin \theta_{j-1} \quad (8.5)$$

Applying equation (8.1) recursively, the electric field between any two interfaces in the sample can be found provided that the electromagnetic field is continuous across layers - a major assumption made in deriving equation (8.1). Luminescence, however, represents a discontinuity in form of an electromagnetic source. Therefore, the region above and below the position where it is generated has to be dealt with separately.

Let us assume that the luminescence was generated in the  $m$ th layer, in the region between  $z_m$  and  $z_m + dz$  (as measured from the  $(m - 1)$ th interface as indicated in Fig. 1). This way, the  $m$ th layer is effectively broken into three separate layers:  $m'$ ,  $m''$  and  $m'''$ . The following equations relate the electric field amplitudes for the region above  $z_m$  and below  $z_m + dz$ :

$$\begin{aligned} \begin{pmatrix} 0 \\ E_0^- \end{pmatrix} &= C^- \begin{pmatrix} e^{i\frac{2\pi}{\lambda} \mathbf{n}_m z_m \cos \theta_m} & 0 \\ 0 & e^{-i\frac{2\pi}{\lambda} \mathbf{n}_m z_m \cos \theta_m} \end{pmatrix} \begin{pmatrix} E_{m'}^+ \\ E_{m'}^- \end{pmatrix} \\ &= D^- \begin{pmatrix} E_{m'}^+ \\ E_{m'}^- \end{pmatrix} \end{aligned} \quad (8.6)$$

$$\begin{aligned}
\begin{pmatrix} E_{m''}^+ \\ E_{m''}^- \end{pmatrix} &= \frac{1}{t_{m+1}} \begin{pmatrix} e^{i\frac{2\pi}{\lambda}(d_m-z_m)\cos\theta_m} & r_{m+1}e^{i\frac{2\pi}{\lambda}(d_m-z_m)\cos\theta_m} \\ r_{m+1}e^{-i\frac{2\pi}{\lambda}(d_m-z_m)\cos\theta_m} & e^{-i\frac{2\pi}{\lambda}(d_m-z_m)\cos\theta_m} \end{pmatrix} C^+ \begin{pmatrix} E_{N+1}^+ \\ 0 \end{pmatrix} \\
&= D^+ \begin{pmatrix} E_{N+1}^+ \\ 0 \end{pmatrix}
\end{aligned} \tag{8.7}$$

where

$$C^- = C_1 C_2 \cdots C_m \tag{8.8}$$

and

$$C^+ = C_{m+2} \cdots C_{N+1} \tag{8.9}$$

The two regions (above and below the luminescence) can be related if the energy flow is analyzed. The energy flux in the  $m$ th layer is given by the magnitude of the corresponding Poynting vector:

$$|S| = |E \times B|^2 = \frac{|\mathbf{n}_m||E|^2}{c} \tag{8.10}$$

Two cases can arise: the luminescence is radiated either towards the bottom (positive direction) or top (negative direction) surface of the sample. In the former case, the flow of energy is described by the following two equations:

$$|\mathbf{n}_m||E_{m''}^+ - E_{m'}^+|^2 = |\mathbf{n}_m||E_{lum}|^2 \tag{8.11}$$

$$|\mathbf{n}_m||E_{m''}^- - E_{m'}^-|^2 = 0 \tag{8.12}$$

In the latter case, equations (8.11) and (8.12) are replaced by:

$$|\mathbf{n}_m||E_{m''}^- - E_{m'}^-|^2 = |\mathbf{n}_m||E_{lum}|^2 \tag{8.13}$$

$$|\mathbf{n}_m||E_{m''}^+ - E_{m'}^+|^2 = 0 \tag{8.14}$$

In experiments, one usually excites the sample through its top surface and measures the fraction of luminescence energy that leaves the sample through either side. Therefore, the following quantities need to be calculated:

$$R^{+/-} = \frac{|\mathbf{n}_0 \cos \theta_0| |E_0^-|^2}{|\mathbf{n}_m \cos \theta_m| |E_{lum}|^2} \quad (8.15)$$

and

$$T^{+/-} = \frac{|\mathbf{n}_{N+1} \cos \theta_{N+1}| |E_{N+1}^+|^2}{|\mathbf{n}_m \cos \theta_m| |E_{lum}|^2} \quad (8.16)$$

where  $R$  is the luminescence through the top surface ("reflection"),  $T$  is the luminescence transmitted through the bottom surface of the sample and the signs (+ or -) refer to the direction of the initial luminescence inside the  $m$ th layer. Note that since cross-sections of the beams inside and outside the sample at non-normal incidence are different, cosine correction factors (Klingshirn, 1995) were included in equations (8.15) and (8.16).

Solving equations (8.6) - (8.7) with the proper boundary conditions ((8.11)-(8.12) or (8.13) - (8.14)) we get

$$T^+ = \left| \frac{\mathbf{n}_{N+1} \cos \theta_{N+1}}{\mathbf{n}_m \cos \theta_m} \right| \frac{|d_{11}^-|^2}{|d_{11}^+ d_{11}^- - d_{21}^+ d_{12}^-|^2} \quad (8.17)$$

$$R^+ = \left| \frac{\mathbf{n}_0 \cos \theta_0}{\mathbf{n}_m \cos \theta_m} \right| \frac{|d_{21}^+|^2 |d_{11}^- d_{22}^- - d_{12}^- d_{21}^-|^2}{|d_{11}^+ d_{11}^- - d_{21}^+ d_{12}^-|^2} \quad (8.18)$$

$$T^- = \left| \frac{\mathbf{n}_{N+1} \cos \theta_{N+1}}{\mathbf{n}_m \cos \theta_m} \right| \frac{|d_{12}^-|^2}{|d_{11}^+ d_{11}^- - d_{21}^+ d_{12}^-|^2} \quad (8.19)$$

$$R^- = \left| \frac{\mathbf{n}_0 \cos \theta_0}{\mathbf{n}_m \cos \theta_m} \right| \frac{|d_{11}^+|^2 |d_{11}^- d_{22}^- - d_{12}^- d_{21}^-|^2}{|d_{11}^+ d_{11}^- - d_{21}^+ d_{12}^-|^2} \quad (8.20)$$

Expressions (8.17)-(8.20) can be restated using matrices  $C^+$  and  $C^-$ . Unlike  $D^{+/-}$  the  $C^{+/-}$  matrices are independent of  $z_m$  so the following expressions are more appropriate for integration w.r.t.  $z_m$ :

$$T^+ = \frac{|\mathbf{n}_{N+1} \cos \theta_{N+1} / (\mathbf{n}_m \cos \theta_m)| |t_{m+1} c_{11}^-|^2 e^{-\frac{4\pi}{\lambda} z_m \text{Im}(\mathbf{n}_m \cos \theta_m)}}{\left| c_{11}^- (c_{11}^+ + r_{m+1} c_{21}^+) e^{i\frac{2\pi}{\lambda} \mathbf{n}_m d_m \cos \theta_m} - c_{12}^- (c_{21}^+ + r_{m+1} c_{11}^+) e^{-i\frac{2\pi}{\lambda} \mathbf{n}_m d_m \cos \theta_m} \right|^2} \quad (8.21)$$

$$T^- = \frac{|\mathbf{n}_{N+1} \cos \theta_{N+1} / (\mathbf{n}_m \cos \theta_m)| |t_{m+1} c_{12}^-|^2 e^{\frac{4\pi}{\lambda} z_m \text{Im}(\mathbf{n}_m \cos \theta_m)}}{\left| c_{11}^- (c_{11}^+ + r_{m+1} c_{21}^+) e^{i\frac{2\pi}{\lambda} \mathbf{n}_m d_m \cos \theta_m} - c_{12}^- (c_{21}^+ + r_{m+1} c_{11}^+) e^{-i\frac{2\pi}{\lambda} \mathbf{n}_m d_m \cos \theta_m} \right|^2} \quad (8.22)$$

$$R^+ = \frac{|\mathbf{n}_0 \cos \theta_0 / (\mathbf{n}_m \cos \theta_m)| |(c_{11}^- c_{22}^- - c_{12}^- c_{21}^-) (c_{21}^+ + r_{m+1} c_{11}^+)|^2 e^{-\frac{4\pi}{\lambda} z_m \text{Im}(\mathbf{n}_m \cos \theta_m)}}{\left| c_{11}^- (c_{11}^+ + r_{m+1} c_{21}^+) e^{i\frac{2\pi}{\lambda} \mathbf{n}_m d_m \cos \theta_m} - c_{12}^- (c_{21}^+ + r_{m+1} c_{11}^+) e^{-i\frac{2\pi}{\lambda} \mathbf{n}_m d_m \cos \theta_m} \right|^2} \quad (8.23)$$

$$R^- = \frac{|\mathbf{n}_0 \cos \theta_0 / (\mathbf{n}_m \cos \theta_m)| |(c_{11}^- c_{22}^- - c_{12}^- c_{21}^-) (c_{11}^+ + r_{m+1} c_{21}^+)|^2 e^{\frac{4\pi}{\lambda} z_m \text{Im}(\mathbf{n}_m \cos \theta_m)}}{\left| c_{11}^- (c_{11}^+ + r_{m+1} c_{21}^+) e^{i\frac{2\pi}{\lambda} \mathbf{n}_m d_m \cos \theta_m} - c_{12}^- (c_{21}^+ + r_{m+1} c_{11}^+) e^{-i\frac{2\pi}{\lambda} \mathbf{n}_m d_m \cos \theta_m} \right|^2} \quad (8.24)$$

In experiments, luminescence is collected from a finite collection angle (determined by the objective) and from the whole layer. Then, for example, the fraction of radiated luminescence through the top surface of the sample is given by the following integral

$$R_m = \frac{\int_0^{d_m} dz_m \rho(z_m) \int_{\theta_{min}}^{\theta_{max}} d\theta \sin \theta (R^+ + R^-) / 2}{d_m (\cos \theta_{min} - \cos \theta_{max}) \int_0^{d_m} dz_m \rho(z_m)} \quad (8.25)$$

where  $\rho(z_m)$  is the probability of luminescence generation at depth  $z_m$ . It is obtained by solving the carrier diffusion equations for the given material and excitation geometry (Bensaid 1989, Luke and Cheng, 1987, Hooft and van Oopdorp, 1986, Boulou and Bois, 1977). If the diffusion length of carriers is larger

than the depth of focus of the objective,  $\rho(z)$  will have to be modified to account for this. For most objectives (except reflecting objectives)  $\theta_{min} = 0$ . The integral (8.25) assumes isotropic luminescence, therefore an average was taken between  $R^+$  and  $R^-$ . It will be shown later on that the integration over  $\theta$  is not always necessary as the  $\theta$  dependence is rather weak, and formulas for normal incidence can be used for low power objectives. The index of refraction  $\mathbf{n}_m$  in the layer from which luminescence originates can be modified to account for stimulated emission, or other effects.

### 8.3 Discussion and Analysis

By examining equations (8.21)-(8.24) we easily see that if the layer in which the luminescence occurs is transparent, the radiated luminescence lineshape does not depend on the depth at which the luminescence was generated. Equations (8.21)-(8.24) contain only one term that has a dependence on  $z_m$  - the exponential in the numerator. However, for a transparent layer  $\text{Im}(\mathbf{n}_m) = 0$  and this term is constant.

For luminescence that occurs in absorbing materials (such as direct bandgap semiconductors, especially when the Urbach tail is pronounced), there is a strong depth dependence. In time-resolved luminescence experiments, as the carriers diffuse and recombine deeper in the sample, the radiated luminescence is substantially decreased. This can result in a systematic underestimation of the carrier lifetime.

Equations (8.17)-(8.20) are rather cumbersome, and closed analytical expressions in terms of indices of refraction and layer thicknesses cannot be obtained but for the simplest of sample geometries and only at normal incidence. There-

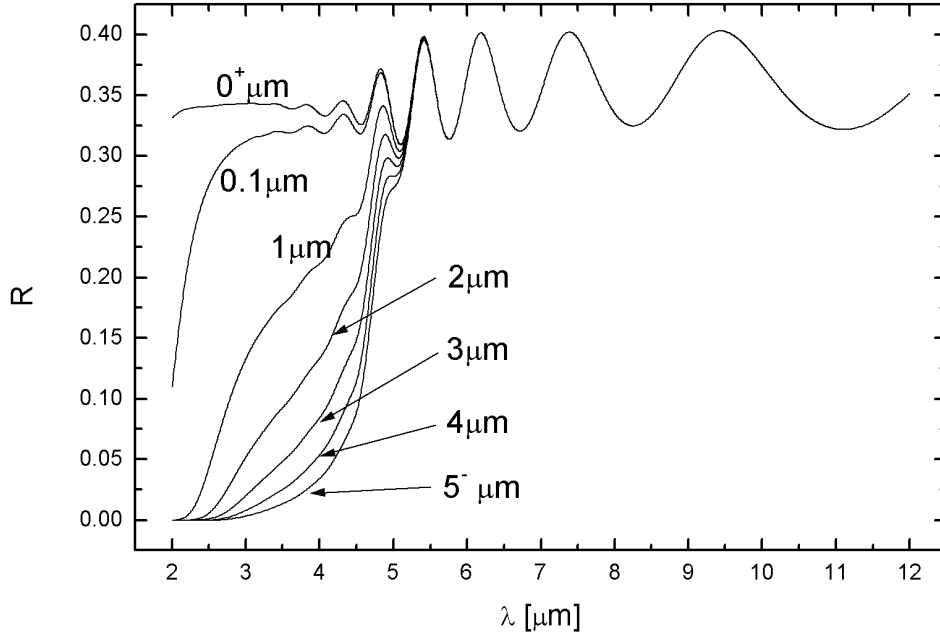


Figure 8.2: Depth dependence.

fore, only a numerical analysis of these equations will be given.

Figure 8.2 shows the fraction of radiated luminescence in a sample as a function of depth where the luminescence originated. The sample is a  $5\mu\text{m}$  thick film of  $\text{Hg}_{0.724}\text{Cd}_{0.276}\text{Te}$  on a bulk CdTe substrate. The bandgap for the epilayer is  $E_g = 0.258\text{eV}$ . The values for  $\mathbf{n}_1$  ( $\text{Hg}_{1-x}\text{Cd}_x\text{Te}$ ) and  $\mathbf{n}_2$  (CdTe) were taken from (Kucera, 1987, Chu et al., 1991) and (Marple, 1964) respectively. It can be seen that in parts of the spectrum where the film is absorbing, the luminescence has a strong depth dependence. It important to note that these curves are quite sensitive to the value of optical constants and thicknesses of the layers. For accurate correction, it is recommended that actual values for the index of refraction and absorption and layer thicknesses be used instead of literature values and nominal thicknesses.

Figure 8.3 shows the effect of the collection angle. For low power objectives (e.g.  $\text{NA}=0.125$  or  $\theta \approx 7^\circ$ ) there is only a slight difference when compared with

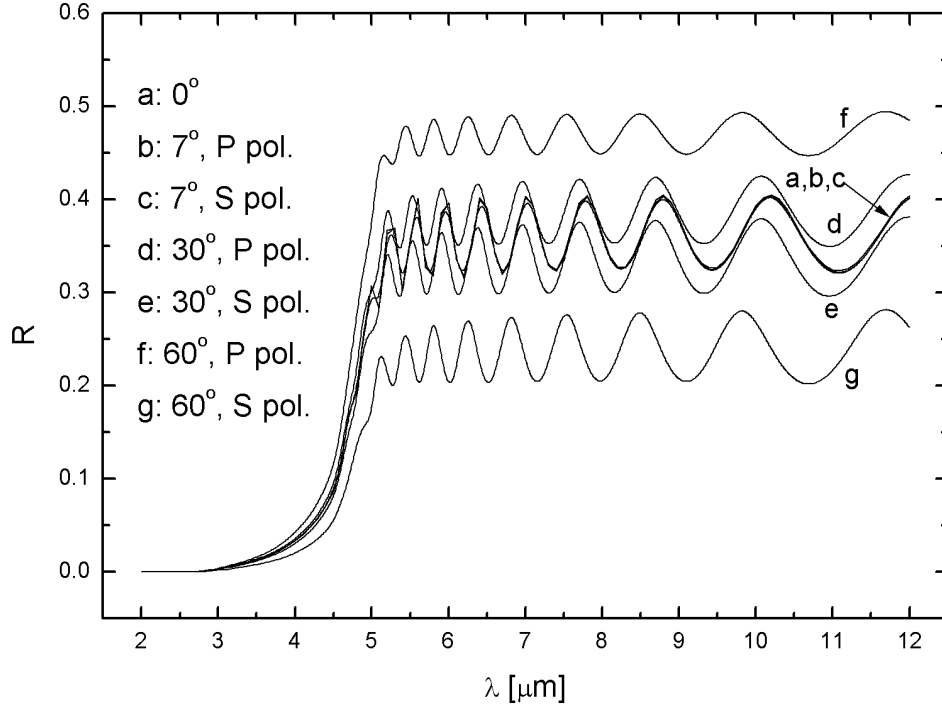


Figure 8.3: Collection angle dependence.

the formulas for normal incidence (especially if the  $p$  and  $s$  polarizations are averaged). For high-NA objectives, a substantial deviation is observed.

To demonstrate the importance of these corrections, a measured 5K photoluminescence spectrum of a  $2.34\mu\text{m}$  thick CdTe film deposited on a glass substrate will be analyzed (Bitar et al., 1995). The spectrum contains three pronounced peaks, as shown in Fig. 8.4. We believe that the defect levels identified in (Bitar et al., 1995) are greatly influenced (their position) or even caused by the interference effects in the film. To demonstrate this, the measured spectrum was divided by the luminescence efficiency curves given by equations (8.23) and (8.24) assuming a reported film thickness of  $2.34\mu\text{m}$  and  $n = 1.571$  for the glass substrate. The index of refraction of the CdTe film was not known, so a simple quadratic dispersion in the transparent region near the bandgap was assumed. A value that gave reasonably good agreement was  $n(E) = 2.65 + 3.78(E - 1.3)^2$ .

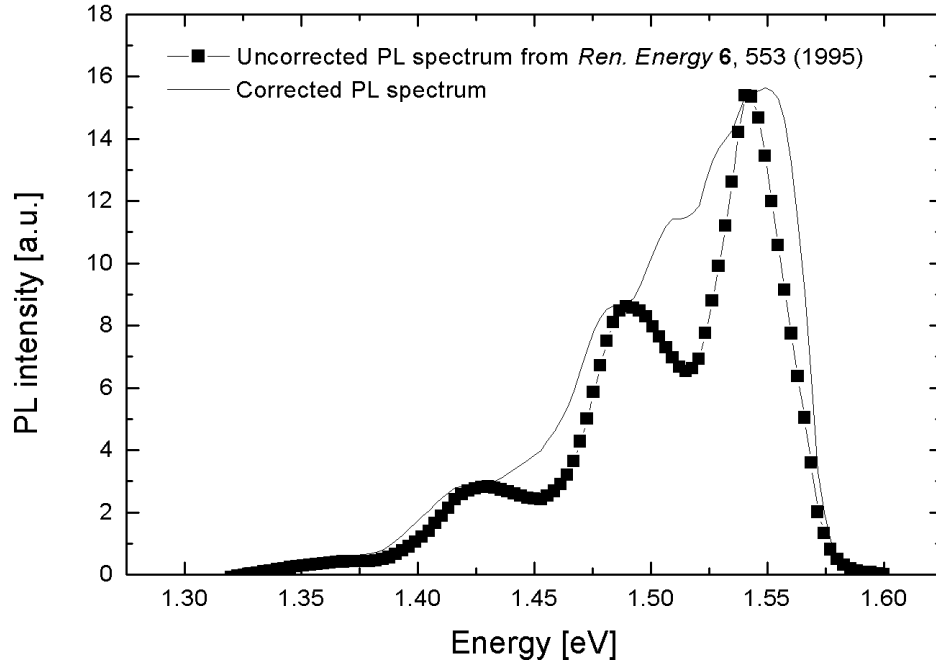


Figure 8.4: Uncorrected and corrected PL spectrum of CdTe/glass.

With these values the three peaks in the spectrum are greatly reduced and a smooth single broad peak is revealed.

# Chapter 9

## Summary

In this chapter we briefly summarize what was accomplished in this work and present the major conclusions.

- We have developed a novel experimental apparatus, based on Fourier Transform Infrared (FTIR) Spectrometry, suitable for the measurement of photoluminescence, transmittance and photo-transmittance with high spectral and diffraction limited spatial resolution in the infrared portion of the spectrum. The apparatus was used for the investigation of defects in MBE grown  $\text{Hg}_{1-x}\text{Cd}_x\text{Te}$  and bulk CdTe and  $\text{Cd}_{0.96}\text{Zn}_{0.04}\text{Te}$  by measuring photoluminescence.
- We have developed a novel algorithm for error-free phase correction of FTIR interferograms based on the application of digital all-pass filter. This new method is particularly useful for high precision measurements (such as in infrared spectroscopic ellipsometry), or in the processing of large amounts of spectra such as in FTIR imaging.
- It was shown that photoluminescence imaging can be a viable character-

ization tool used in the process of fabrication of infrared materials and devices. It can be useful in the optimization of the MBE growth process.

- We have analyzed photoluminescence spectra of bulk CdTe and Cd<sub>0.96</sub>Zn<sub>0.04</sub>Te used in MBE growth of Hg<sub>1-x</sub>Cd<sub>x</sub>Te epilayers. Defect levels were analyzed and identified. For example, for CdTe have shown the the broad defect peak in the 1.3-1.5eV region consist of at least three distinct defect level transitions. We measured the temperature dependence of PL spectra. We also analyzed the spatial distribution of defect level transitions.
- For Hg<sub>1-x</sub>Cd<sub>x</sub>Te epilayers, we studied the influence of substrate preparation on band-edge photoluminescence. The temperature dependence of the photoluminescence spectra was measured and analyzed. We also identified a defect level transition in doped Hg<sub>1-x</sub>Cd<sub>x</sub>Te samples.
- We calculated correction factors to account for the distortion of photoluminescence spectra from multilayered structures to distinguish between spectral artifacts and actual defect level transitions.
- We have shown, for the first time, that photo-transmittance can be successfully measured using Fourier Transform Infrared Spectrometry. We have also formulated a special phase correction procedure needed to process interferograms from photo-transmittance (or photo-reflectance) experiments.
- We have measured photo-transmittance in Hg<sub>1-x</sub>Cd<sub>x</sub>Te around the band edge. This could be used to determine the bandgap with higher precision than current methods based on analyzing the shape of the absorption coefficient curve.

# References

- Alt, H. C., Neef, M. and von Philipsborn, H., Appl. Phys. Lett. **55**, 1972 (1989).
- Arakawa, T., Watabe, H., Nagamune, Y. and Arakawa, Y., Appl. Phys. Lett. **69**, 1294 (1996).
- Ardila, A. M., Martinez, O., Avella, M., Jimenez, J., Gil-Lafon, E. and Gerard, B., J. Mater. Res. **17**, 1341 (2002).
- Ariel, V., Garber, V., Bahir, G., Raizman, A. and Sher, A., Appl. Phys. Lett. **70**, 1849 (1997).
- Aspnes, D. E., *Handbook on Semiconductors Volume 2: Optical Properties of Solids* (M. Balkanski, ed.) (North-Holland Publishing Co., Amsterdam, 1980).
- Bajaj, J., Arias, J. M. and Zandian, M., J. Electron. Mater. **25**, 1394 (1996).
- Bassignana, I. C., Miner, C. J. and Puetz, N., J. Appl. Phys. **65**, 4229 (1989).
- Bensaid, B., J. Appl. Phys. **66**, 5542 (1989).
- Bishop, S. G., Jr., J. A. F., Jr., P. E. R. N. and Gipe, M. L., Amorphous and Crystalline Silicon Carbide II. Recent Developments. Proc. of the 2nd Intern. Conf. p. 112 (1989).
- Bitar, R. A., Moutinho, H., Abulfotuh, F. and Kazmerski, L., Renewable Energy **6**, 553 (1995).
- Boulou, M. and Bois, D., J. Appl. Phys. **48**, 4713 (1977).
- Bryant, F. J., Totterdell, D. H. J. and Hagston, W. E., J. Phys. C **4**, 641 (1971).
- Capper, P. (Ed.), *Narrow-gap II-VI Compounds for Optoelectronic and Electromagnetic Applications* (Chapman & Hall, London, 1997), p. 145.
- Chadi, D. J., Walter, J. P. and Cohen, M. L., Phys. Rev. **5**, 3058 (1972).

- Chang, Y., Badano, G., Zhao, J., Zhou, Y. D., Ashokan, R., Grein, C. H. and Nathan, V., *J. Electron. Mater.* **33**, 709 (2004).
- Chang, Y., Chu, J. H., Ji, R. B., Wang, X. G., Huang, G. S., Li, J. F., He, L. and Tang, D. Y., *Fourth Intern. Conf. on Thin Films, Proc. SPIE* **4086**, 182 (2000).
- Chase, D. B., *Appl. Spectrosc.* **36**, 240 (1982).
- Chu, J., Mi, Z. and Tang, D., *Infrared Phys.* **32**, 195 (1991).
- Daraselia, M., Carmody, M., Edwall, D. D. and Tiwald, T. E., *J. Electron. Mater.* **34**, 762 (2005).
- Deczky, A. G., *IEEE Trans. Acoustics Speech, Signal Processing* **22**, 98 (1974).
- Finkman, E. and Schacham, S. E., *J. Appl. Phys.* **56**, 2896 (1984).
- Forman, M. L., Steele, W. H. and Vanasse, G. A., *J. Opt. Soc. Am.* **56**, 59 (1966).
- Francou, J. M., Saminadaray, K., Molva, E. and Pautrat, J. L., *Proc. 13th Intern. Conf. on Defects in Semiconductors* (Metallurgical Society of AIME, New York, 1985).
- Fuchs, F., Lusson, A., Koidl, P. and Triboulet, R., *J. Cryst. Growth* **101**, 722 (1990).
- Furstenberg, R. and White, J. O., *Appl. Spectrosc.* **59**, 316 (2005).
- Furstenberg, R. and White, J. O., *Vib. Spectrosc.*, (accepted) (2006).
- Furstenberg, R., White, J. O., Dinan, J. H. and Olson, G. L., *J. Electron. Mater.* **33**, 714 (2004).
- Furstenberg, R., White, J. O. and Olson, G. L., *J. Electron. Mater.* **34**, 791 (2005).
- Garbuzov, D. Z., *Semiconductor Physics, (edited by V. M. Tuchkevich and V. Y. Frenkel)* (Consultants Bureau, New York, 1986).
- Giles-Taylor, N. C., Bicknell, R. N., Blanks, D. K., Myers, T. H. and Schetzina, J. F., *J. Vac. Sci. Technol. A* **3**, 76 (1985).
- Greeff, C. W. and Glyde, H. R., *Phys. Rev. B* **51**, 1778 (1995).

- Griffiths, P. R. and de Haseth, J. A., *Fourier Transform Infrared Spectrometry* (John Wiley & Sons, New York, 1986).
- Hansen, G. L., Schmit, J. L. and Casselman, T. N., *J. Appl. Phys.* **53**, 7099 (1982).
- Haugen, G. M., Guha, S., DePuydt, J. M., Haase, M. A., Law, K. K., Miller, T. J. and Wu, B. J., *Proc. SPIE* **2346**, 16 (1999).
- Heavens, O. S., *Optical Properties of Thin Solid Films* (Dover, 1991).
- Hofmann, D. M., Omling, P., Grimmeiss, H. G., Meyer, B. K., Benz, K. and Sinerius, D., *Phys. Rev. B* **45**, 6247 (1992).
- Hooft, G. W. and van Opdorp, C., *J. Appl. Phys.* **60**, 1065 (1986).
- Jing, Z., *IEEE Trans. Acoustics Speech, Signal Processing* **35**, 1557 (1987).
- Johnson, J. R., *Introduction to Digital Signal Processing* (Prentice Hall, New York, 1989).
- Johnson, J. R., *Introduction to Digital Signal Processing* (Prentice Hall, New York, 1989), pp. 96-105.
- Johnson, J. R., *Introduction to Digital Signal Processing* (Prentice Hall, New York, 1989), p. 244.
- Johnson, J. R., *Introduction to Digital Signal Processing* (Prentice Hall, New York, 1989), p. 120.
- Kazmierski, K., Hirtz, P., Ricciardi, J., Razeghi, M. and Cremoux, B. D., *Defect Recognition and Image Processing in III-V Compounds. Proc. of the Intern. Symp.* p. 279 (1985).
- Klingshirn, C. F., *Semiconductor Optics* (Springer, 1995).
- Kobayashi, A., Sankey, O. F. and Dow, J. D., *Phys. Rev. B* **25**, 6367 (1982).
- Kraus, M. M., Becker, C. R., Scholl, S., Wu, Y. S. and Landwehr, G., *Semicond. Sci. Technol.* **8**, 962 (1993).
- Krishnamurty, S., Chen, A. B. and Sher, A., *J. Appl. Phys.* **80**, 4045 (1996).
- Krustok, J., Valdna, V., Hjelt, K. and Collan, H., *J. Appl. Phys.* **80**, 1757 (1996).
- Kucera, Z., *phys. stat. sol. (a)* **100**, 659 (1987).

- Kurtz, S. R., Bajaj, J., Edwall, D. D. and Irvine, S. J. C., *Semicond. Sci. Technol.* **8**, 941 (1993).
- Lee, J., Giles, N. C., Rajavel, D. and summers, C. J., *Phys. Rev. B* **49**, 1668 (1994).
- Lester, S. D., Kim, T. S. and Streetman, B. G., *J. Appl. Phys.* **63**, 853 (1988).
- Li, B., Chu, J. H., Chang, Y., Gui, Y. S. and Tang, D. Y., *Infrared Phys. Technol.* **37**, 525 (1996).
- Luke, K. L. and Cheng, L. J., *J. Appl. Phys.* **61**, 2282 (1987).
- Marple, D., *J. Appl. Phys.* **35**, 539 (1964).
- Mertz, L., *Transformations in Optics* (John Wiley and Sons, New York, 1965).
- Moazzami, K., Liao, D., Phillips, J. D., Lee, D. L., Carmody, M., Zandian, M. and Edwall, D. D., *J. Electron. Mater.* **32**, 646 (2003).
- Molva, E., Bunod, P., Chabli, A., Lombardot, A., Dubois, S. and Bertin, F., *J. of Crystal Growth* **103**, 91 (1990).
- Molva, E., Pautrat, J. L., Saminadaray, K., Milchberg, G. and Magnea, N., *Phys. Rev. B* **30**, 3344 (1984).
- Nafie, L. A. and Diem, M., *Appl. Spectrosc.* **33**, 130 (1979).
- Nathan, V., *J. Appl. Phys.* **83**, 2812 (1998).
- Pernot, E., Harrouniand, I. E., Mermouxand, M., Bluetand, J. M., Anikin, M., Chaussende, D., Pons, M. and Madar, R., *Materials Science Forum* **433-436**, 265 (2003).
- Petruzzello, J., Herko, S. P., Gaines, J. M. and Marshall, T., *Phys. Stat. Sol. B* **187**, 297 (1995).
- Schmidt, H., Tomm, J. W. and Hermann, K. H., *J. Cryst. Growth* **101**, 474 (1990).
- Schubert, E. F., Goebel, E. O., Horikoshi, Y., Ploog, K. and Queisser, H. J., *Phys. Rev. B* **30**, 813 (1984).
- Shahzad, K. and Cammack, D. A., *Appl. Phys. Lett.* **56**, 180 (1990).
- Singh, R., Velicu, S., Crocco, J., Chang, Y., Zhao, J., Almeida, L. A., Markunas, J., Kaleczyc, A. and Dinan, J. H., *J. Electron. Mater.* **34**, 885 (2005).

Sochinskii, N. V., Babentsov, V. N., McNally, P. J., Dundee, A. and Corsi, C., *Infrared Phys. & Technology* **46**, 181 (2004).

Stavola, M., *Semiconductors and Semimetals Volume 51B: Identification of Defects in Semiconductors* (Academic Press, San Diego, 1999).

Urbach, F., *Phys. Rev.* **92**, 1324 (1953).

Vetter, T. and Winnacker, A., *J. Mater. Res.* **6**, 1055 (1991).

Vina, L., Umbach, C., Cardona, M. and Vodopyanov, L., *Phys. Rev. B* **29**, 6752 (1984).

Warwick, C. A., *J. Appl. Phys.* **59**, 4182 (1986).

Wolny, M., Duluc, T. and Linne, C., *Proc. SPIE* **2228**, 332 (1994).

Yang, M. J., Yamaguchi, M., Takamoto, T., Ikeda, E., Kurita, H. and Ohmori, M., *Solar Energy Materials and Solar Cells* **45**, 331 (1997).

# Author's Biography

Robert Furstenberg was born on January 15, 1974, in Subotica, Serbia and Montenegro. He received a B.S. degree in Physics from the University of Novi Sad (Novi Sad, Serbia and Montenegro) in 1998 and an M.S. degree in Physics from the University of Illinois at Urbana-Champaign in 1999. He received a Postdoctoral Fellowship from the National Research Council and plans to study the opto-magnetic properties of magnetic nanostructures at the Naval Research Laboratory.